

AD-A282 971



A Final Report AEOSSR-TR- 94 0472
Grant No. F49620-93-1-0245

April 1, 1993 - March 31, 1994

**FUNDAMENTAL CONCEPTS RELATING LOCAL ATOMIC
ARRANGEMENTS, DEFORMATION AND FRACTURE
OF INTERMETALLIC ALLOYS**

Submitted to:

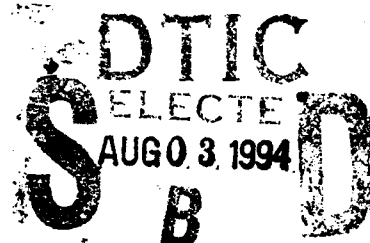
Air Force Office of Scientific Research
110 Duncan Avenue, Suite B115
Bolling Air Force Base
Washington, DC 20332-0001

Attention:

Dr. Charles Ward, NC
Directorate of Chemistry and Materials Science

Submitted by:

John A. Wert
Professor



SEAS Report No. UVA/525771/MSE94/101
April 1994

DEPARTMENT OF MATERIALS SCIENCE AND ENGINEERING

SCHOOL OF
ENGINEERING 
& APPLIED SCIENCE

University of Virginia
Thornton Hall
Charlottesville, VA 22903

Approved for public release;
distribution unlimited.

DTIC REPORT AVAILABLE

94 8 02 202

94-24557

UNIVERSITY OF VIRGINIA
School of Engineering and Applied Science

The University of Virginia's School of Engineering and Applied Science has an undergraduate enrollment of approximately 1,500 students with a graduate enrollment of approximately 600. There are 160 faculty members, a majority of whom conduct research in addition to teaching.

Research is a vital part of the educational program and interests parallel academic specialties. These range from the classical engineering disciplines of Chemical, Civil, Electrical, and Mechanical and Aerospace to newer, more specialized fields of Applied Mechanics, Biomedical Engineering, Systems Engineering, Materials Science, Nuclear Engineering and Engineering Physics, Applied Mathematics and Computer Science. Within these disciplines there are well equipped laboratories for conducting highly specialized research. All departments offer the doctorate; Biomedical and Materials Science grant only graduate degrees. In addition, courses in the humanities are offered within the School.

The University of Virginia (which includes approximately 2,000 faculty and a total of full-time student enrollment of about 17,000), also offers professional degrees under the schools of Architecture, Law, Medicine, Nursing, Commerce, Business Administration, and Education. In addition, the College of Arts and Sciences houses departments of Mathematics, Physics, Chemistry and others relevant to the engineering research program. The School of Engineering and Applied Science is an integral part of this University community which provides opportunities for interdisciplinary work in pursuit of the basic goals of education, research, and public service.

REPORT DOCUMENTATION PAGE

Form Approved
OMB No. 0704-0188

Public reporting burden for this collection of information is estimated to average 1 hour per response, including the time for reviewing instructions, searching existing data sources, gathering and maintaining the data needed, and completing and reviewing the collection of information. Send comments regarding this burden estimate or any other aspect of this collection of information, including suggestions for reducing this burden, to Washington Headquarters Services, Directorate for Information Operations and Reports, 1215 Jefferson Davis Highway, Suite 1204, Arlington, VA 22202-4302, and to the Office of Management and Budget, Paperwork Reduction Project (0704-0188), Washington, DC 20503.

1. AGENCY USE ONLY (Leave blank)		2. REPORT DATE April 1994	3. REPORT TYPE AND DATES COVERED Final Report - 4/1/93 - 3/31/94
4. TITLE AND SUBTITLE Fundamental Concepts Relating Local Atomic Arrangements, Deformation and Fracture of Intermetallic Alloys		5. FUNDING NUMBERS Grant No. F49620-93-1-0245	
6. AUTHORS(S) John A. Wert, Professor			
7. PERFORMING ORGANIZATION NAMES(S) AND ADDRESS(ES) University of Virginia Department of Materials Science and Engineering School of Engineering and Applied Science Thornton Hall Charlottesville, VA 22903-2442		8. PERFORMING ORGANIZATION REPORT NUMBER UVA/525771/MSE94/101 AFOSR-JR- 94 0472	
9. SPONSORING/MONITORING AGENCY NAMES(S) AND ADDRESS(ES) Air Force Office of Scientific Research 110 Duncan Avenue, Suite B115 Bolling Air Force Base Washington, DC 20332-0001		10. SPONSORING/MONITORING AGENCY REPORT NUMBER	
11. SUPPLEMENTARY NOTES			
12a. DISTRIBUTION/AVAILABILITY STATEMENT Approved for public release; distribution unlimited.		12b. DISTRIBUTION CODE	
13. ABSTRACT (Maximum 200 words) The creep resistance of a TiAl/Ti ₃ Al alloy with a lamellar microstructure has been previously found to be superior to the creep resistance of single-phase TiAl and Ti ₃ Al alloys with compositions close to the compositions of the individual phases in the lamellar alloy. The objectives of the present research project were to identify the origin of the enhanced creep resistance of the TiAl/Ti ₃ Al lamellar alloy, to formulate a model capable of predicting the creep strength of the TiAl/Ti ₃ Al lamellar alloy, and to evaluate the effect of thermal exposure on the creep strength of the TiAl/Ti ₃ Al lamellar alloy. The results, analyses and interpretations described in this report show that the enhanced creep resistance of the TiAl/Ti ₃ Al lamellar alloy arises from the lamellar morphology of the TiAl and Ti ₃ Al phases. The lamellar morphology provides a large interphase interfacial area per unit volume, which is proposed to introduce a high density of dislocation sources. The high density of dislocation sources is thought to increase the work hardening rate of the lamellar alloy relative to the individual single phase alloys; an effect which contributes the small primary creep strain and low secondary creep rate exhibited by the lamellar alloy. When the increased work hardening rate is accounted for in the constitutive equations for creep of the individual TiAl and Ti ₃ Al phases, an analytical model formulated for creep of discontinuous, lamellar-reinforced composites can be used to predict the creep strength of the TiAl/Ti ₃ Al lamellar alloy from the creep properties of the single phase alloys. Finally, thermal exposure causes coarsening of the lamellar microstructure and degradation of the creep resistance, but the process is very slow at the projected service temperature.			
14. SUBJECT TERMS TiAl, Ti ₃ Al, Intermetallic, Creep, Lamellar Composite, Constitutive Model, Coarsening		15. NUMBER OF PAGES 115	
		16. PRICE CODE	
17. SECURITY CLASSIFICATION OF REPORT Unclassified	18. SECURITY CLASSIFICATION OF THIS PAGE Unclassified	19. SECURITY CLASSIFICATION OF ABSTRACT Unlimited	20. LIMITATION OF ABSTRACT Unlimited

TABLE OF CONTENTS

Chapter I	Introduction	2
Chapter II	Measurement of the Compressive Creep Strain Rates of the Individual Phases within a Lamellar Microstructure	6
Chapter III	Modeling Creep Deformation of a Two-Phase TiAl/Ti ₃ Al Alloy with a Lamellar Microstructure	26
Chapter IV	Modeling the Minimum Creep Rate of Discontinuous Lamellar-Reinforced Composites	58
Chapter V	The Effect of Thermal Exposure on Microstructural Stability and Creep Resistance of a Two-Phase TiAl/Ti ₃ Al Lamellar Alloy	83
Chapter VI	Publications and Presentations	115

Accession For	
NTIS GRA&I	<input checked="" type="checkbox"/>
DTIC TAB	<input type="checkbox"/>
Unannounced	<input type="checkbox"/>
Justification	
By	
Distribution/	
Availability Codes	
Dist	Avail and/or Special
A-1	

Chapter I

INTRODUCTION

This is the final technical report for a 1 year research project to explore the creep resistance of a TiAl/Ti₃Al alloy with a lamellar microstructure. The current research was undertaken when an earlier study revealed that the creep resistance of the TiAl/Ti₃Al lamellar alloy was superior to the creep resistance of single-phase TiAl and Ti₃Al alloys with compositions close to the compositions of the phases in the lamellar alloy. This unexpected result indicates that the elevated temperature mechanical properties of the lamellar alloy are not related to the properties of its constituent phases solely by composite strengthening mechanisms. The objectives of the present research project were to identify the origin of the enhanced creep resistance of the TiAl/Ti₃Al lamellar alloy, to formulate a model capable of predicting the creep strength of the TiAl/Ti₃Al lamellar alloy, and to evaluate the effect of thermal exposure on the creep strength of the TiAl/Ti₃Al lamellar alloy.

The experimental results, models and analyses used to accomplish the objectives stated above have been incorporated into a series of research papers that describe various aspects of the work. This report consists of the 4 papers that have been prepared based on work during the past year. To clarify the unifying thread that connects the papers, the topics and key conclusions from each paper are presented below.

1. Measurement of the Compressive Creep Strain Rates of the Individual Phases within a Lamellar Microstructure. (Chapter II)

In this paper, a technique is described for measuring the strain rate in the individual phases during creep of a duplex alloy with a lamellar microstructure. The technique involves scribing fiducial lines on the surface of the specimen prior to the creep test, and carefully measuring the orientation of the lines before and after the test. The change of orientation of a fiducial line in each phase depends on the strain rate of phase and the lamellar orientation. Using an analysis described in the paper, the strain rate can be determined by coupling fiducial line measurements with stereological measurements. The analysis can be applied to creep of any alloy with a lamellar microstructure subject to creep under a uniaxial applied stress.

Although the analysis technique is general, the paper describes its application to creep of the TiAl/Ti₃Al lamellar alloy. The results reveal that the creep rates of the TiAl and Ti₃Al phases in the lamellar microstructure are about 20 times lower than the creep rates of single phase TiAl and Ti₃Al alloys, and that no interfacial sliding occurs during creep. This result demonstrates that the lower creep rate of the TiAl/Ti₃Al lamellar alloy is a consequence of decreased creep rates of the TiAl and Ti₃Al phases when they assume the lamellar morphology. This effect is termed *enhanced hardening* of the phases in the lamellar microstructure.

2. Modeling Creep Deformation of a Two-Phase TiAl/Ti₃Al Alloy with a Lamellar Microstructure. (Chapter III)

In this paper, the constitutive relationships for creep of single phase TiAl and Ti₃Al alloys are modified to include the enhanced hardening factors determined from the fiducial line experiments. Once these factors are introduced, the single-phase constitutive equations are incorporated into a composite strengthening model similar to the classic Kelly and Street model. The model is formulated to predict the creep rate of a composite containing randomly aligned plates of a reinforcing phase in the situation where both the matrix and reinforcing phases exhibit power law creep. For modeling purposes, it is immaterial whether the reinforcing plates are grouped into randomly oriented lamellar colonies (as in the TiAl/Ti₃Al lamellar alloy) or are dispersed as individual randomly oriented plates.

The model requires as inputs the constitutive relationships for the single phase alloys (including the enhanced hardening factors), and the volume fraction and dimensions of the reinforcing plates. The creep rate of the lamellar alloy predicted by the model matches the experimentally observed creep rate for the lamellar alloy over the full ranges of stress and temperature explored in the study.

3. Modeling the Minimum Creep Rate of Discontinuous Lamellar-Reinforced Composites. (Chapter IV)

The modeling work described above was focused on the TiAl/Ti₃Al lamellar alloy in which the creep rates of the matrix and reinforcing phases are not very different. To place this work in the broader context of constitutive relationships for creep of composite materials, the model for creep of a composite material with randomly

oriented plates of the reinforcing phase was extended to consider a wide range of relative strengths of the matrix and reinforcing phases. While the model is analytical rather than numerical, the analytical expression for the creep rate of the composite is complex and results are most conveniently represented in graphical form.

Two important results from the more generalized model are pertinent to the TiAl/Ti₃Al lamellar alloy. One result shows that the creep rate of the lamellar composite is not strongly affected by the plate aspect ratio (length/thickness) when the two phases have similar creep rates. Thus, changes in plate aspect ratio during creep are not predicted to strongly degrade the creep strength of the TiAl/Ti₃Al lamellar alloy. A second key result shows that lamellar reinforcements and fiber reinforcements provide approximately the same degree of composite strengthening, unless the reinforcing phases is essentially nondeforming. Thus, attempts to convert the lamellar morphology of the TiAl/Ti₃Al alloy to a fiber-like morphology are not predicted to produce a significant benefit.

4. The Effect of Thermal Exposure on Microstructural Stability and Creep Resistance of a Two-Phase TiAl/Ti₃Al Lamellar Alloy. (Chapter V)

The long-term thermal stability of microstructures is an important aspect of creep-resistant materials. Much prior experimental and modeling work has explored the evolution of lamellar microstructures by diffusional processes. The fourth paper addresses the thermal stability of the lamellar microstructure found in the TiAl/Ti₃Al alloy, and the effect of evolution of this microstructure on creep resistance.

The first part of the paper presents and interprets experimental results that describe the kinetics of coarsening and eventual globularization of the lamellar microstructure. Coarsening of the lamellar microstructure initially proceeds mainly by termination migration, and the coarsening experiments yield an activation energy for this process.

The second part of the paper shows that the creep rate at constant stress and temperature increases as a result of prior thermal exposure. The increased creep rate after microstructural coarsening is consistent with an analysis that includes two factors. The first factor is the reduced interphase interfacial area per unit volume in the coarsened microstructure. It is postulated that the enhanced hardening factor arises

from dislocation generation at interphase interfaces. This suggests that when the coarsening process decreases the interphase interface area, the enhanced hardening factors decrease and the creep rate of the lamellar composite increases. The second factor affecting creep rates is the reduced composite strengthening effect associated with conversion of the initial lamellar microstructure into an equiaxed two phase structure for long annealing times.

The activation energy can be used to predict the coarsening rate in the projected service temperature range. This analysis can be combined with the creep results to predict that thermal exposure times in excess of 10,000 hours would be required to measurably increase the creep rate at 1100K (827°C).

The results, analyses and interpretations summarized above show that the objectives of the research project have been met. The enhanced creep resistance of the TiAl/Ti₃Al lamellar alloy arises from the lamellar morphology of the TiAl and Ti₃Al phases, and the creep resistance is found to degrade when the lamellar microstructure is transformed into an equiaxed microstructure. When the enhanced hardening factors are accounted for, an analytical model can be used to predict the creep strength of the TiAl/Ti₃Al lamellar alloy from the creep properties of the single phase alloys. Finally, thermal exposure causes coarsening of the lamellar microstructure and degradation of the creep resistance, but the process is very slow at the projected service temperature.

The remainder of the report consists of the papers that describe the results and analyses summarized above. The papers are arranged as chapters, each with its own set of figures, tables and references.

Chapter II

Measurement of the Compressive Creep Strain Rates of the Individual Phases within a Lamellar Microstructure

1. Introduction

Bartholomeusz, Yang and Wert [1] have reported that the compressive creep rates of a two-phase TiAl/Ti₃Al lamellar alloy are more than an order of magnitude lower than the creep rates of the constituent single-phase alloys tested in compression at the same temperatures and applied stresses. Composite strength models predict that the creep rate of a two-phase composite material is a weighted average of the creep rates of the constituent single phases [2]. The experimental results for the TiAl/Ti₃Al lamellar alloy indicate that the TiAl and Ti₃Al phases within the lamellar microstructure creep at lower rates than the constituent single-phase alloys. This phenomenon has been previously observed in several natural (in-situ) composite materials [3].

Several studies have revealed that combining constituent phases within a composite microstructure can result in effects such as the stabilization of a smaller subgrain size within each constituent phase [4], changes in the active modes of slip and twinning deformation resulting from preferential impurity segregation from one constituent phase to the other [5], and changes in the mobile dislocation density due to the presence of dislocation sources and sinks at interphase interfaces [5-7]. These phenomena change the fundamental thermomechanical response of the constituent phases in a composite microstructure, compared to the response of the individual single-phase materials. To model the thermomechanical properties of the composite, the properties of the constituent phases having the composite morphology are needed. However, it is difficult to use traditional microscopy methods to quantify the contribution of each constituent phase within the lamellar microstructure to the total creep deformation of the composite. In developing models to predict the creep properties of composites where both constituent phases deform plastically during thermomechanical exposure, it is necessary to determine explicitly the contribution of each constituent phase to the overall strain rate of the composite.

A technique has been developed to determine the creep properties of the constituent phases within the microstructure of a lamellar composite undergoing power-law creep. The technique involves inscribing fine fiducial lines on the polished face of a specimen of a lamellar alloy prior to creep deformation. By measuring the orientation of the fiducial line in each constituent phase before and after creep deformation and analyzing the results using a geometrical model, the total strain of each constituent phase within the lamellar microstructure can be calculated. Knowledge of the duration of the creep test yields the strain rates of the constituent phases within the lamellar microstructure at the temperature and macroscopic applied stress used for the creep test. The objective of the present paper is to outline the fiducial line technique. The fiducial line analysis has been applied to a two-phase TiAl/Ti₃Al lamellar alloy to determine the strain in each phase during a compression creep test. Using these results the total strain of the lamellar specimen is calculated and compared to the strain directly measured on the specimen to assess the accuracy of the fiducial line analysis.

2. Experimental Methods

Details concerning preparation of the two-phase TiAl/Ti₃Al lamellar alloy (also referred to as *the lamellar alloy*) used in this study have been previously reported [1]. One face of a compression creep specimen measuring 1.5 x 1.5 mm² x 2 mm was polished using 0.05 μ m alumina powder. By carefully touching the polished face of the specimen to a spinning polishing wheel containing 1 μ m alumina powder, an array of fiducial lines was scratched onto the surface. The scratched face was then lightly etched to enable secondary electron imaging of the polished surface in the scanning electron microscope (SEM). Careful measurements were taken with respect to the initial orientations and positions of several of the fiducial lines. The sample was then crept in compression at 1080 K in a vacuum hot press under an applied stress of 380 MPa for 10.3 h. The macroscopic true plastic strain of the sample at the end of this test was measured to be 0.079. The test was conducted in a vacuum hot press to prevent oxidation from obscuring the fiducial lines. After testing, the new orientations and positions of the fiducial lines were recorded using a SEM.

3. Experimental Results

Fig. 1a is a SEM micrograph of a portion of the polished specimen face of the two-phase TiAl/Ti₃Al lamellar alloy containing a fiducial line (indicated by the arrows)

prior to creep testing. The microstructure consists of lamellar packets containing aligned TiAl and Ti₃Al lamellae. The darker lamellae are TiAl phase which constitutes 64 volume percent of the microstructure. The mean linear intercept lamellar packet diameter is 70 μm and the true thickness of the TiAl lamellae is 3.3 μm . The quantitative metallographic techniques used to obtain these values are described in reference [8]. The fiducial line in Fig. 1a forms an angle of 58.5° with the compression axis and is straight on the scale of the creep specimen. Fig. 1b depicts the same fiducial line passing through the lamellar packet marked "a" in Fig. 1a, after creep testing to a true plastic strain of 0.079. The compression axis and the orientation of the fiducial line prior to testing are marked on Fig. 1b. In the bottom left corner of Fig. 1b, the two lines almost coincide. However, in the top right corner of Fig. 1b, there is a significant difference in the positions of the two lines, and the orientation of the fiducial lines is noticeably different in the two phases.

Although the creep test was conducted in a vacuum hot press, the vacuum during the test was not better than 5 Pa. Furnace debris and some limited oxidation marred the surface of the sample and permitted evaluation of only those lamellar packets for which the position of the fiducial line could be positively discerned. In all, 28 lamellae in three lamellar packets were evaluated. The same fiducial line depicted in Fig. 1 passed through all three lamellar packets. The change in orientation of the fiducial line after the creep test ($\Delta\theta$) was determined for all the lamellae in the three lamellar packets evaluated. The second and third columns in Table 1 depict the average change in orientation of the fiducial line with respect to the compression axis in the TiAl and Ti₃Al lamellae within the three lamellar packets. The standard deviations of the average values were determined on the basis of several independent measurements.

The angles ψ and ϕ in the forth and fifth columns in Table 1 represent the orientation of the lamellae within each packet at the start of the compression test. Within each lamellar packet, all the lamellae are assumed to possess the same orientation. The angles ψ and ϕ are defined in Fig. 2. The orientation of the lamellar faces with respect to the compression axis (x_3 direction) on the polished face is given by ψ . The angle ϕ defines the rotation of the lamellae away from the polished face of the specimen (x_1, x_3 plane). The value of ψ can be directly measured from micrographs of the lamellar packets (i.e., Fig. 1). Fig. 2 demonstrates that the width of a lamella on the plane of polish (w_o) is the true thickness of the lamella (w_o') divided by $\cos\phi$.

Therefore, assuming that all TiAl lamellae in the specimen have the same true thickness, measurement of the average apparent thickness of TiAl lamellae in a packet yields the absolute value of ϕ for that packet. The measurements to determine ψ and ϕ for the three lamellar packets listed in Table 1 were taken prior to compression creep testing.

4. Model

In Fig. 2, the applied compressive stress is defined in the specimen coordinate system (x_1, x_2, x_3). The x_1', x_2', x_3' coordinate system is associated with the lamellae within a packet. The heavy solid line represents the fiducial line passing through a lamella on the polished face (x_1, x_3 plane) of the compression creep specimen. The heavy dashed line is the projection of the fiducial line onto the x_1', x_3' plane. In the following calculations, the change in orientation of a fiducial line across a lamella, in response to an applied compressive stress, in the lamellae coordinate system will be determined and rotated into the x_1, x_2, x_3 coordinate system to yield the change in orientation of the fiducial line measured on the SEM micrographs.

The direction cosine matrix defining the rotation from the x_1, x_2, x_3 coordinate system to the x_1', x_2', x_3' coordinate system is:

$$a_{ij} = \begin{pmatrix} \cos \phi \cos \psi & \sin \phi & \cos \phi \sin \psi \\ -\sin \phi \cos \psi & \cos \phi & -\sin \phi \sin \psi \\ -\sin \psi & 0 & \cos \psi \end{pmatrix}. \quad (1)$$

Using the direction cosines, a strain state prescribed in the x_1, x_2, x_3 coordinate system, ϵ_{mn} , can be resolved in the x_1', x_2', x_3' coordinate system, ϵ_{pq}' , by:

$$\epsilon_{pq}' = a_{p'm} a_{q'n} \epsilon_{mn}. \quad (2)$$

For a uniaxial compressive stress, σ , applied along the x_3 axis, the resultant normal strains in the x_1, x_2, x_3 coordinate system can be determined assuming conservation of

volume during creep deformation:

$$\begin{pmatrix} 0 & 0 & 0 \\ 0 & 0 & 0 \\ 0 & 0 & -\sigma \end{pmatrix} = \begin{pmatrix} 0.5\epsilon_t & 0 & 0 \\ 0 & 0.5\epsilon_t & 0 \\ 0 & 0 & -\epsilon_t \end{pmatrix} \quad (3)$$

Using Eq. 1, 2 and 3, the strain components in the x_1', x_2', x_3' coordinate system can be expressed in terms of ϵ_t , the axial strain during uniaxial compression creep:

$$\begin{aligned} \epsilon_{11}' &= -\epsilon_t \left((\cos\phi \sin\psi)^2 - \frac{1}{2} (\cos^2\phi \cos^2\psi + \sin^2\phi) \right) \\ \epsilon_{12}' &= \epsilon_{21}' = \frac{3}{2} \epsilon_t \cos\phi \sin\phi \sin^2\psi \\ \epsilon_{13}' &= \epsilon_{31}' = -\frac{3}{2} \epsilon_t \cos\phi \sin\psi \cos\psi \\ \epsilon_{22}' &= -\epsilon_t \left((\sin\phi \sin\psi)^2 - \frac{1}{2} (\sin^2\phi \cos^2\psi + \cos^2\phi) \right) \\ \epsilon_{23}' &= \epsilon_{32}' = \frac{3}{2} \epsilon_t \sin\phi \sin\psi \cos\psi \\ \epsilon_{33}' &= -\epsilon_t \left(\cos^2\psi - \frac{1}{2} \sin^2\psi \right). \end{aligned} \quad (4)$$

The effect of each strain component in Eq. 4 on the orientation of the fiducial line will be calculated independently, and the net change in orientation of the fiducial line will be determined by summing the individual contributions.

Fig. 3 represents the change in shape of a volume element in a lamella under the influence of the compressive normal strain component ϵ_{33}' . Prior to application of this strain, the orientation of the fiducial line on the x_1', x_3' plane is defined by the angle θ_o' :

$$\tan\theta_o' = \frac{w_o'}{h_o'}. \quad (5)$$

The lengths h_o' and w_o' are parallel to the x_3' and x_1' axes, respectively. Since the x_3' axis lies in the x_1, x_3 plane, the projection of θ_o' onto the x_1, x_3 plane is:

$$\tan\theta_o = \frac{w_o'}{h_o'} \frac{1}{\cos\phi}, \quad (6)$$

where the initial orientation of the fiducial line on the plane of polish (x_1, x_3 plane) is given by the angle θ_o .

Similarly, the orientation of the fiducial line on the plane of polish after application of the compressive strain component ϵ_{33}' is defined as:

$$\tan\theta_{f33}' = \frac{w_1'}{h_1'} \frac{1}{\cos\phi}. \quad (7)$$

Assuming conservation of volume during plastic deformation, the strain components ϵ_{33}' and ϵ_{11}' are:

$$\epsilon_{33}' = \frac{h_1' - h_o'}{h_o'} \quad (8)$$

$$\epsilon_{11}' = -0.5\epsilon_{33}' = \frac{w_1' - w_o'}{w_o'}.$$

Combining Eq. 6, 7 and 8 yields an expression for θ_{f33}' :

$$\tan\theta_{f33}' = \left(\frac{2 - \epsilon_{33}'}{1 + \epsilon_{33}'} \right) \frac{\tan\theta_o}{2}. \quad (9)$$

The same procedure used to obtain Eq. 9 can be used to determine the new orientation of the fiducial line on the plane of polish after separate application of the

other compressive normal strain components, ε_{11}' and ε_{22}' :

$$\begin{aligned}\tan\theta_{f11}' &= \left(\frac{1+\varepsilon_{11}'}{2-\varepsilon_{11}'} \right) 2\tan\theta_o \\ \tan\theta_{f22}' &= \tan\theta_o.\end{aligned}\tag{10}$$

The present analysis reveals that the normal strain component ε_{22}' does not affect the orientation of the fiducial line.

Fig. 4 depicts the change in shape of a volume element, a cube of unit edge length, in a lamella under the influence of the shear strain components ε_{13}' and ε_{31}' . The end points of the fiducial line on the x_1', x_3' face of the volume element prior to straining are $(-1+d_o', 1)$ and $(-1, 0)$ in the x_1', x_2', x_3' coordinate system. Similarly, the end points of the fiducial line after application of ε_{13}' and ε_{31}' are $(-1-d_o'-\varepsilon_{13}', 1+\varepsilon_{31}'-\varepsilon_{31}'d_o')$ and $(-1, \varepsilon_{31}')$. Since the shear strain components ε_{13}' and ε_{31}' are equal, both shear strain components can be represented by ε_{13}' . Using this information and consulting Fig. 4, the orientations of the fiducial line on the plane of polish (x_1, x_3 plane) before and after imposition of the shear strain components can be expressed as:

$$\tan\theta_o = \frac{d_o'}{1} \frac{1}{\cos\phi},\tag{11}$$

and

$$\tan\theta_{f13}' = \frac{(d_o' - \varepsilon_{13}')}{(1 - \varepsilon_{13}'d_o')} \frac{1}{\cos\phi}.\tag{12}$$

Combining Eq. 11 and 12 yields the new orientation of the fiducial line on the plane of polish after application of the shear strain components ε_{13}' and ε_{31}' :

$$\tan\theta_{f13}' = \frac{(\tan\theta_o \cos\phi - \varepsilon_{13}')}{(1 - \varepsilon_{13}' \tan\theta_o \cos\phi)} \frac{1}{\cos\phi}.\tag{13}$$

Using similar procedures, the new orientation of the fiducial line on the plane of polish after the application of the other shear strain components, ϵ_{23}' and ϵ_{32}' , and ϵ_{12}' and ϵ_{21}' , can be determined:

$$\epsilon_{23}' \text{ and } \epsilon_{32}': \quad \tan\theta_{f23}' = \frac{\tan\theta_o}{\sqrt{1+(\epsilon_{23}')^2}} \quad (14)$$

$$\epsilon_{12}' \text{ and } \epsilon_{21}': \quad \tan\theta_{f12}' = \frac{\tan\theta_o \cos\phi \sqrt{1+(\epsilon_{12}')^2}}{\cos(\phi + |\epsilon_{12}'|)} \quad (15)$$

Adding the individual contributions to the change in fiducial line orientation given in Eq. 9,10,13,14 and 15, the change in orientation of the fiducial line on the plane of polish, $\Delta\theta$, after application of the compressive normal stress component σ_{33} in the x_1, x_2, x_3 coordinate system can be expressed as:

$$\Delta\theta = \theta_f - \theta_o = (\theta_{f33}' - \theta_o) + (\theta_{f11}' - \theta_o) + (\theta_{f13}' - \theta_o) + (\theta_{f23}' - \theta_o) + (\theta_{f12}' - \theta_o). \quad (16)$$

The formulation of Eq. 16 assumes that the individual contributions to the change in fiducial line orientation are small. Inserting the expressions in Eq. 4 into Eq. 16 results in an expression for $\Delta\theta$ as a function of the orientation parameters ψ and ϕ , the initial orientation of the fiducial line on the plane of polish, θ_o and the total strain of the sample after uniaxial compression creep testing, ϵ_t . Thus, by determining the orientation of a lamella and measuring the change in orientation of a fiducial line on a planar section through the lamella, ϵ_t for an individual lamella during the creep test can be found.

Eq. 9,10,13,14 and 15 were explicitly derived for positive values of ψ and ϕ . Deriving the corresponding expressions for negative values of ψ and ϕ reveals that $\Delta\theta$ has the same magnitude and sign for all combinations of positive and negative values of these variables. Therefore, for any ψ and ϕ (positive or negative) the value of

$\Delta\theta$ can be determined by inserting the absolute values of ψ and ϕ into the equations outlined in the present paper. Furthermore, the value of $\Delta\theta$ does not depend on the initial orientation of the fiducial line (i.e., left-bottom to right-top or right-bottom to left-top). Modifying the present analysis to treat tensile deformation instead of compressive deformation is quite straightforward.

5. Model Results

In Fig. 5, the predicted change in orientation of the fiducial line on the plane of polish ($\Delta\theta = \theta_f - \theta_o$) is plotted as a function of lamellar orientation with respect to the compression axis (ψ) and lamellar orientation away from the polished face of the specimen (ϕ). The plots were constructed using Eq. 4 and 16 for a total applied uniaxial compressive strain (ϵ_t) of 0.10 and four different values of the initial orientation of the fiducial line on the plane of polish (θ_o). Only the positive ranges of ψ and ϕ need to be represented since $\Delta\theta$ is symmetric for positive and negative values of these variables. Due to the singularity at $\phi = 90^\circ$, when the lamellar x_1, x_3 plane is perpendicular to the plane of polish (x_1, x_3 plane), the ϕ axis of the plots is terminated at 80° .

Figure 5 demonstrates that lamellar orientations associated with intermediate values of ψ and ϕ generally produce smaller rotations of the fiducial line than lamellar orientations at which at least one of the angles tends towards an extremity. Large values of ψ and ϕ produce negative rotations of the fiducial line ($\theta_f < \theta_o$) for a compressive uniaxial strain, whereas small values of ψ or large values of ϕ result in positive rotations of the fiducial line. Furthermore, Fig. 5 demonstrates that for the majority of lamellar orientations, the change in fiducial line orientation is greatest for an initial fiducial line orientation of 45° . The overall changes in fiducial line orientations are not very large. Therefore, to facilitate accurate measurement of the change in orientation of the fiducial line, samples should be tested to the highest possible strains, and the initial orientation of the fiducial line(s) should be inscribed at 45° with respect to the applied stress axis.

6. Discussion

The sixth and seventh columns of Table 1 contain the average strain of the TiAl and Ti₃Al lamellae in each of the three lamellar packets for which the fiducial line

analyses was conducted. The strains were determined using the measured values of θ , θ_f , ϕ , ψ and Eq. 4 and 16. The standard deviations of the strains are fairly large due to the relatively small changes in fiducial line orientation and the uncertainty involved in determining the orientations of the fiducial line across the lamellae after the creep test. The accuracy of the results could have been improved by inscribing the initial fiducial line closer to 45° , attaining a larger uniaxial creep strain, or performing the test in a better vacuum to minimize obscuring of the fiducial lines by oxidation.

The average strain of each lamellar packet during the compression creep test can be calculated by taking the weighted sum of the average strains of the TiAl and Ti₃Al lamellae:

$$\epsilon_{\text{lamellar}} = V_F \epsilon_{\text{TiAl}} + (1 - V_F) \epsilon_{\text{Ti}_3\text{Al}} \quad (17)$$

where, $\epsilon_{\text{lamellar}}$, ϵ_{TiAl} and $\epsilon_{\text{Ti}_3\text{Al}}$ represent the average strains of the lamellar packet and the TiAl and Ti₃Al lamellae, respectively. The volume fraction of the TiAl phase is V_F . The eighth column in Table 1 lists the value of $\epsilon_{\text{lamellar}}$ for each lamellar packet after the compression creep test. The cumulative standard deviations of the lamellar packet strains were calculated using statistical methods outlined in Ref. [9].

The average strain of the lamellar packets increases with increasing ψ . Several investigators have demonstrated that the creep rate of aligned fiber composites is anisotropic [10,11]. Calculations by Miles and McLean [10] demonstrate that fibers aligned parallel and perpendicular to the applied stress represent the upper and lower bound creep strength of fiber-reinforced composites. Extending these ideas to discontinuous aligned lamellar composites indicates that as the orientation of lamellae within a packet changes from $\psi = 0^\circ$ to $\psi = 90^\circ$, the creep rate of the lamellar packet should correspondingly increase. Therefore, the increase in average strain of the lamellar packets with increasing ψ can be rationalized in terms of the decreasing composite creep resistance as the lamellae are oriented away from the applied stress axis.

Since the two-phase TiAl/Ti₃Al lamellar specimen consists of randomly oriented lamellar packets, the strain of the lamellar specimen and the TiAl and Ti₃Al phases within the lamellar microstructure after the compression creep test can be approximated

by taking the mean of the values listed in columns 6, 7 and 8 in Table 1. The strain of the lamellar alloy and the constituent single-phase alloys within the lamellar microstructure determined using the fiducial line technique after creep testing at 1080 K and 380 MPa for 10.3 h, ϵ (fiducial line analysis), are listed in Table 2. Also listed is the value of strain determined by measuring the height of the lamellar specimen before and after the creep test, ϵ (creep specimen). The utility of the fiducial line technique is evidenced by the good agreement between ϵ (fiducial line analysis) and ϵ (creep specimen). The fiducial line experiment enables measurement of the deformation characteristics of the phases within the lamellar microstructure, a task that cannot be easily accomplished using alternate mechanical testing and microscopy techniques. The results in Table 2 demonstrate that the TiAl phase creeps approximately 2.2 times faster than the Ti₃Al phase within the lamellar microstructure during compression creep testing at 1080 K and 380 MPa .

By dividing the strains depicted in Table 2 by the duration of the creep test (10.3 hours), the creep rates of the lamellar specimen and the constituent single phases within the lamellar microstructure can be determined. These creep rates include both the primary and secondary creep strain regimes. Bartholomeusz, Yang and Wert [1] have reported that the two-phase TiAl/Ti₃Al lamellar alloy exhibits negligible primary creep strain; therefore, the creep rates obtained using the fiducial line experiment are expected to be approximately equal to the secondary, or minimum, creep rates. In a forthcoming paper the minimum creep rates of the TiAl and Ti₃Al phases within the lamellar microstructure will be compared with the minimum creep rates of the TiAl and Ti₃Al single-phase alloys obtained from compression creep tests, and a composite strengthening model will be developed to predict the creep behavior of the two-phase TiAl/Ti₃Al lamellar alloy by accounting for the creep properties of the constituent phases within the lamellar microstructure.

While not part of the present investigation, the fiducial line analysis can be used to determine the stress exponent and activation energy for creep of the phases within the lamellar microstructure by conducting fiducial line experiments at different stresses and temperatures. An additional important result of the fiducial line analysis is the information it yields on interphase interface sliding during mechanical testing. By evaluating the continuity of the fiducial line across the interphase interface after deformation, information regarding the extent of interfacial sliding can be obtained. In the two-phase TiAl/Ti₃Al alloy investigated in the present study, the fiducial lines were

always observed to be continuous across interphase interfaces indicating that interfacial sliding does not contribute to the creep deformation of this alloy within the resolution limit of the fiducial line experiment.

7. Conclusions

- (1) A fiducial line technique has been developed to determine the creep properties of the constituent phases within a lamellar composite subject to compression creep deformation. The technique can yield information on the total strain, creep rate and the stress exponent and activation energy for creep of the individual phases within a lamellar microstructure.
- (2) The contribution of interphase interfacial sliding to the strain of lamellar composites can also be evaluated using the fiducial line technique.
- (3) Application of the fiducial line analysis to a two-phase TiAl/Ti₃Al lamellar alloy deformed in compression at 1080 K and 380 MPa yields good agreement between the total creep strain of the specimen determined from the fiducial line analysis and the value directly measured from the crept specimen.

8. Acknowledgments

We would like to express our gratitude to Prof. E.F. Bartholomeusz for his thoughtful contributions to the present paper. This work was sponsored by AOFSR under contract number AOFSR-90-0143; Capt. C. Ward and Dr. A. Rosenstein were the contract monitors.

9. References

1. M.F. Bartholomeusz, Q. Yang and J.A. Wert, Creep deformation of a two-phase TiAl/Ti₃Al lamellar alloy and the individual TiAl and Ti₃Al constituent phases, *Scripta Metall. Mater.* 29:389-394 (1993).
2. A. Kelly and K.N. Street, Creep of discontinuous fiber composites II. Theory for the steady-state, *Proc. Roy. Soc. Lond.* 328A:283-293 (1972).
3. R.S. Polvani, W.-S. Tzeng and P.R. Strutt, High temperature creep in a semi-coherent NiAl-Ni₂AlTi alloy, *Metall. Trans.* 7A:33-40 (1976).
4. O.D. Sherby, R.H. Klundt and A.K. Miller, Flow stress, subgrain size, and subgrain stability at elevated temperature, *Metall. Trans.* 8A:843-850 (1977).
5. V.K. Vasudevan, M.A. Stucke, S.A. Court and H.L. Fraser, The influence of second phase Ti₃Al on the deformation mechanisms in TiAl, *Philos. Mag. Lett.* 59:299-307 (1989).
6. J.H. Van Der Merwe, G.J. Shiflet and P.M. Stoop, Structural ledges in interphase boundaries, *Metall. Trans.* 22A:1165-1175 (1991).
7. M. Larsen, A. Misra, S. Hartfield-Wunsch, R. Noebe and R. Gibala, *Ductility Enhancement From Interface Dislocation Sources in a Directionally Solidified $\beta + (\gamma + \gamma')$ Ni-Fe-Al Composite Alloy*, Proc. Int. Conf. on Intermetallic Matrix Composites, D.L. Anton, P.L. Martin, D.B. Miracle and R. McMeeking, eds., MRS, Pittsburgh, PA, pp. 191-198 (1989).
8. E.E. Underwood, Applications of quantitative metallography, in *Metals Handbook*, ASM, Metals Park, pp. 37-47 (1973).
9. J.R. Taylor, *An Introduction to Error Analysis*, University Science Books, California, (1982).
10. D.E. Miles and M. McLean, Anisotropic creep behavior of (Co,Cr)(Co,Cr)₇C₃ eutectic composite, *Metals Science* 11:563-570 (1977).
11. G. Gonzalez-Doncel and O.D. Sherby, High temperature creep behavior of metal matrix aluminum-SiC composites, *Acta Metall. Mater.* 41:2797-2805 (1993).

Table 1 Results of fiducial line analysis for the two-phase TiAl/Ti₃Al lamellar alloy compression crept at 1080 K under an applied stress of 380 MPa.

lamellar p #	$\Delta\bar{\theta}_{\text{TiAl}}$	$\Delta\bar{\theta}_{\text{Ti}_3\text{Al}}$	Ψ	ϕ	$\bar{\epsilon}_{\text{TiAl}}$	$\bar{\epsilon}_{\text{Ti}_3\text{Al}}$	$\bar{\epsilon}_{\text{lamellar}}$
1	5.2° (± 1.5°)	2.0° (± 1.1°)	0°	14°	0.091 (± 0.016)	0.034 (± 0.011)	0.071 (± 0.019)
2	1.7° (± 0.5°)	0.7° (± 0.5°)	30°	20°	0.095 (± 0.016)	0.041 (± 0.016)	0.077 (± 0.023)
3	-4.6° (± 1.5°)	-2.7° (± 1.5°)	60°	0°	0.100 (± 0.019)	0.058 (± 0.012)	0.085 (± 0.023)

Table 2 Comparison of creep strains determined from fiducial line analysis with the value directly measured from creep the specimen.

Material	ϵ_{tot} (fiducial line analysis)	ϵ_{tot} (creep specimen)
lamellar alloy	0.077 (± 0.012)	0.079
TiAl lamellae	0.096 (± 0.009)	-
Ti ₃ Al lamellae	0.044 (± 0.008)	-

List of Figures

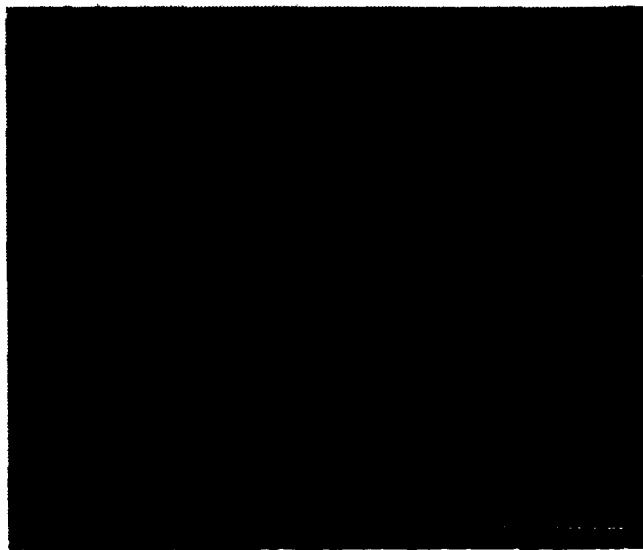
Figure 1. (a) SEM micrograph of fiducial lines on a surface of the lamellar alloy prior to compression creep testing. (b) Region "a" in micrograph (a) after compression creep testing at 1080 K under an applied compressive stress of 380 MPa to a true strain of 0.079. The arrows indicate the compression axis. The heavy dark line represents the orientation of the fiducial line prior to compression creep testing.

Figure 2. Relation between the specimen coordinate system (x_1, x_2, x_3) and the coordinate system of lamellae within a lamellar packet (x_1', x_2', x_3'). The orientation of lamellae with respect to the compression axis (x_3 direction) is given by the angle ψ . The angle ϕ defines the rotation of the lamellae away from the polished face of the specimen (x_1, x_3 plane).

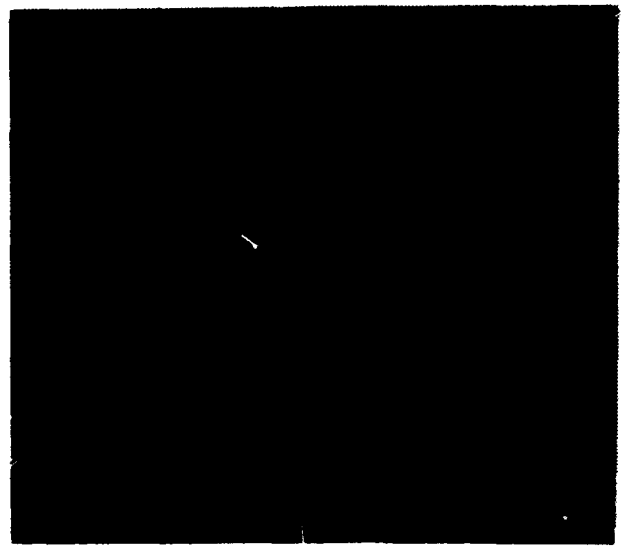
Figure 3. The change in shape of a volume element in a lamella under the influence of the compressive normal stress component σ_{33}' .

Figure 4. The change in shape of a volume element, a cube of unit length, in a lamella under the influence of the shear stress components σ_{13}' and σ_{31}' .

Figure 5. The predicted change in orientation of the fiducial line on the plane of polish plotted as a function of lamellar orientation for a total uniaxial compressive strain (ϵ_t) of 0.10 and for four different values of the initial orientation of the fiducial line on the plane of polish: (a) $\theta_0 = 15^\circ$. (b) $\theta_0 = 30^\circ$. (c) $\theta_0 = 45^\circ$. (d) $\theta_0 = 75^\circ$.



(a)



(b)

Figure 1. (a) SEM micrograph of fiducial lines on a surface of the lamellar alloy prior to compression creep testing. (b) Region "a" in micrograph (a) after compression creep testing at 1080 K under an applied compressive stress of 380 MPa to a true strain of 0.079. The arrows indicate the compression axis. The heavy dark line represents the orientation of the fiducial line prior to compression creep testing.

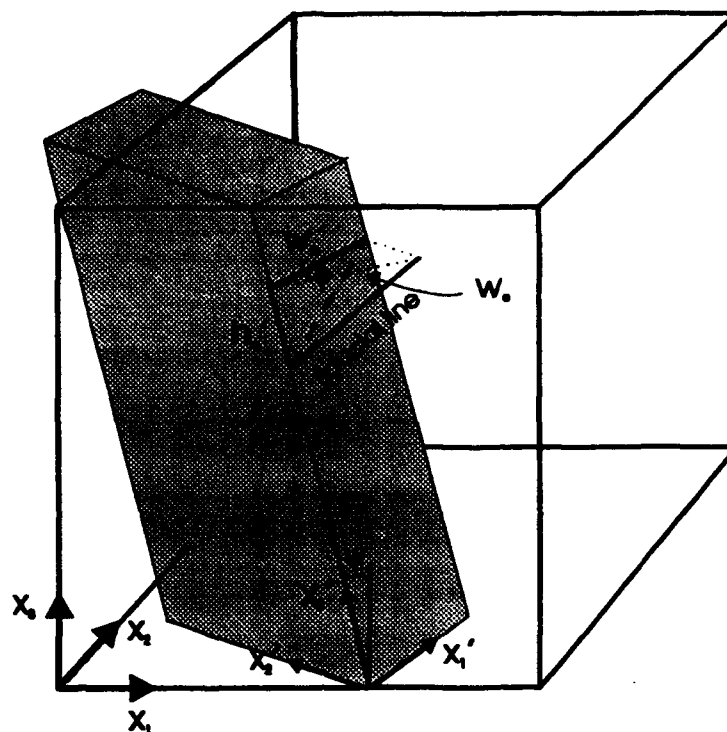


Figure 2. Relation between the specimen coordinate system (x_1, x_2, x_3) and the coordinate system of lamellae within a lamellar packet (x_1', x_2', x_3'). The orientation of lamellae with respect to the compression axis (x_3 direction) is given by the angle ψ . The angle ϕ defines the rotation of the lamellae away from the polished face of the specimen (x_1, x_3 plane).

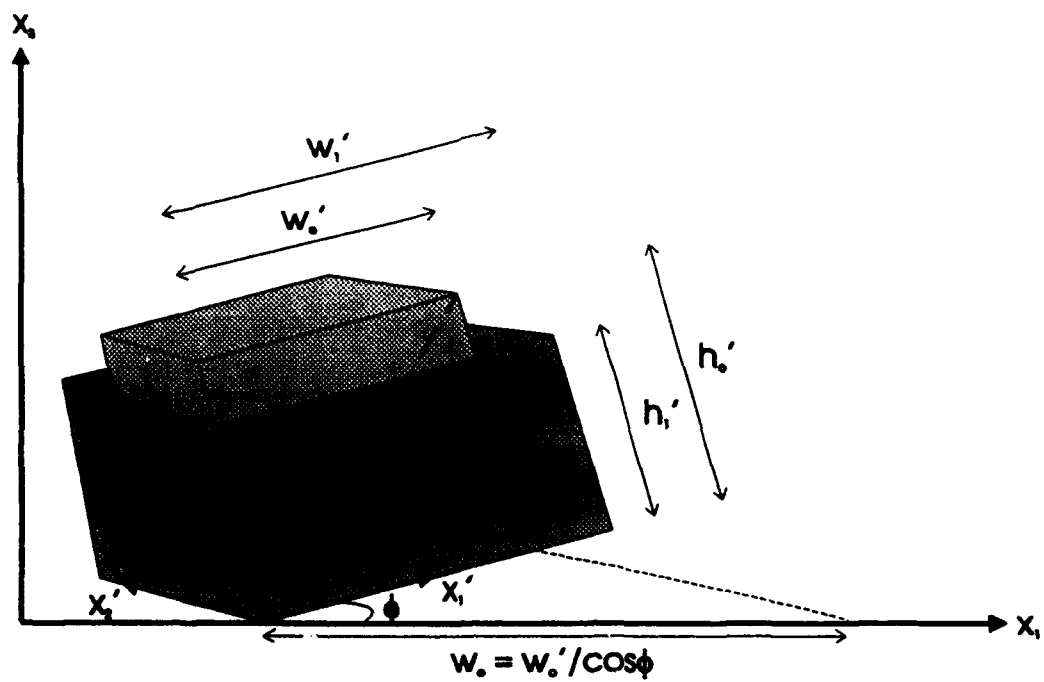


Figure 3. The change in shape of a volume element in a lamella under the influence of the compressive normal stress component σ_{33}' .

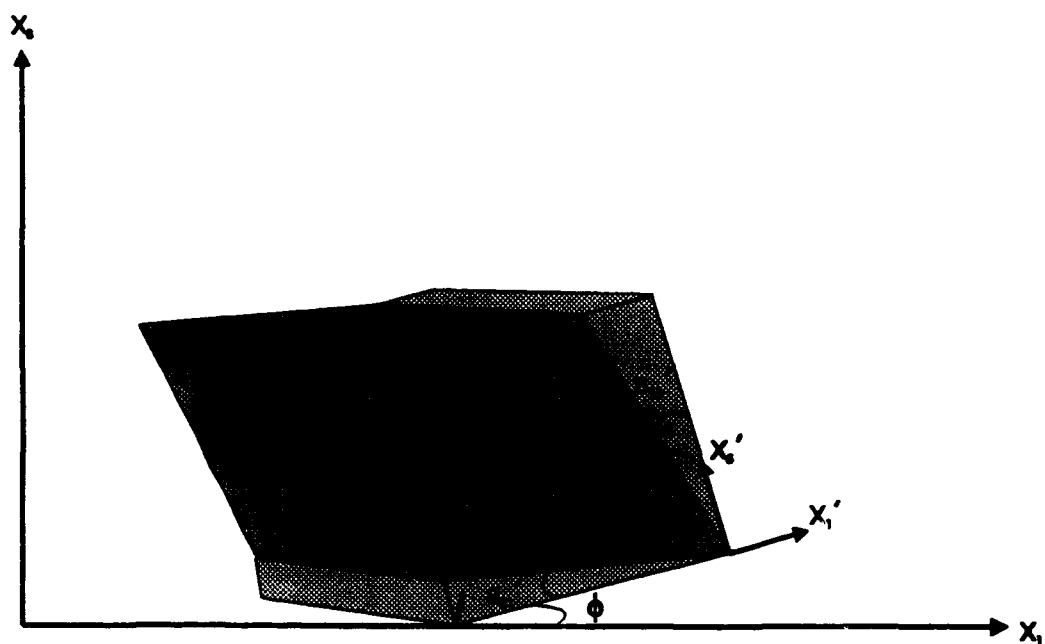


Figure 4. The change in shape of a volume element, a cube of unit length, in a lamella under the influence of the shear stress components $\sigma_{13'}$ and $\sigma_{31'}$.

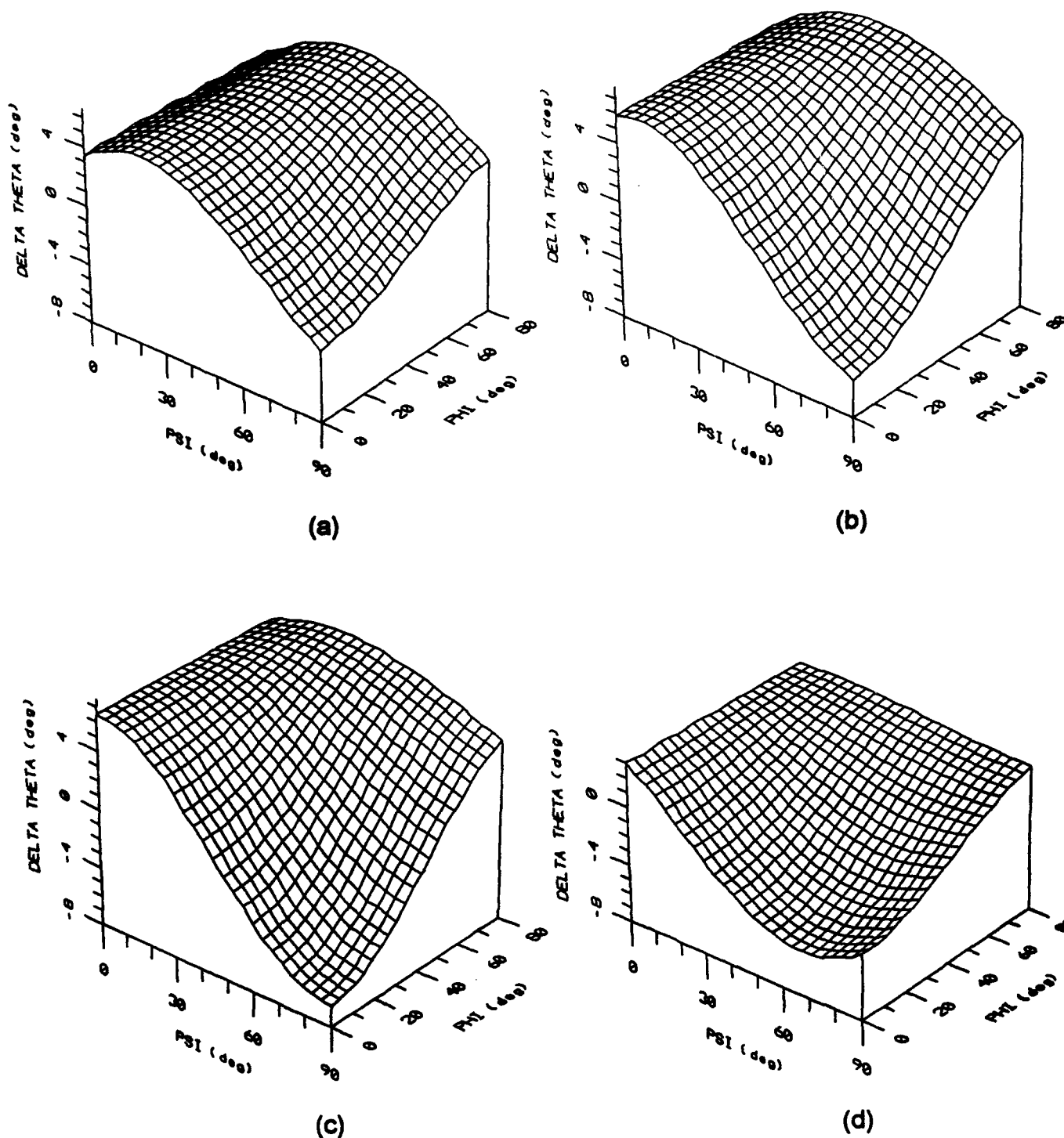


Figure 5. The predicted change in orientation of the fiducial line on the plane of polish plotted as a function of lamellar orientation for a total uniaxial compressive strain (ϵ_t) of 0.10 and for four different values of the initial orientation of the fiducial line on the plane of polish: (a) $\theta_0 = 15^\circ$. (b) $\theta_0 = 30^\circ$. (c) $\theta_0 = 45^\circ$. (d) $\theta_0 = 75^\circ$.

Chapter III

MODELING CREEP DEFORMATION OF A TWO-PHASE TiAl/Ti₃Al ALLOY WITH A LAMELLAR MICROSTRUCTURE

I. Introduction

The low density and good oxidation resistance of TiAl and Ti₃Al ordered intermetallic alloys make them attractive candidate materials for high temperature engineering applications [1, 2]. However, these alloys possess poor ductility at low and intermediate temperatures and are susceptible to rapid fatigue crack growth [1]. It has been shown by previous investigators that two-phase TiAl/Ti₃Al lamellar alloys exhibit an appreciably improved toughness and fatigue resistance compared to the constituent TiAl and Ti₃Al single-phase alloys [1, 3]. Furthermore, Bartholomeusz, Yang and Wert (BYW) [4] demonstrated that the minimum creep rate of a two-phase TiAl/Ti₃Al lamellar alloy (referred to as *the lamellar alloy* in the present paper) is lower than the creep rates of the constituent phases. The creep behavior of the TiAl/Ti₃Al lamellar alloy is not unique; several duplex alloys have been reported to possess lower creep rates than their constituent phases, most notably NiAl/Ni₂AlTi and γ/γ' nickel-base superalloys [5-7]. It has been proposed that this phenomenon is a general one associated with duplex alloys possessing semicoherent interfaces [5].

Polvani *et al.* [5] suggested that the lower creep rate of the duplex NiAl/Ni₂AlTi alloy with respect to its constituent phases is due to the retardation of dislocation climb at semicoherent interfaces separating the two phases. It is possible that such a mechanism is occurring in the TiAl/Ti₃Al lamellar alloy, but alternate mechanisms could also account for the experimental observations. For example, the phases in the lamellar microstructure may possess lower steady-state creep rates than the corresponding constituent single-phase alloys as a result of enhanced work hardening. Power-law creep can be regarded as a competition between recovery and work hardening [8, 9]. When a balance is achieved between these two processes, the material exhibits steady-state creep. Therefore, an increase in the work hardening rate, or a reduction in the recovery rate, can have the effect of reducing the steady-state creep rate.

In a study of the elevated-temperature deformation characteristics of TiAl and Ti₃Al alloys, Rao and Tangri [10] found that the alloys with lamellar microstructures exhibit substantially higher work hardening rates than the single-phase alloys. There are several potential explanations for the higher work hardening rates of TiAl and Ti₃Al within the lamellar microstructure. First, the interphase interfaces may provide a high density of dislocation sources in the lamellar alloy, as described by Appel et al. [11]. Second, segregation of interstitial impurities from the TiAl phase to the Ti₃Al phase has been reported to significantly increase slip and twin activity in the TiAl phase [12]. Finally, enrichment of impurities in the Ti₃Al phase appears to enhance slip in this phase; specifically, the basal plane is rendered more favorable for slip [13]. Assuming that the recovery rate is less sensitive to the lamellar character of the microstructure than the work hardening rate, the increased density of dislocations and dislocation sources in the TiAl and Ti₃Al phases within the lamellar microstructure would cause the lamellar alloy to exhibit a lower creep rate than the individual constituent phases. This conjecture is consistent with Weertman's model for power-law creep [14] in which the steady-state creep rate is inversely proportional to the density of dislocation sources.

In the results reported by BYW, the grain sizes of the TiAl and Ti₃Al alloys tested were 230 and 280 μm , respectively. For these grain sizes and at low to intermediate values of applied stress, TiAl has a lower minimum creep rate than Ti₃Al at the same temperature and applied stress. Oikawa and coworkers [15, 16] conducted several creep tests on single-phase TiAl alloys possessing different grain diameters and found a strong dependence of minimum creep rate on grain size. Inspection of Oikawa's results reveals that TiAl alloys with 32 μm grain diameter always exhibit a higher minimum creep rate than the Ti₃Al alloy tested by BYW at the same temperature and applied stress. The average dimension of the TiAl phase within the lamellar microstructure is 37 μm . It is not known whether the grain size effect on the steady-state creep rate of TiAl carries through to the lamellar microstructure.

The preceding summary of prior observations demonstrates that the mechanism(s) underlying the superior creep properties of the TiAl/Ti₃Al lamellar alloy are not understood. The objective of the present paper is to characterize the creep behavior of the TiAl and Ti₃Al phases within the lamellar microstructure, and to demonstrate that the steady-state creep rate of the lamellar alloy can be predicted using a composite strengthening model. Sections II through IV are devoted to experimental determination of the creep behavior of the TiAl and Ti₃Al constituent

phases within the lamellar microstructure. These experimental results are then used in a creep strength model developed in the remaining sections of the paper.

II. Experimental Methods

Details concerning preparation of the alloys used in this study have been previously reported [4]. To characterize the creep behavior of the constituent TiAl and Ti₃Al phases within the lamellar microstructure, the following experiments were conducted. One face of a compression creep specimen, measuring 1.5 x 1.5 mm² x 2 mm, was polished using 0.05 μ m alumina powder. By carefully touching the polished face of the specimen to a spinning polishing wheel containing 1 μ m alumina powder, an array of fine fiducial lines was scratched onto the surface. The scratched face was lightly etched to enable secondary electron imaging of the polished surface in the scanning electron microscope (SEM). Careful measurements were taken with respect to the initial orientations and positions of several of the fiducial lines. The sample was then crept in compression at 1080 K in a vacuum hot press under an average applied stress of 350 MPa for 7 hours. The total true strain of the sample at the end of the test was 0.044. The same preparation procedure was used for a second sample, which was crept in compression at 1080 K under an average applied stress of 380 MPa for 10.3 hours. The total true strain at the end of this test was 0.079. To prevent oxidation from obscuring the fiducial lines, these tests were conducted in a vacuum hot press instead of the creep test fixture used to obtain the creep data presented by BYW. After testing, the orientations and positions of the fiducial lines were recorded using the SEM. Reference [17] presents a detailed account of the fiducial line experiment and its interpretation in the case of the lamellar sample deformed to a true strain of 0.079.

III. Experimental Results

Figure 1 is an optical micrograph of the lamellar alloy prior to testing. Each packet in the lamellar alloy consists of alternating TiAl and Ti₃Al lamellae. The darker lamellae are TiAl phase which constitutes 64 volume percent of the alloy. The average packet diameter is 70 μ m and the true thickness of the TiAl lamellae is 3.3 μ m. Thus, the average dimension of the TiAl phase is approximately 37 μ m. BYW reported that, over large stress and temperature ranges, the minimum creep rate of the two-phase TiAl/Ti₃Al lamellar alloy is lower than the minimum creep rates of either of the constituent single-phase alloys. Figure 2 illustrates the results of BYW [4] and Oikawa

[15] for creep tests at 1080 K. The grain sizes of the samples used to obtain the creep properties represented in Figure 2 are: TiAl tested by BYW, 230 μm ; Ti_3Al tested by BYW, 280 μm ; and TiAl tested by Oikawa, 32 μm . The values of minimum creep rate for the lamellar alloy in Figure 2 were obtained at true strains less than 0.05.

Figure 3a is a SEM micrograph of a portion of the polished specimen face containing fiducial lines, prior to testing to a true strain of 0.044. The width of the fiducial lines is significantly smaller than the width of the TiAl and Ti_3Al lamellae, ensuring accurate observation of the deformation of the fiducial lines within the phases and at the interphase interfaces. Figure 3b is a SEM micrograph of the fiducial lines after compression creep testing to a true strain of 0.044. The darker and mottled phase in the SEM micrographs is the TiAl phase; its mottled appearance is an artifact of the etching process. The fiducial lines are clearly continuous across interphase interfaces and are also continuous across lamellar packet boundaries. The displacement of the fiducial lines within the constituent phases of the lamellar alloy tested to a true strain of 0.044 was very slight and quantitative determination of the local strains necessitated evaluation of the lamellar alloy crept to a true strain of 0.079 [17].

Figure 4a is a SEM micrograph of a portion of the polished specimen face containing a fiducial line prior to testing to a true strain of 0.079 [17]. The fiducial line in Figure 4a is 58.5° from the compression axis and is straight within the resolution limit of the fiducial line experiment. Figure 4b depicts the same fiducial line, passing through the lamellar packet marked "a" in Figure 4a, after creep testing to a true strain of 0.079. The orientation of the fiducial line prior to testing is marked on Figure 4b. In the bottom left corner of Figure 4b, the two lines almost coincide. However, in the top right corner of Figure 4b there is a significant difference in the positions of the two lines and the orientation of the fiducial line is noticeably different in the two phases. After testing, the fiducial lines are continuous across interphase interfaces.

Although the creep test was conducted in a vacuum hot press, the vacuum during the test was not better than 5 Pa. Furnace debris and some limited oxidation marred the surface of the sample tested to a true strain of 0.079 and permitted evaluation of only those lamellar packets for which the position of the fiducial line could be positively discerned. In all, three lamellar packets possessing lamellae orientations ranging from 0° to 60° with respect to the compression axis were evaluated [17]. The second and third columns in Table 1 depict the average change in orientation of the

fiducial line with respect to the compression axis in the TiAl and Ti₃Al lamellae within the three lamellar packets. The change in orientation of the fiducial line in the TiAl phase was always greater than the change in orientation of the fiducial line in the Ti₃Al phase. This result demonstrates that the TiAl phase strained more during the creep test, and therefore the TiAl phase in the lamellar microstructure exhibits a higher creep rate than the Ti₃Al phase in the lamellar microstructure.

IV. Interpretation of Experimental Results

Evaluation of the orientations of the fiducial lines in the two phases within the lamellar microstructure demonstrates that, under the same external stress, the TiAl phase in the lamellar microstructure creeps more rapidly than the Ti₃Al phase in the lamellar microstructure. This conflicts with previously reported observations of the creep rates of single-phase TiAl and Ti₃Al which show that coarse-grain TiAl creeps less rapidly than coarse-grain Ti₃Al at the same stress and temperature, for low to intermediate values of applied stress [4]. Several factors could account for this difference. For example, the effective dimensions of the phases in the lamellar alloy are much smaller than the grain sizes of the single-phase alloys. Oikawa *et al.* [15, 16] have shown that reducing the grain size of TiAl increases the steady-state creep rate in the temperature and stress regime used in the present study. However, if reduced grain size increases the creep rate of TiAl, it is even more difficult to understand the low creep rate of the lamellar alloy. The grain size dependence of creep rate for Ti₃Al has not been reported, so it is not possible to identify the role of grain size in this case.

Alloy stoichiometry is known to affect creep of TiAl and Ti₃Al [4, 15, 16, 18,19]. However, in the present study, the single-phase alloy compositions were selected to match closely the compositions of the two phases in the lamellar alloy. Therefore, it is unlikely that the low creep rate of the lamellar alloy can be accounted for by alloy stoichiometry.

Since considerations of grain size and phase stoichiometry are unable to explain the creep behavior of the lamellar alloy, further analysis of the fiducial line experiments is necessary. Bartholomeusz and Wert [17] have described an analysis that relates the change in orientation of the fiducial line in each phase ($\Delta\theta$ values in Table I) to the strain in the individual phases. The information required to perform the analysis is derived completely from measurements on the plane of polish: the true and apparent

lamellar thickness, the angle (on the plane of polish) between the interphase interface and the compression axis (ψ), and the angle between the fiducial line and the compression axis before and after creep testing. Since the analysis method is the subject of a separate paper [17], the details are not repeated here. The results of the analysis are shown in Table I, which lists the value of ψ and the average strains determined for the individual phases within three different lamellar packets ($\bar{\epsilon}_{\text{TiAl}}$ and $\bar{\epsilon}_{\text{Ti}_3\text{Al}}$). The term *average strain* signifies that $\Delta\theta$ values for all TiAl and Ti_3Al lamellae traversed by the fiducial line within a single packet were averaged to obtain values of $\bar{\epsilon}_{\text{TiAl}}$ and $\bar{\epsilon}_{\text{Ti}_3\text{Al}}$. Finally, the strain of the individual lamellar packets ($\bar{\epsilon}_{\text{lamellar}}$) was obtained from the fiducial line analysis by invoking a rule of mixtures argument; these values are listed in the last column of Table I.

The results of the fiducial line analysis show that the strain of the lamellar packets increases with increasing ψ . This result is a reflection of the anisotropy of the creep resistance of lamellae having different orientations with respect to the applied stress. Lamellae inclined at 60° with respect to the applied stress strain about 20% more than lamellae oriented parallel to the applied stress. The strain of the lamellar specimen possessing randomly oriented lamellar packets can be approximated by the average strain of the three lamellar packets evaluated in Table I [17], which gives an average strain of 0.077. The strain measured directly from the crept specimen was 0.079. Since the macroscopic strain measured directly from the specimen is not used in the fiducial line analysis, these assessments of the overall strain are independent and the close agreement provides confidence in the fiducial line analysis method. From the duration of the creep test and the strain values listed in Table I, the average creep rates for the constituent phases within the lamellar microstructure and the average creep rate of the lamellar alloy can be calculated. Previous results indicate that the lamellar alloy exhibits a negligible amount of primary creep strain [4, 20]. Therefore, the creep rates obtained from the fiducial line analysis are approximately equal to the secondary, or minimum, creep rates.

Table II presents the average creep rates of the lamellar alloy and the TiAl and Ti_3Al phases within the lamellar microstructure determined using the fiducial line method ($\dot{\epsilon}$ [fiducial line results]), and the creep rates of the lamellar alloy and single-phase TiAl and Ti_3Al alloys obtained from compression creep tests ($\dot{\epsilon}$ [creep tests]). The minimum creep rate values for the lamellar alloy measured using the two different

techniques are in good agreement. The creep rate determined from the fiducial line analysis is slightly higher, probably due to the incorporation of a small amount of primary creep strain in the calculation. However, the most significant result in Table II is that the creep rates of the constituent phases in the lamellar microstructure are more than an order of magnitude lower than the same phases tested as single-phase alloys.

Polvani and coworkers [5] reported that the overwhelming majority of dislocations in a NiAl/Ni₂AlTi duplex alloy were contained within interfacial networks. Very few dislocations were present within the single-phase regions. They consequently proposed that the lower creep rate of the NiAl/Ni₂AlTi duplex alloy relative to its constituent phases was due to the emission and absorption rates of dislocations by the interfacial dislocation networks. By acting as physical barriers to dislocation climb, the interfacial dislocation networks were proposed to endow the duplex alloy with a lower creep rate than its constituent phases. There are two observations which suggest that a different mechanism controls the lower creep rate of the TiAl/Ti₃Al lamellar alloy with respect to its constituent phases.

First, the average separation between interphase interfaces in the lamellar alloy is 2.6 μm , more than an order of magnitude greater than the average interfacial network separation in the NiAl/Ni₂AlTi duplex alloy [5]. The larger interface separation in the TiAl/Ti₃Al lamellar alloy suggests that a significant fraction of climbing dislocations would not encounter an interphase interface during creep to a strain of 0.08. This indicates that the role of the interfaces in blocking dislocation climb is unlikely to be as dominant an effect in the TiAl/Ti₃Al lamellar alloy as it is in the NiAl/Ni₂AlTi duplex alloy.

Second, Rao and Tangri [10] reported that the lamellar alloy exhibits a higher work hardening rate than the constituent phases. As described in the introduction, the higher work hardening rate can be directly related to the lower steady state creep rates of the constituent phases in the lamellar microstructure. While the microstructural origin(s) of the higher work hardening rate have not been verified, dislocation climb inhibition by interfacial boundaries is an unlikely explanation for the 10-fold increase in the work hardening rate over a broad temperature range.

Irrespective of the origin of the enhanced work hardening of the TiAl and Ti₃Al phases in the lamellar morphology, it is possible to define hardening factors (χ) for

each phase:

$$\chi_{\gamma} = \frac{\dot{\epsilon}_{\gamma}[\text{lamellar}]}{\dot{\epsilon}_{\gamma}[\text{single-phase}]} \quad (1)$$

$$\chi_{\alpha 2} = \frac{\dot{\epsilon}_{\alpha 2}[\text{lamellar}]}{\dot{\epsilon}_{\alpha 2}[\text{single-phase}]}$$

where $\dot{\epsilon}_{\gamma}[\text{lamellar}]$ and $\dot{\epsilon}_{\alpha 2}[\text{lamellar}]$ represent the average creep rates of the TiAl and Ti₃Al phases within the lamellar microstructure and $\dot{\epsilon}_{\gamma}[\text{single-phase}]$ and $\dot{\epsilon}_{\alpha 2}[\text{single-phase}]$ represent the creep rates of the corresponding single-phase alloys. For an applied compressive stress of 380 MPa at 1080 K, the hardening factors have values of 23 and 17 for the TiAl and Ti₃Al phases, respectively.

The constitutive relationships for compression creep of the single-phase TiAl and Ti₃Al alloys in the present investigation have been determined over ranges of stress and temperature [4, 15]. The single-phase alloys exhibit power-law creep behavior. Owing to the difficulty of the fiducial line experiment, however, the hardening factors have been evaluated for creep at a single stress and temperature. Making the simplistic assumption that the hardening factors are not affected by the applied stress and temperature, constant hardening factors can be incorporated into the constitutive relationships reported previously for creep of TiAl and Ti₃Al to give constitutive relationships for the two phases within the lamellar microstructure. In the remainder of this paper, a composite strengthening model is developed to predict the minimum creep rate of the lamellar alloy as a function of stress and temperature, using the constitutive relationships that include the appropriate hardening factors.

V. Model

Kelly and Street (KS) [21] modeled steady-state creep deformation of a composite containing uniaxially aligned discontinuous fibers. The basic premise of the KS model is that bonding at the matrix/reinforcement interface results in the retardation

of creep in the matrix phase adjacent to the interphase interface. The lower creep rate of the matrix adjacent to the interface produces a shear stress across the interface, resulting in load transfer from the matrix to the reinforcements. Sliding of the interface is also taken into account in the KS model. Application of the KS model to several metal matrix composite systems revealed good agreement between model predictions of composite creep properties and experimental results [21-24].

Each packet in the TiAl/Ti₃Al lamellar alloy consists of alternating plates, or lamellae, of TiAl and Ti₃Al; a geometry different from that modeled by KS. In the present paper, the KS analysis is presented in modified form to specifically address steady-state creep of a lamellar microstructure consisting of randomly oriented lamellar packets. In a lamellar microstructure with similar volume fractions of the two phases, the morphologies of the reinforcing and matrix phases are virtually identical. For model development, it is convenient to use the terms *matrix* and *reinforcement*, even though the concept of a continuous matrix phase may not be applicable to the lamellar microstructure.

The effect of the reinforcing phase on retardation of flow in the matrix is a maximum for lamellae oriented parallel to the applied stress. In contrast, when the lamellae are oriented normal to the applied stress, the reinforcing phase does not significantly constrain flow of the matrix phase. Therefore, lamellar packets oriented parallel and perpendicular to the applied stress represent the upper and lower creep strength bounds for the lamellar alloy [25, 26]. In the remainder of Section V of the present paper, the KS model is adapted for use with the lamellar phase morphology. The two limiting cases are considered first, followed by the general case. Figure 5 depicts the two limiting cases; $\dot{\epsilon}_m$ and $\dot{\epsilon}_r$ represent displacement rates in the matrix and reinforcing phases respectively. In Figure 5a, the combined effect of the reinforcement displacement rate and the interfacial sliding velocity, $\dot{\epsilon}_s$, is represented by $\dot{\epsilon}_i$.

A. Discontinuous lamellae oriented parallel to the uniaxial stress

For lamellae oriented parallel to a uniaxial stress, the matrix and reinforcing phases are required to strain at the same rates. The strength of such a lamellar composite, σ_c , can be expressed in terms of the average strength of the discontinuous reinforcing lamellae, $\bar{\sigma}_r$, the strength of the matrix phase, σ_m , and the volume fractions

of the respective phases, V_r and V_m :

$$\sigma_c = \bar{\sigma}_r V_r + \sigma_m V_m. \quad (2)$$

In the context of creep deformation, strength signifies the stress required to maintain a constant creep rate at a given temperature. Evaluation of the term describing the average stress in the discontinuous reinforcing lamellae is fairly involved. The original Kelly and Street [21] model outlines a procedure for evaluating this stress in the case of uniaxially aligned discontinuous fibers. In the following paragraphs, the salient steps of a similar derivation for the case of uniaxially aligned discontinuous lamellae are described.

As in the original KS analysis, the difference in displacement rate of the matrix at the interphase interface and at a distance h from the interface is:

$$\Delta v = \dot{u}_m - \dot{u}_i \quad (3)$$

where

$$\dot{u}_m = \dot{\epsilon}_m z$$

$$\dot{u}_i = \dot{u}_r + \dot{u}_s$$

$$\dot{u}_s = \eta(\dot{u}_m - \dot{u}_r)$$

and z is distance measured parallel to the interface (see Figure 5a). The factor η varies between 1 and 0, depending on whether interfacial sliding occurs or not. The experimental results described in Section III of the present paper show that no detectable interfacial sliding occurs in the TiAl/Ti₃Al lamellar alloy for the true strains tested; therefore, we take $\eta = 0$. The displacement rate gradient in the matrix results in a shear strain rate adjacent to the interface, given by:

$$\dot{\gamma} = \frac{\Delta v}{h} = \frac{\dot{\epsilon}_m z - \dot{u}_r}{h} \quad (4)$$

where h is half of the thickness of the matrix lamellae. The parameter h can be

expressed as:

$$h = \frac{t(1 - V_r)}{2V_r} \quad (5)$$

where t is the thickness of the reinforcing lamellae. In Eq. 5, h is inversely proportional to the volume fraction of the reinforcing phase, whereas in the original KS model h is inversely proportional to the square root of the volume fraction of the reinforcing phase. Since V_r is a fractional quantity, for the same volume fraction of reinforcing phase, the shear strain rate in the matrix of a fiber-reinforced composite is greater than that in a lamellar composite.

The relationship between tensile stress (σ_m) and creep rate ($\dot{\epsilon}_m$) for the matrix phase undergoing power-law creep is [21]:

$$\sigma_m = \sigma_{mo} \left(\frac{\dot{\epsilon}_m}{\dot{\epsilon}_{mo}} \right)^{1/n} \quad (6)$$

where n is the stress exponent of the matrix phase, and σ_{mo} and $\dot{\epsilon}_{mo}$ are temperature dependent parameters. Using the relations $\sigma_m = 2\tau$, where τ is the local shear stress, and $\dot{\epsilon}_m = (2/3)\dot{\gamma}$ [21], the shear stress dependence on shear strain rate can be expressed as:

$$\dot{\gamma} = \frac{3}{2} \dot{\epsilon}_{mo} \left(\frac{2\tau}{\sigma_{mo}} \right)^n \quad (7)$$

Combining Eq. 4 through 7 yields:

$$\tau = \beta' \sigma_{mo} (t \dot{\epsilon}_{mo})^{-1/n} (\dot{\epsilon}_m Z - \dot{u}_r)^{1/n} \quad (8)$$

where

$$\beta' = \frac{1}{2} \left(\frac{4}{3} \right)^{1/n} \left(\frac{V_r}{1 - V_r} \right)^{1/n}$$

Eq. 8 is the constitutive equation that represents the shear stress acting on any part of the reinforcing lamellae surface.

Figure 6 summarizes several approximations made in determining the creep rate of the reinforcing lamellae. The length of the lamellae is defined by the parameter L . Away from the ends of the reinforcing lamellae, $z < z_c$, the reinforcement and matrix phases are constrained to have the same creep rate, $\dot{\epsilon}_r = \dot{\epsilon}_m$. Creep of the reinforcing phase occurs slowly near the ends, $z > z_c$, because load transfer across the interface is insufficient to develop a high stress at the lamellae ends. The parameter z_c represents the critical length for maximum load transfer to the reinforcing lamellae. Kelly and Street [21] demonstrated that the transition between these two creep regimes is very steep for a reinforcing phase stress exponent, n , greater than 4. This is the case for the reinforcing phase in the TiAl/Ti₃Al lamellar alloy [4], which indicates that treating the transition in creep rate of the reinforcing phase as a step function is reasonable.

Substituting $\dot{\epsilon}_r = \dot{\epsilon}_m z$ for $z < z_c$ and $\dot{\epsilon}_r = \dot{\epsilon}_m z_c$ for $z > z_c$ into Eq. 8 results in the following:

$$\tau = 0 \quad \text{for } z < z_c \quad (9a)$$

$$\tau = \beta' \sigma_{mo} \left(\frac{\dot{\epsilon}_m}{\dot{\epsilon}_{mo}} \right)^{1/n} \left(\frac{z - z_c}{d} \right)^{1/n} \quad \text{for } z > z_c. \quad (9b)$$

For $z > z_c$, a force balance allows the relationship between the shear and tensile stresses to be developed, as shown in Figure 7:

$$wt\delta\sigma_r = 2\tau(w + t)\delta z. \quad (10)$$

The width of the reinforcing lamellae is defined by the parameter w . If the factor $\delta\sigma_r$ for reinforcing lamellae is compared with the corresponding expression for reinforcing fibers of diameter t [21], it is apparent that the tensile stresses developed in the lamellae are approximately a factor of two less than those developed in the fibers. The expressions given in Eq. 5 and Eq. 10 demonstrate that stress transfer to reinforcing lamellae is not as effective as stress transfer to reinforcing fibers [21]. This is a direct consequence of the greater surface to volume ratio associated with the fiber geometry.

Integrating $\delta\sigma_r$ for the case of τ given by Eq. 9b yields:

$$\begin{aligned}\sigma_r &= -2 \int_{L/2}^z \tau \left(\frac{1}{\tau} + \frac{1}{w} \right) dz \\ &= 2\beta' \frac{n}{n+1} \sigma_{mo} \left(\frac{\dot{\epsilon}_m}{\dot{\epsilon}_{mo}} \right)^{1/n} \left(1 + \frac{t}{w} \right) \left[\left(\frac{L'}{t} \right)^{(n+1)/n} - \left(\frac{z - z_c}{t} \right)^{(n+1)/n} \right] \quad (11)\end{aligned}$$

where

$$\frac{L'}{2} = \frac{L}{2t} - \frac{z_c}{t}.$$

Evaluating Eq. 11 at $z = z_c$ yields the maximum value of σ_r , σ'_r , which represents the tensile stress in the reinforcing lamellae for $z < z_c$:

$$\sigma'_r = 2\beta' \frac{n}{n+1} \sigma_{mo} \left(\frac{\dot{\epsilon}_m}{\dot{\epsilon}_{mo}} \right)^{1/n} \left(1 + \frac{t}{w} \right) \left(\frac{L'}{t} \right)^{(n+1)/n} \quad \text{for } z < z_c. \quad (12)$$

For $z > z_c$, σ_r monotonically decreases from its maximum value at $z = z_c$ to 0 at the reinforcing plate end. Therefore, the average value of σ_r in the interval z_c to $L/2$, σ''_r , can be calculated by integrating the expression for σ_r given by Eq. 11:

$$\sigma''_r = \int_{z_c}^{L/2} \left(\frac{L}{2} - z_c \right)^{-1} \sigma_r dz \quad \text{for } z > z_c. \quad (13)$$

Evaluating this integral results in the following expression for σ''_r :

$$\sigma''_r = 2\beta' \frac{n}{2n+1} \sigma_{mo} \left(\frac{\dot{\epsilon}_m}{\dot{\epsilon}_{mo}} \right)^{1/n} \left(1 + \frac{t}{w} \right) \left(\frac{L'}{t} \right)^{(n+1)/n} \text{ for } z < z_c. \quad (14)$$

The aggregate average tensile stress on the entire reinforcing lamellae can be determined by combining Eq. 12 and Eq. 14 and taking into account the fraction of the lamellae length each stress acts on:

$$\bar{\sigma}_r = \frac{2z_c}{L} \sigma'_r + \frac{1-2z_c}{L} \sigma''_r. \quad (15)$$

The only parameter left to determine in Eq. 15 is z_c . As described previously, $\sigma_r = \sigma'_r$ at $z = z_c$. In an expression similar to Eq. 6, the creep rate of the reinforcing phase undergoing power-law creep can be described by:

$$\sigma_r = \sigma_{ro} \left(\frac{\dot{\epsilon}_r}{\dot{\epsilon}_{ro}} \right)^{1/n}. \quad (16)$$

Combining Eq. 12 and Eq. 16 yields:

$$z_c = \frac{L}{2} - t \left(\frac{(\dot{\epsilon}_m)^{(1/n-1/n)}}{2\beta'} \frac{n+1}{n} \frac{\sigma_{ro}}{\sigma_{mo}} \frac{(\dot{\epsilon}_{mo})^{1/n}}{(\dot{\epsilon}_{ro})^{1/n}} \frac{w}{w+t} \right)^{n/(n+1)}. \quad (17)$$

Thus, expanding Eq. 15 results in the final expression for the average tensile stress on the reinforcing plate.

Substituting the expression for the average tensile stress on the reinforcing plate into Eq. 2 results in a general constitutive relationship for the strength of a uniaxially

aligned discontinuous lamellar composite:

$$\sigma_c = \sigma_{mo} \left(\frac{\dot{\epsilon}_m}{\dot{\epsilon}_{mo}} \right)^{1/n} \frac{2t}{L} \left(1 + \frac{t}{L} \right) \left[\lambda 2^{1/n} \left(\frac{L'}{t} \right)^{(2n+1)/n} + 2\beta' \frac{n}{n+1} \left(\frac{L'}{t} \right)^{(n+1)/n} \left(\frac{L}{2t} - \frac{L'}{t} \right) \right] V_r$$

$$+ \sigma_{mo} \left(\frac{\dot{\epsilon}_m}{\dot{\epsilon}_{mo}} \right)^{1/n} (1 - V_r) \quad (18)$$

where

$$\lambda = \left(\frac{2}{3} \right)^{1/n} \frac{n}{2n+1} \left(\frac{V_r}{1-V_r} \right)^{1/n}.$$

The composite strength, σ_c , is dependent on the matrix creep rate, $\dot{\epsilon}_m$, which is modified by the presence of the reinforcing phase. Therefore, σ_c represents the stress required to deform the composite at a creep rate given by $\dot{\epsilon}_m$. As in the original KS analysis, the length-to-thickness ratio of the reinforcing lamellae cannot be too small since load transfer to the lamellae by way of tensile stresses across their ends is assumed to be negligible.

B. Discontinuous lamellae oriented perpendicular to the uniaxial stress

In a composite where the reinforcing lamellae are oriented perpendicular to the applied stress (Figure 5b), the composite creep rate derives from the isostress condition. This condition gives a composite strain rate of:

$$\dot{\epsilon}_c = \dot{\epsilon}_r V_r + \dot{\epsilon}_m V_m. \quad (19)$$

C. Discontinuous lamellae randomly oriented with respect to the uniaxial stress

Since the two cases described in the previous two sections represent the upper and lower bounds of the composite creep strength, a composite possessing randomly

oriented plates should exhibit a value of strength somewhere between these two limiting cases. McLean [25] has developed an analytical expression describing composite creep for the general case of fiber orientation, but only elastically deforming fibers are considered. In this section, we show that the upper and lower bound stresses are similar for the particular case of the TiAl/Ti₃Al lamellar alloy, which obviates the need to find a solution for the general case.

The fiducial line results show that TiAl creeps more rapidly than Ti₃Al in the lamellar alloy. It is therefore appropriate to designate TiAl as the matrix phase and Ti₃Al as the reinforcing phase. The various geometric parameters required for the modified KS model were determined metallographically from samples of the lamellar alloy. The length of the Ti₃Al reinforcing plates was assumed to be equivalent to the average lamellar packet diameter of 70 μm . The average true thickness and volume fraction of the Ti₃Al reinforcing lamellae were measured to be 1.8 μm and 0.36 μm respectively [4]. The quantities $\dot{\epsilon}_m$ and $\dot{\epsilon}_r$ in Eq. 18 and 19 are the strain rates of the TiAl and Ti₃Al phases within the lamellar microstructure, equivalent to $\dot{\epsilon}_\gamma[\text{lamellar}]$ and $\dot{\epsilon}_{\alpha_2}[\text{lamellar}]$ in Eq. 1. The experimentally determined hardening factors can be used to relate $\dot{\epsilon}_\gamma[\text{lamellar}]$ and $\dot{\epsilon}_{\alpha_2}[\text{lamellar}]$ to $\dot{\epsilon}_\gamma[\text{single-phase}]$ and $\dot{\epsilon}_{\alpha_2}[\text{single-phase}]$. The stress and temperature dependence of $\dot{\epsilon}_\gamma[\text{single-phase}]$ and $\dot{\epsilon}_{\alpha_2}[\text{single-phase}]$ have been reported by Oikawa [15] and BYW [4], respectively. In addition, expressions for the parameters $\dot{\epsilon}_{m0}$ and σ_{m0} in Eq. 18 can be found by recasting the power-law constitutive equation for the matrix phase (TiAl), including the appropriate hardening factor.

Based on experimentally determined parameters, the constitutive equations for creep of the composite microstructure (Eq. 18 and 19) can be evaluated. Figure 8 is a graph of composite creep rate versus composite strength for the two cases. This graph demonstrates that there is not more than a 30% difference between the upper and lower bound composite creep strengths, in agreement with the results of the fiducial line experiment discussed in Section IV. The modest difference in strength, for a fixed creep rate, between the matrix and reinforcing phases reflects a small difference in the upper and lower bounds of the composite strength. This would not necessarily be the case for typical metal matrix and polymer matrix composites where the strength of the reinforcing phase is usually significantly greater than that of the matrix phase [25, 26]. Given the small difference in upper and lower bound strengths for the TiAl/Ti₃Al case, it is a reasonable approximation to take the average of these two values as

representative of the strength of the TiAl/Ti₃Al lamellar composite possessing packets of plates aligned randomly with respect to the stress axis.

VI. Model Results

The enhanced hardening factors ($\chi_{\alpha 2}$ and χ_{γ}) described in Section IV of this paper were experimentally determined for each constituent phase from creep tests conducted at 1080 K under an average applied stress of 380 MPa. The value of this factor for each phase is assumed to be constant for creep tests conducted at moderately different stresses and temperatures. The predictions of the modified KS model, with the enhanced hardening of the constituent phases accounted for, are plotted in Figure 9; also included are the experimentally determined creep rates for single-phase TiAl and Ti₃Al and the lamellar alloy [4, 15].

VII. Discussion of Model Results

At 980 K, 1030 K and 1080 K, the agreement between the model predictions and the experimentally determined creep rates for the lamellar alloy is very good. At the highest test temperature, 1130 K, the predicted creep rates of the lamellar alloy are a little lower than the experimentally determined creep rates. This comparison demonstrates that the creep behavior of the lamellar alloy can be represented by a constitutive equation based on composite strengthening mechanisms. The applicability of composite strengthening concepts was not initially apparent because the enhanced hardening of the constituent phases is not present when they are tested as single-phase alloys.

The observation that a single value of the hardening factor for each phase adequately explains the observed behavior over moderate temperature and stress ranges suggests that the mechanisms responsible for enhanced hardening in the lamellar alloy are relatively insensitive to the conditions of the creep test. At 1130 K, the model predicts that the creep rates of the lamellar alloy are approximately a factor of two lower than the experimentally determined rates. Fiducial line experiments could be conducted for lamellar samples crept at 1130 K to determine if the hardening factors are indeed lower at this temperature. If the hardening factors are lower at 1130 K, it would not be immediately apparent whether this is due to a lower work hardening rate or to a higher recovery rate. In this context, it is important to consider that the

hardening factors reflect both the work hardening and recovery phenomena. As discussed previously, the work hardening effect in the lamellar alloy can be attributed to an increase in dislocation source density at the interphase interface, and to considerations of interstitial impurity segregation. It is reasonable to consider that the effect of the interfaces on dislocation generation is less temperature dependent than recovery processes. Therefore, a decrease in the hardening factors at 1130 K most likely reflects an increase in the recovery rate of the constituent phases in the lamellar alloy.

In addition to effects of the recovery rate on the hardening factors, several other effects could contribute to the discrepancy between the model and the experimental results at 1130 K. For example, thermal effects at the interface may be sufficient to promote interfacial sliding at 1130 K. The resulting inefficiency of stress transfer to the reinforcing phase would result in a higher creep rate of the composite.

Rao and Tangri [10] reported that the work hardening rate of two-phase TiAl/Ti₃Al lamellar alloys was greater than the work hardening rates of single-phase TiAl and Ti₃Al. Evaluation of their data revealed that the work hardening rate of the lamellar alloy was approximately an order of magnitude greater than those of the constituent phases. This result is in excellent agreement with the hardening factor values determined from the fiducial line experiments in the present investigation, even though the stoichiometry of the TiAl alloy tested by Rao and Tangri was different from that of the TiAl alloy used in the present investigation. Additionally, Rao and Tangri conducted constant strain rate tests, as opposed to the constant stress creep tests of the current investigation. These differences do not detract from the agreement in experimental results between the two investigations.

In the present study, the difference in creep response of TiAl and Ti₃Al tested as single-phase alloys and tested in the lamellar microstructure was only quantified in terms of the strain hardening factor. Any differences in activation energy for creep and stress exponent between the constituent phases in the lamellar microstructure and the corresponding single-phase alloys were not taken into account. It was assumed that the values of these parameters were not significantly affected by the lamellar phase morphology. This assumption appears justified when comparing the predicted and experimentally determined creep curves represented in Figure 9.

VIII. Conclusions

- (1) During creep deformation of the two-phase TiAl/Ti₃Al lamellar alloy investigated in this study, the TiAl phase within the lamellar microstructure was observed to creep at a higher rate than the Ti₃Al phase within the lamellar microstructure.
- (2) For true strains up to 0.08 at 1080 K, interfacial sliding was undetectable in the lamellar alloy crept in compression.
- (3) The creep rates of the constituent TiAl and Ti₃Al phases within the lamellar microstructure tested in compression are approximately a factor of twenty lower than the creep rates of single-phase TiAl and Ti₃Al tested in compression at the same stress and temperature. This difference can be incorporated into the constitutive equations for the phases in the lamellar microstructure by means of the experimentally determined hardening factors.
- (4) Using constant hardening factors for the constituent phases within the lamellar microstructure, the creep rate of the lamellar alloy can be represented by a constitutive equation based on composite creep strengthening mechanisms. Application of the constitutive equation yields a very good correlation between predicted and experimentally observed minimum creep rates over moderate temperature and stress ranges.

Acknowledgments

We would like to express our gratitude to Mr. D. Gundel for his assistance with the vacuum hot press and Ms. F. Smith, Prof. T. Kozmac and Prof. T. Courtney for their thoughtful and insightful discussions. This work was sponsored by AOFSR under contract number AOFSR-90-0143; Dr. A. Rosenstein was the contract monitor.

References

1. Y.W. Kim and D.M. Dimiduk: *JOM*, 1991, vol. 43, no. 8, pp. 40-7.
2. H.A. Lipsitt, D. Shechtman and R.E. Schafrik: *Metall. Trans. A*, 1980, vol. 11A, pp. 1369-75.
3. S. Mitao, S. Tsuyama and K. Minakawa: *Mater. Sci. Eng.*, 1991, vol. 143A, pp. 51-62.
4. M.F. Bartholomeusz, Q. Yang and J.A. Wert: *Scripta Metall. Mater.*, 1993, vol. 29, pp. 389-94.
5. R.S. Polvani, W.-S. Tzeng and P.R. Strutt: *Metall. Trans. A*, 1976, vol 7A, pp. 33-40.
6. P.R. Strutt and B.H. Kear, in *High-Temperature Ordered Intermetallic Alloys*, C.C. Koch, C.T. Liu and N.S. Stoloff (eds.), MRS, Pittsburgh, PA, 1985, pp. 279-92.
 J.V. Nathal, J.O. Diaz and R.V. Miner, in *High-Temperature Ordered Intermetallic Alloys III*, C.T. Liu, A.I. Taub, N.S. Stoloff and C.C. Koch (eds.), MRS, Pittsburgh, PA, 1985, pp. 269-74.
8. D. McLean: *Progress in Physics*, 1966, vol. 29, pp.1-33.
9. J.P. Poirier: *Creep of Crystals*, Cambridge University Press, Cambridge, 1985, pp. 103-108.
10. P.P. Rao and Kris Tangri: *Mater. Sci. Eng.*, 1991, vol. 132A, pp. 49-59.
11. F. Appel, P.A. Beaven and R. Wagner: *Acta Metall. Mater.*, 1993, vol. 41, pp. 1721-1732.
12. V.K. Vasudevan, M.A. Stucke, S.A. Court and H.L. Fraser: *Philos. Mag. Lett.*, 1989, vol. 59, pp. 299-307.
13. S.A. Court, J.P.A. Lofvander, M.H. Loretto and H.L. Fraser: *Philos. Mag.*, 1990, vol. 61, pp. 109-39.
14. J. Weertman: *Trans. A.S.M.*, 1968, vol. 61, pp. 681-94.
15. H. Oikawa, in *High Temperature Aluminides & Intermetallics*, S.H. Wang, C.T. Liu, D.P. Pope and J.O. Stiegler (eds.), TMS, Warrendale, PA, 1989, pp. 353-73.
16. T. Takahashi, H. Nagai and H. Oikawa: *Mater. Sci. Eng.*, 1990, vol. 128A, pp. 195-200.
17. M.F. Bartholomeusz and J.A. Wert, "Measurement of the Compressive Strain Rates of the Individual Phases within a Lamellar Microstructure", submitted to *Materials Characterization*, 1993.
18. M.G. Mendiratta and H.A. Lipsitt: *J. Mater. Sci.*, 1980, vol. 15, pp. 2985-90.
19. H. Nagai, T. Takahashi and H. Oikawa: *J. Mater. Sci.*, 1990, vol. 25, pp. 629-32.
20. S.C. Huang and D.S. Shih, in *Microstructure/Property Relationships in Titanium*

Aluminides and Alloys Y.W Kim and R.R. Boyer (eds.), TMS, Warrendale, PA, 1990, pp. 105-22.

21. A. Kelly and K.N. Street: *Proc. Roy. Soc. Lond.*, 1972, vol. 328A, pp. 283-93.
22. A. Kelly and W.R. Tyson: *J. Mech. Phys. Solids*, 1966, vol. 14, pp. 177-186.
23. I. Miura and H. Honma: *J. Jap. Inst. Met.*, 1967, vol. 31, pp. 607-610.
24. A. Kelly and K.N. Street: *Proc. Roy. Soc. Lond.*, 1972, vol. 328A, pp. 267-82.
25. M. McLean, in *Proc. 5th Int. Conf. on Composite Materials*, W.C. Harrigan, J. Strife and A.K. Dhingra (eds.), TMS, Warrendale, PA, 1985, pp. 37-51.
26. A.F. Johnson: *Mech. Phys. Solids*, 1977, vol. 25, pp. 117-126.

Table I

Results of fiducial line analysis for the two-phase TiAl/Ti₃Al lamellar alloy compression creep tested at 1080 K under an applied stress of 380 MPa.

lamellar packet #	$\Delta\bar{\theta}_{\text{TiAl}}$	$\Delta\bar{\theta}_{\text{Ti}_3\text{Al}}$	ψ	$\bar{\epsilon}_{\text{TiAl}}$	$\bar{\epsilon}_{\text{Ti}_3\text{Al}}$	$\bar{\epsilon}_{\text{lamellar}}$
1	5.2° (± 1.5°)	2.0° (± 1.1°)	0°	0.091 (± 0.016)	0.034 (± 0.011)	0.071 (± 0.019)
2	1.7° (± 0.5°)	0.7° (± 0.5°)	30°	0.095 (± 0.016)	0.041 (± 0.016)	0.077 (± 0.023)
3	-4.6° (± 1.5°)	-2.7° (± 1.5°)	60°	0.100 (± 0.019)	0.058 (± 0.012)	0.085 (± 0.023)

Table II

Creep rates of lamellar alloy and constituent phases determined from compression creep tests and fiducial line experiments at 1080 K under an applied stress of 380 MPa.

Material	$\dot{\epsilon}$ [creep tests] (1/s)	$\dot{\epsilon}$ [fiducial line results] (1/s)
lamellar alloy	1.8×10^{-6}	$2.1(\pm 0.3) \times 10^{-6}$
TiAl*	6.2×10^{-6}	$2.6(\pm 0.2) \times 10^{-6}$
TiAl*	2×10^{-6}	$1.2(\pm 0.2) \times 10^{-6}$

* Creep data for fine-grain TiAl obtained from Ref. [15]. Creep data for Ti₃Al and lamellar alloy obtained from Ref. [4].

List of Figures

Figure 1. Optical micrograph of undeformed lamellar microstructure. The dark lamellae are the TiAl phase and the light lamellae are the Ti₃Al phase.

Figure 2. Minimum creep rates as a function of stress for the lamellar alloy and the constituent single phase alloys tested at 1080 K by BYW [4] and Oikawa [15].

Figure 3. SEM micrographs of fiducial lines on a surface of the lamellar alloy. (a) Prior to compression creep testing. (b) After compression creep testing at 1080 K under an applied compressive stress of 350 MPa to a true strain of 0.044. The darker phase is the TiAl phase. Its mottled appearance is an artifact of the etching process.

Figure 4. (a) SEM micrographs of fiducial lines on a surface of the lamellar alloy prior to compression creep testing. (b) Region "a" in micrograph (a) after compression creep testing at 1080 K under an applied compressive stress of 380 MPa to a true strain of 0.079. The arrows indicate the compression axis. The heavy dark line represents the orientation of the fiducial line prior to compression creep testing.

Figure 5. (a) represents the velocity of the different phases and the interface in the case where the plates are aligned parallel to the applied stress (z axis). (b) represents the velocity of the different phases when the plates are aligned perpendicular to the applied stress.

Figure 6. Creep rate of a reinforcing lamellar plate as a function of position on the plate. The plate is being viewed edge on.

Figure 7. For a small increment in the length of a reinforcing lamella, δz , the increase in plate stress, $\delta\sigma_r$, is obtained by the force balance: $w\delta\sigma_r = 2\tau w\delta z + 2\tau\delta z$.

Figure 8. Model results of minimum creep rate as a function of stress at 1080 K when the reinforcing lamellae are aligned perpendicular and parallel to the applied stress.

Figure 9. Model predictions compared with the experimentally determined compressive creep rates for the lamellar alloy [4] and the two constituent single phase alloys, TiAl [15] and Ti₃Al [4] at: (a) 980 K. (b) 1030 K. (c) 1080 K. (d) 1130 K.

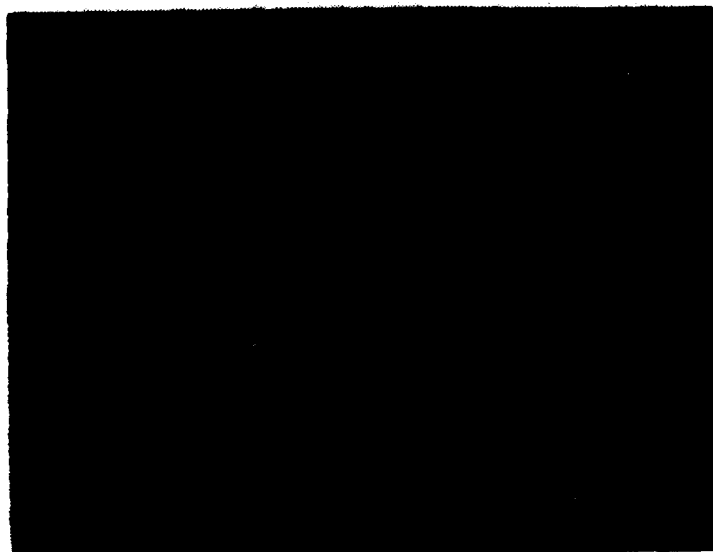


Figure 1. Optical micrograph of undeformed lamellar microstructure. The dark lamellae are the TiAl phase and the light lamellae are the Ti₃Al phase.

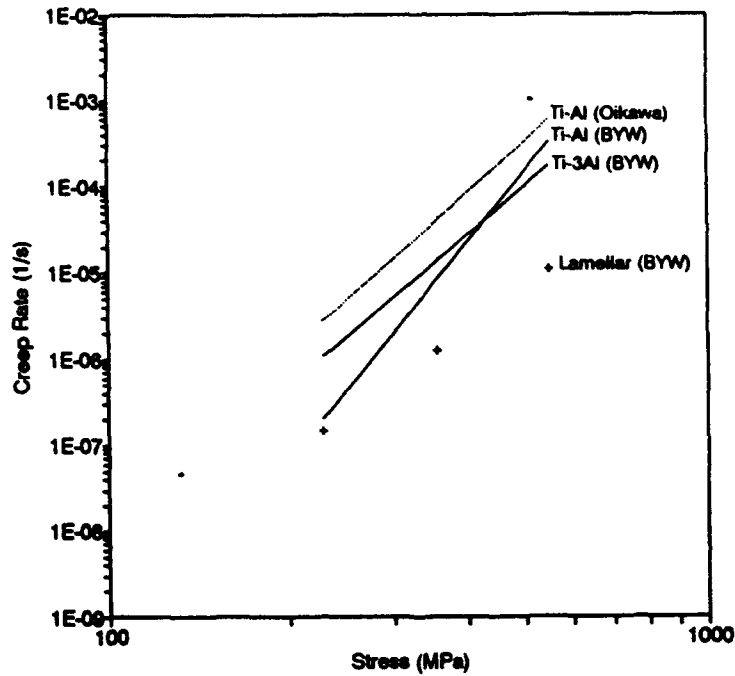
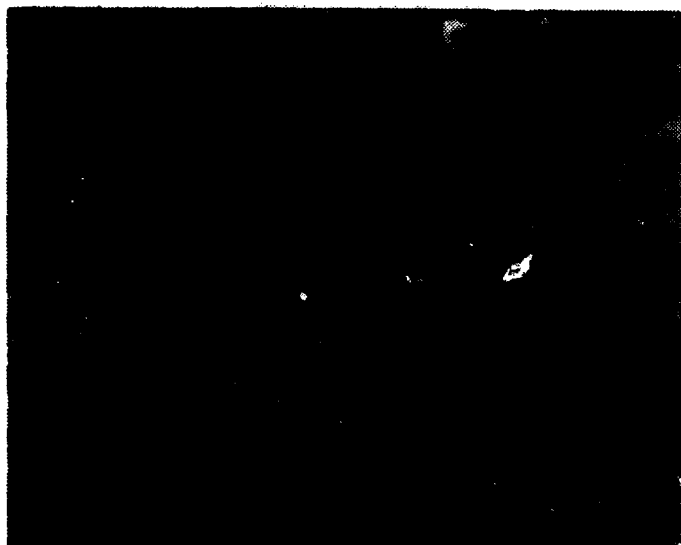
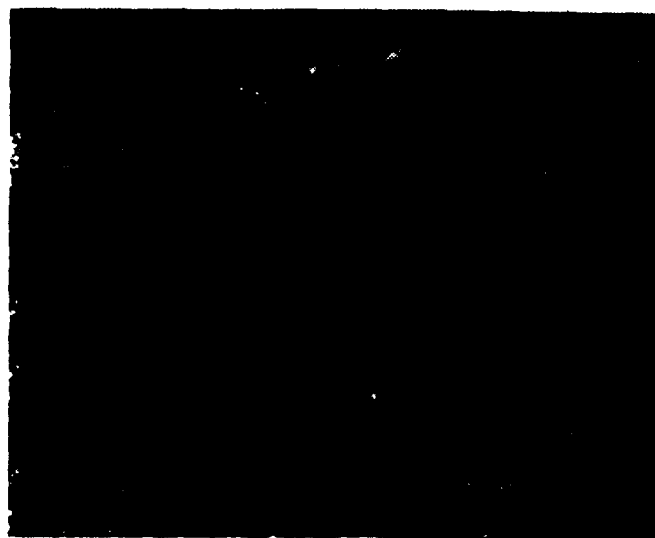


Figure 2. Minimum creep rates as a function of stress for the lamellar alloy and the constituent single phase alloys tested at 1080 K by BYW [4] and Oikawa [14].

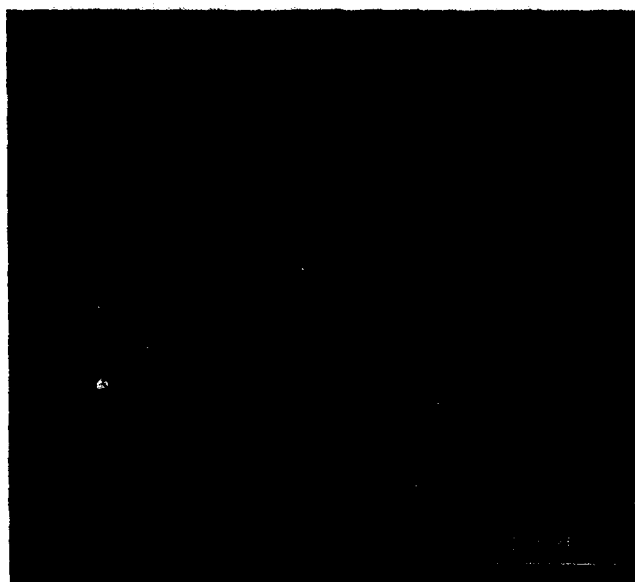


(a)

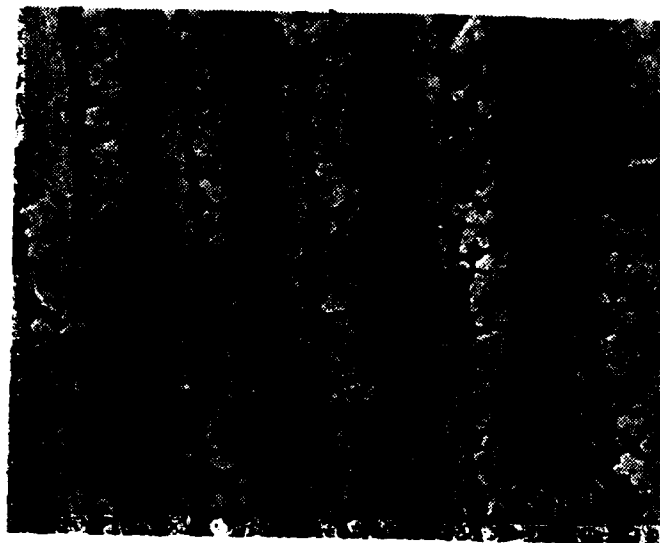


(b)

Figure 3. SEM micrographs of fiducial lines on a surface of the lamellar alloy. (a) Prior to compression creep testing. (b) After compression creep testing at 1080 K under an applied compressive stress of 350 MPa to a true strain of 0.044. The darker phase is the TiAl phase. Its mottled appearance is an artifact of the etching process.

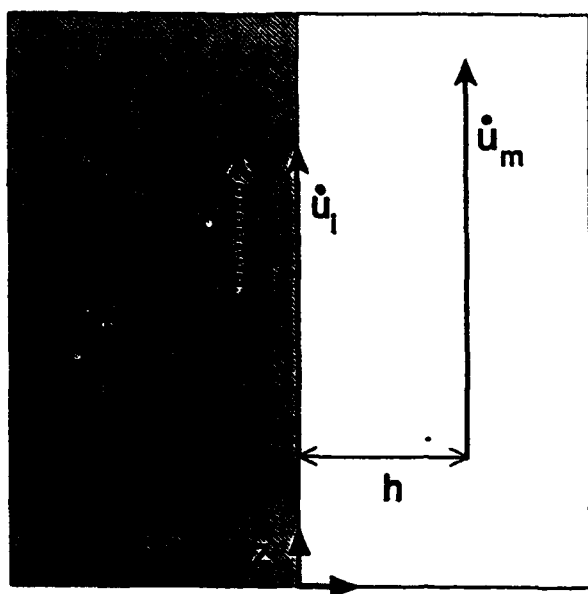


(a)

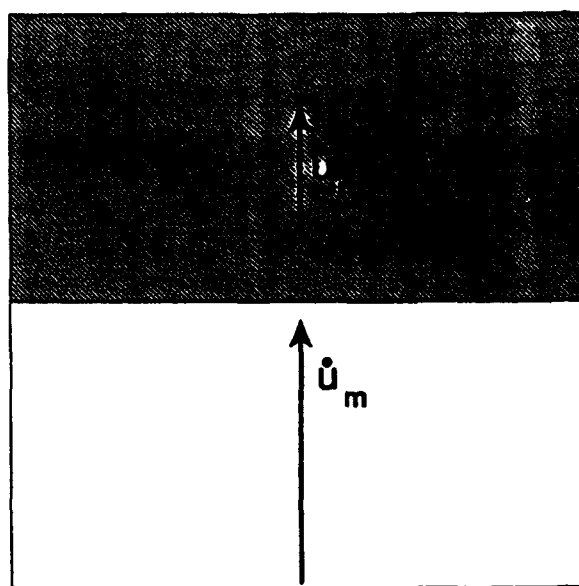


(b)

Figure 4. (a) SEM micrographs of fiducial lines on a surface of the lamellar alloy prior to compression creep testing. (b) Region "a" in micrograph (a) after compression creep testing at 1080 K under an applied compressive stress of 380 MPa to a true strain of 0.079. The arrows indicate the compression axis. The heavy dark line represents the orientation of the fiducial line prior to compression creep testing.



(a)



(b)

Figure 5. (a) represents the velocity of the different phases and the interface in the case where the plates are aligned parallel to the applied stress (z axis). (b) represents the velocity of the different phases when the plates are aligned perpendicular to the applied stress.

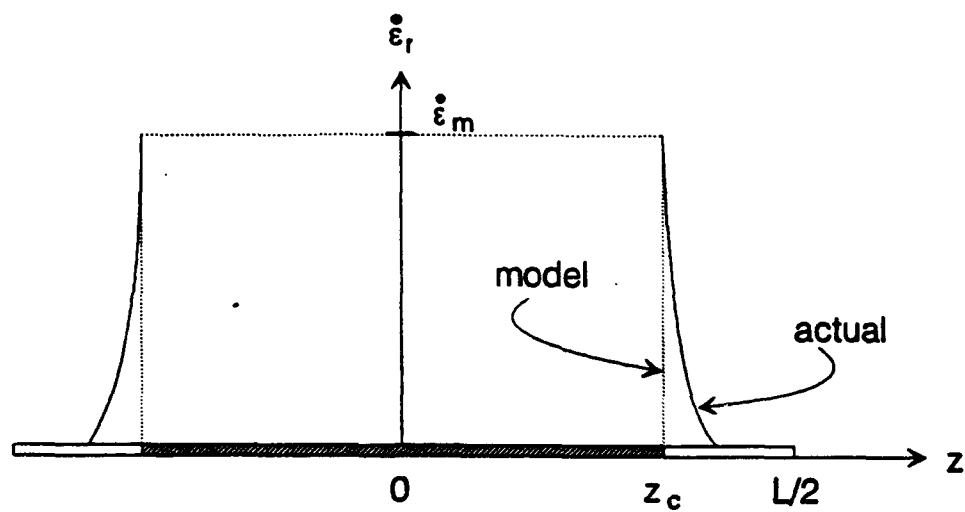


Figure 6. Creep rate of a reinforcing lamellar plate as a function of position on the plate. The plate is being viewed edge on.

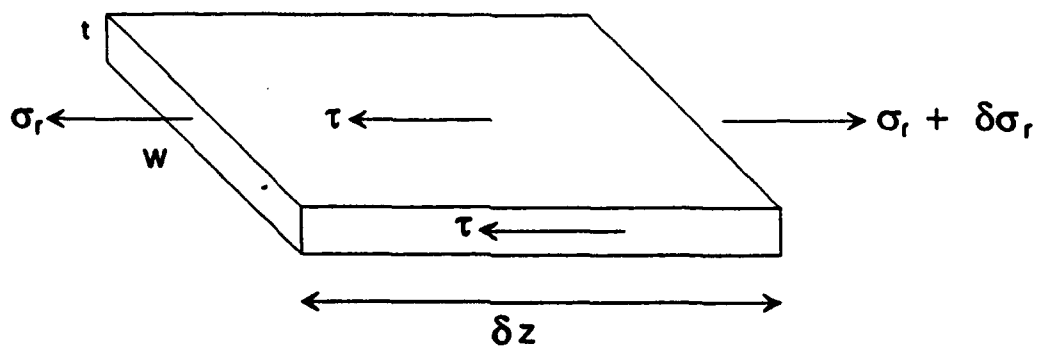


Figure 7. For a small increment in the length of a reinforcing lamella, δz , the increase in plate stress, $\delta\sigma_r$, is obtained by the force balance: $w\delta\sigma_r = 2\tau w\delta z + 2\tau\delta z$.

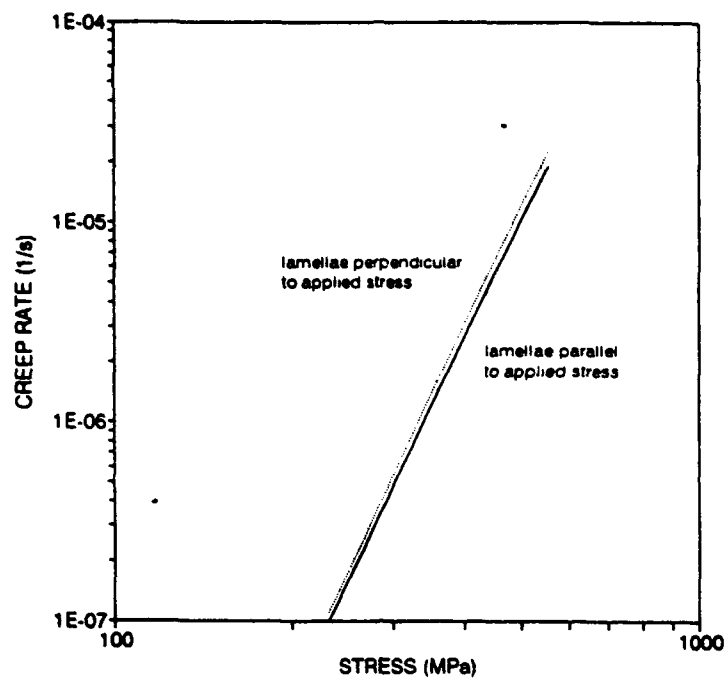
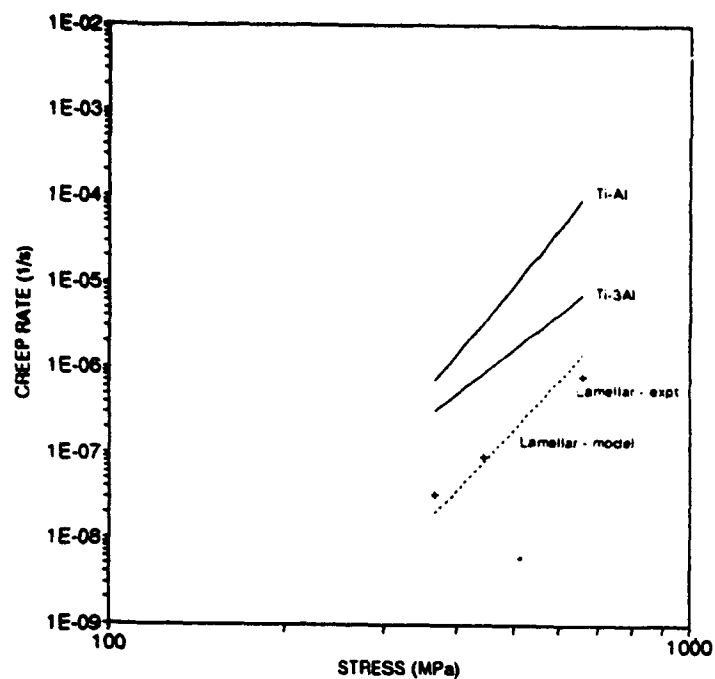
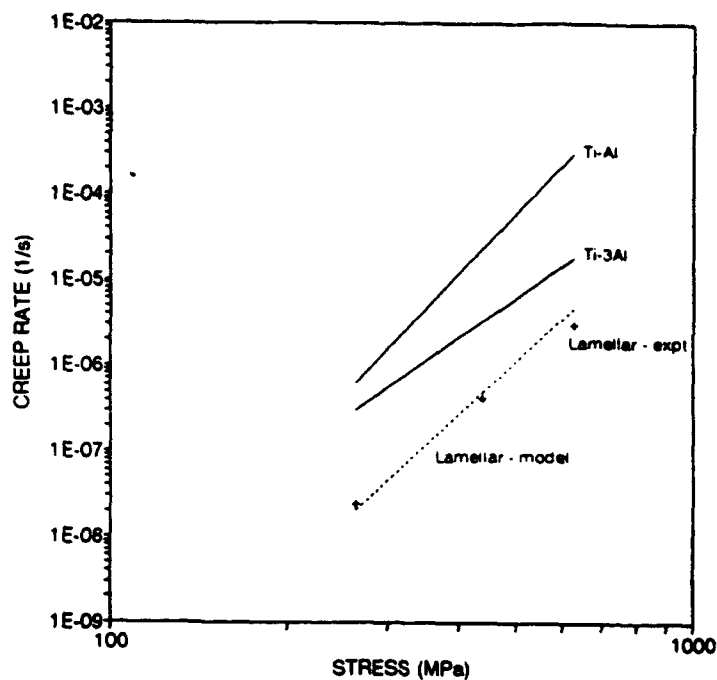


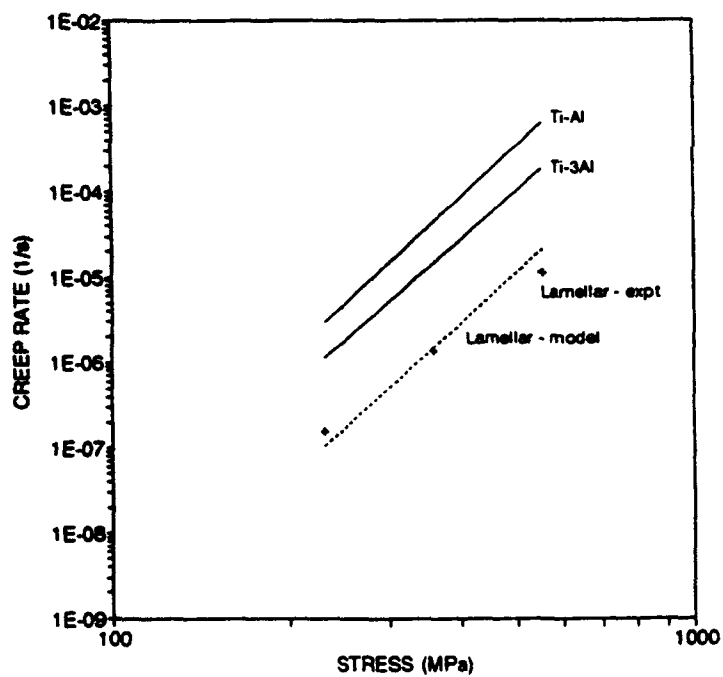
Figure 8. Model results of minimum creep rate as a function of stress at 1080 K when the reinforcing lamellae are aligned perpendicular and parallel to the applied stress.



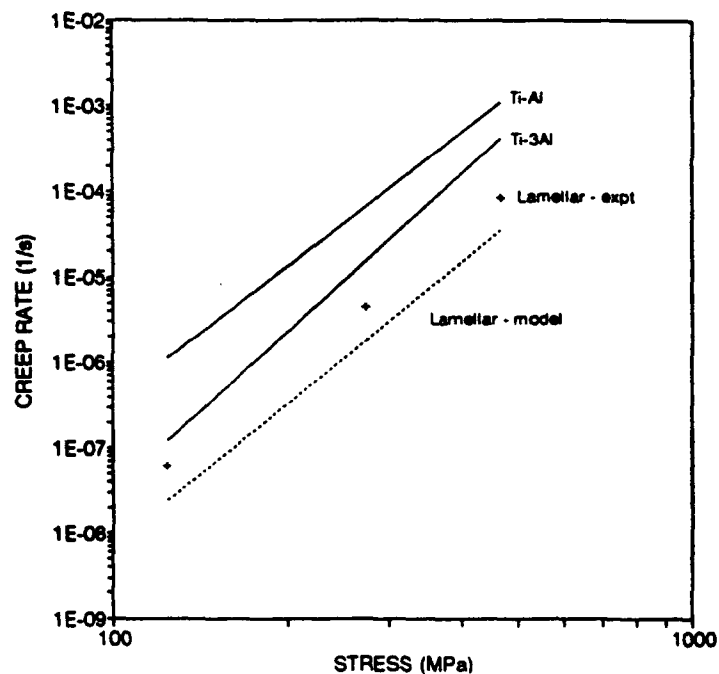
(a)



(b)



(c)



(d)

Figure 9. Model predictions compared with the experimentally determined compressive creep rates for the lamellar alloy [4] and the two constituent single phase alloys, TiAl [14] and Ti_3Al [4] at: (a) 980 K. (b) 1030 K. (c) 1080 K. (d) 1130 K.

Chapter IV

MODELING THE MINIMUM CREEP RATE OF DISCONTINUOUS LAMELLAR-REINFORCED COMPOSITES

I. Introduction

Several analytical and finite element creep models have been developed for fiber and particulate-reinforced composite systems [1-10]. The majority of these models are applicable to composite systems in which the reinforcing phase is non-deforming (rigid) or only elastically deforming at the stress and temperature evaluated. The models have been used to evaluate the effects of reinforcing phase aspect ratio [1-3], fiber alignment with respect to the applied stress [4,5], interfacial sliding [6,7], particle and fiber distribution [8,9], fiber fracture [10], and matrix stress exponent on composite creep rate [6]. In addition, Kelly and Street [7] and Bartholomeusz and Wert [11] have developed composite strength models for the case of discontinuous uniaxially aligned fiber-reinforced and lamellar-reinforced composites, respectively, in which both the matrix and reinforcing phases plastically deform during creep.

The motivation for modeling the creep rate of lamellar composites was provided by recent interest in a two-phase TiAl/Ti₃Al lamellar in-situ composite [12]. Ordered intermetallic alloys based on TiAl and Ti₃Al are a factor of two less dense than nickel-base superalloys and possess many similar mechanical properties [13]. These characteristics make TiAl and Ti₃Al attractive candidates to replace nickel-base superalloys for turbine engine components. However, single-phase TiAl and Ti₃Al alloys exhibit limited ductility at low and intermediate temperatures and are susceptible to rapid fatigue crack growth [12]. It has recently been reported that two-phase TiAl/Ti₃Al in-situ composites have appreciably improved toughness and fatigue resistance compared to the constituent single-phase TiAl and Ti₃Al alloys [12,14]. Furthermore, in contrast to composite strength models which predict that the creep rate of a two-phase composite material is a weighted average of the creep rates of the constituent single phases, Bartholomeusz and coworkers [11,15] demonstrated that a two-phase TiAl/Ti₃Al in-situ composite exhibits a minimum creep rate more than an order of magnitude lower than the minimum creep rates of single-phase TiAl and Ti₃Al alloys, at the same stress and temperature. This result has been shown to arise from the difference in creep properties of the TiAl and Ti₃Al phases within the lamellar

microstructure, compared to the creep properties of single-phase alloys with the same compositions[11,16]. Therefore, in attempting to model the creep response of the two-phase TiAl/Ti₃Al lamellar composite, the effect of the composite microstructure on the creep properties of the constituent phases must be taken into account.

Bartholomeusz and Wert [11] have formulated a constitutive model to predict the creep rate of the two-phase TiAl/Ti₃Al lamellar composite from the creep properties of the constituent phases. Experimental measurements demonstrated that the creep properties of the phases within the TiAl/Ti₃Al lamellar microstructure can be described by introducing hardening factors, approximately equal to 20, into the constitutive equations for power-law creep of the single-phase TiAl and Ti₃Al alloys [11,16]. Model development assumes that no interfacial sliding occurs during creep deformation, consistent with experimental observations for the TiAl/Ti₃Al lamellar composite. Application of the model using the modified constitutive equations for the TiAl and Ti₃Al constituent phases yields excellent correlation between model predictions and experimentally measured minimum creep rates of the TiAl/Ti₃Al lamellar composite over broad stress and temperature ranges [11].

The analytical constitutive model for creep of discontinuous lamellar composites has been previously used to predict the minimum creep rate of a specific composite material. In the present paper, the constitutive model is extended to evaluate the effects of the creep properties of the individual phases and lamellar alignment with respect to the uniaxial stress axis on the composite creep rate. Furthermore, the relative creep rates of discontinuous lamellar-reinforced and fiber-reinforced composites are compared for various cases. The numerical assessments of the model will be based on the material properties of the TiAl and Ti₃Al phases, modified to reflect the additional hardening they experience within the microstructure of the TiAl/Ti₃Al lamellar composite.

II. Model

A model has been previously developed by Bartholomeusz and Wert [11] to predict the creep rate of aligned discontinuous lamellar composites. Two cases were evaluated: lamellae aligned parallel and perpendicular to a uniaxial applied stress. The concept of a continuous matrix phase may not be applicable in the case of an in-situ composite with approximately equal volume fractions of the two phases; however, for

model development, it is convenient to refer to the less creep resistant phase as *the matrix phase*.

The analysis for lamellae aligned parallel to the applied stress is similar to the Kelly and Street [7] shear lag analysis for creep of uniaxially aligned discontinuous fiber reinforced composites. The basic premise of the shear lag models is that bonding at the matrix/reinforcement interface results in retardation of creep in the matrix phase adjacent to the interphase interface. The lower creep rate of the matrix adjacent to the interface produces a shear stress across the interface, resulting in load transfer from the matrix to the reinforcements. The general constitutive relationship for the strength of a uniaxially-aligned discontinuous lamellar composite is [11]:

$$\sigma = \sigma_{mo} \left(\frac{\dot{\epsilon}_c}{\dot{\epsilon}_{mo}} \right)^{1/n} \frac{2t}{L} \left(1 + \frac{t}{L} \right) \left[\lambda 2^{1/n} \left(\frac{L'}{t} \right)^{(2n+1)/n} + 2\beta' \frac{n}{n+1} \left(\frac{L'}{t} \right)^{(n+1)/n} \left(\frac{L}{2t} - \frac{L'}{t} \right) \right] V_r + \sigma_{mo} \left(\frac{\dot{\epsilon}_c}{\dot{\epsilon}_{mo}} \right)^{1/n} (1 - V_r) \quad (1)$$

where

$$\lambda = \left(\frac{2}{3} \right)^{1/n} \frac{n}{2n+1} \left(\frac{V_r}{1-V_r} \right)^{1/n}$$

$$\frac{L'}{2} = \frac{L}{2t} - \frac{z_c}{t}$$

$$z_c = \frac{L}{2} - t \left(\frac{(\dot{\epsilon}_c)^{(1/n-1/n)}}{2\beta'} \frac{n+1}{n} \frac{\sigma_{ro}}{\sigma_{mo}} \frac{(\dot{\epsilon}_{mo})^{1/n}}{(\dot{\epsilon}_{ro})^{1/n}} \frac{w}{w+t} \right)^{n/(n+1)}$$

and

$$\beta' = \frac{1}{2} \left(\frac{4}{3} \right)^{1/n} \left(\frac{V_r}{1-V_r} \right)^{1/n}.$$

The other parameters in Eq. 1 are defined as:

t = thickness of reinforcing lamellae.

L = length of the reinforcing lamellae.

w = width of the reinforcing lamellae.

V_r = volume fraction of the reinforcing phase.

n = stress exponent of the matrix phase.

η = stress exponent of the reinforcement phase.

σ_{mo} and $\dot{\epsilon}_{mo}$ = temperature dependent parameters characterizing the creep behavior of the matrix phase in the constitutive equation:

$$\dot{\epsilon}_m = \dot{\epsilon}_{mo} \left(\frac{\sigma}{\sigma_{mo}} \right)^n. \quad (2)$$

σ_{ro} and $\dot{\epsilon}_{ro}$ = temperature dependent parameters characterizing the creep behavior of the reinforcing phase in the constitutive equation:

$$\dot{\epsilon}_r = \dot{\epsilon}_{ro} \left(\frac{\sigma}{\sigma_{ro}} \right)^\eta. \quad (3)$$

For an applied stress σ , the composite creep rate, $\dot{\epsilon}_c$, can be numerically determined from Eq. 1.

In a composite where the reinforcing lamellae are oriented perpendicular to the applied stress, the reinforcing phase does not significantly constrain the flow of the matrix phase. In this case, the composite creep rate derives from the isostress condition. This condition gives a composite strain rate equal to the weighted sum of

the creep rates of the separate matrix and reinforcing phases [11]:

$$\dot{\epsilon}_c = \dot{\epsilon}_{r0} \left(\frac{\sigma}{\sigma_{r0}} \right)^n V_r + \dot{\epsilon}_{m0} \left(\frac{\sigma}{\sigma_{m0}} \right)^n (1 - V_r), \quad (4)$$

For a composite containing lamellae aligned at an angle ψ with respect to a uniaxial applied stress, there are four modes of plastic deformation to be considered. In Fig. 1, a uniaxial stress is applied parallel to x_3 in the specimen coordinate system (x_1, x_2, x_3). The x_1', x_2', x_3' coordinate system is associated with the lamellae. For a uniaxial stress, σ , applied along the x_3 axis, the only non-zero stress components in the lamellae coordinate system are:

$$\begin{aligned} \text{(i)} \quad & \sigma_{11}' = \sigma \sin^2 \psi \\ \text{(ii)} \quad & \sigma_{33}' = \sigma \cos^2 \psi \\ \text{(iii)} \quad & \sigma_{13}' = \sigma \sin \psi \cos \psi \\ \text{(iv)} \quad & \sigma_{31}' = \sigma \sin \psi \cos \psi. \end{aligned} \quad (5)$$

In the following paragraphs, the contribution of each stress component in Eq. 5 to the creep rate of the composite will be independently evaluated. The creep rate of a lamellar composite with lamellae aligned at an angle ψ with respect to the applied stress will be obtained by summing the individual creep rate contributions. The following analysis is similar to an analysis presented by McLean [4] for the case of a rigid fiber-reinforced composite.

(i) The stress component σ_{33}' is in the plane of the lamellae. The resulting creep rate component of the composite in this direction can be obtained from Eq. 1 by substituting σ_{33}' for σ and numerically solving for $\dot{\epsilon}_c$. The value of $\dot{\epsilon}_c$ corresponding to $\sigma = \sigma_{33}'$ in Eq. 1 will be defined as $\dot{\epsilon}_{33}'$. To satisfy volume conservation there will be additional creep rate components:

$$\dot{\epsilon}_{11}' = \dot{\epsilon}_{22}' = 0.5 \dot{\epsilon}_{33}'. \quad (6)$$

The contribution of creep parallel to the plane of the lamellae ($\dot{\epsilon}_{33}'$) to the uniaxial

creep rate parallel to x_3 is therefore given by:

$$\dot{\epsilon}_{33}(\psi, i) = \dot{\epsilon}_{33}' \left(\cos^2 \psi - \frac{1}{2} \sin^2 \psi \right). \quad (7)$$

(ii) The stress component σ_{13}' results in shear deformation of the composite parallel to the plane of the lamellae. For an isotropic solid with stress exponent N , the shear creep rate, $\dot{\epsilon}_{ij}$, can be expressed in terms of the normal creep rate, $\dot{\epsilon}_{ii}$ (no sum implied), as [4]:

$$\dot{\epsilon}_{ij} = \frac{3^{(N+1)/2}}{2} \dot{\epsilon}_{ii}. \quad (8)$$

Therefore, the contribution of the shear creep rate parallel to the plane of the lamellae ($\dot{\epsilon}_{13}'$) to the uniaxial creep rate parallel to x_3 is given by:

$$\dot{\epsilon}_{33}(\psi, ii) = \frac{3^{(N+1)/2}}{2} \dot{\epsilon}_{33}' \sin \psi \cos \psi, \quad (9)$$

The value of $\dot{\epsilon}_{33}'$ in Eq. 9 can be determined from Eq. 1 by substituting σ_{13}' for σ and numerically solving for $\dot{\epsilon}_c$. In Eq. 9, N is the volume fraction weighted average of the stress exponents of the matrix and reinforcing phases.

(iii) The stress component σ_{31}' results in shear deformation of the composite perpendicular to the plane of the lamellae. Since the shear stress acts perpendicular to the lamellar interphase interfaces, the reinforcing phase does not retard the flow of the matrix phase and deformation of the phases can be assumed to occur independently [11]. The normal creep rate component of the composite perpendicular to the plane of the lamellae is given by Eq. 4. Therefore, using the relationship between shear creep rate and normal creep rate expressed in Eq. 8, the contribution of the shear creep rate perpendicular to the plane of the lamellae ($\dot{\epsilon}_{31}'$) to the uniaxial

creep rate parallel to x_3 is expressed as:

$$\dot{\epsilon}_{33}(\psi, \text{iii}) = \frac{3^{(N+1)/2}}{2} \left(\dot{\epsilon}_{r0} \left(\frac{\sigma}{\sigma_{r0}} \right)^n V_r + \dot{\epsilon}_{m0} \left(\frac{\sigma}{\sigma_{m0}} \right)^n (1 - V_r) \right) \sin \psi \cos \psi. \quad (10)$$

(iv) The normal stress component σ_{11}' results in composite creep perpendicular to the plane of the lamellae, given by the strain rate component $\dot{\epsilon}_{11}'$. The composite creep rate, $\dot{\epsilon}_{11}'$, is equal to $\dot{\epsilon}_c$ in Eq. 4 for $\sigma = \sigma_{11}'$. Volume conservation dictates that there is also flow parallel to the plane of the lamellae:

$$\dot{\epsilon}_{22}' = \dot{\epsilon}_{33}' = 0.5 \dot{\epsilon}_{11}'. \quad (11)$$

Therefore, the contribution of creep perpendicular to the plane of the lamellae ($\dot{\epsilon}_{11}'$) to the uniaxial creep rate parallel to x_3 is given by

$$\dot{\epsilon}_{33}(\psi, \text{iv}) = \left(\dot{\epsilon}_{r0} \left(\frac{\sigma}{\sigma_{r0}} \right)^n V_r + \dot{\epsilon}_{m0} \left(\frac{\sigma}{\sigma_{m0}} \right)^n (1 - V_r) \right) \left(\sin^2 \psi - \frac{1}{2} \cos^2 \psi \right), \quad (12)$$

The total creep rate of a composite containing lamellae aligned at an angle ψ with respect to the applied stress can be expressed as the sum of the individual contributions:

$$\dot{\epsilon}_{33}(\psi) = \dot{\epsilon}_{33}(\psi, \text{i}) + \dot{\epsilon}_{33}(\psi, \text{ii}) + \dot{\epsilon}_{33}(\psi, \text{iii}) + \dot{\epsilon}_{33}(\psi, \text{iv}) \quad (13)$$

There are no adjustable parameters in the expressions comprising Eq. 13.

Two important assumptions are made in the development of Eq. 13: (1) Each strain rate component is independent of the other strain rate components, except as required for volume conservation. (2) Interphase interfacial sliding does not contribute to the creep deformation of the composite. These assumptions are discussed in detail in the following paragraphs.

- (1) In the derivations of expressions for the individual terms on the right hand side of Eq. 13, the shear and normal stress components were decoupled from the normal and shear strain rate components, respectively. It is possible that simultaneous application of normal and shear stresses, as in the cases for $\psi \neq 0$ and $\psi \neq 90$, could couple normal stress components and shear strain rate components, and vice versa. Interactions between the stress and strain rate components are most important for values of ψ where there is a transition between two deformation regimes [4]. A measure of the error involved in the assumptions used to formulate the model can be obtained by applying the model to a homogeneous isotropic solid. This can be accomplished by equating the creep rates and stress exponents of the matrix and reinforcing phases in all of the equations used in the development of Eq. 13.

For a homogeneous isotropic solid (his), $\dot{\epsilon}_{\psi}/\dot{\epsilon}_{his}$ should equal 1 for all values of ψ . Using the material parameters for TiAl listed in Table I, the maximum deviation of the model predictions of $\dot{\epsilon}_{\psi}/\dot{\epsilon}_{his}$ from 1 is approximately a factor of 3.5, which occurs at the values of ψ where there is a transition between predominantly shear and predominantly normal stress and strain rate regimes ($25^{\circ} < \psi < 35^{\circ}$ and $55^{\circ} < \psi < 65^{\circ}$). This result indicates that in cases where the effect of lamellae orientation on creep rate is appreciably larger than 3.5, the assumption of non-interaction of stress components is reasonable. The effect of lamellae orientation on creep rate increases with increasing disparity between the creep rates of the matrix and reinforcing phases for a particular value of applied stress. In the next section it will be shown that when the ratio of matrix to reinforcing phase creep rates is larger than three orders of magnitude, the errors associated with the model assumptions have only a small effect on $\dot{\epsilon}_{33}(\psi)$ for all values of ψ .

- (2) Bartholomeusz and Wert [16] used a fiducial line analysis to demonstrate that interfacial sliding does not occur in a TiAl/Ti₃Al lamellar in-situ composite creep tested to a true strain of approximately 0.1. This result is consistent with the idea that the strong bonding associated with semi-coherent interphase interfaces resists interfacial sliding. The model developed in the present paper is most applicable for this class of in-situ composites. For lamellar alloys possessing weak interphase interfaces, interfacial sliding is expected to increase the creep rate of the composite. Recent analyses by McMeeking [6] for aligned rigid fiber-reinforced composites

demonstrates that interfacial sliding can result in a dramatic increase in composite creep rate.

III. Results

All model calculations given in the present paper have been performed using the material parameters of the constituent phases within the TiAl/Ti₃Al lamellar composite [11]. The creep properties of the TiAl and Ti₃Al constituent phases in Table I have been modified to reflect the additional hardening they experience in the lamellar microstructure, as discussed in the introduction section. Since the TiAl phase creeps at a faster rate than the Ti₃Al phase for the same applied stress, TiAl is considered to be the matrix phase and Ti₃Al is the reinforcing phase. The values of σ_{mo} and σ_{ro} can be selected so that the difference in creep rates of the constituent phases is entirely represented by $\dot{\epsilon}_{mo}$ and $\dot{\epsilon}_{ro}$. Since the stress exponents of the TiAl and Ti₃Al phases are similar, the same value has been used for σ_{mo} and σ_{ro} .

The constant $\dot{\epsilon}_{ro}$ for Ti₃Al can be varied between $\dot{\epsilon}_{mo}$ and $\dot{\epsilon}_{mo}/10^9$ to reflect composite creep properties ranging from a homogeneous solid to a discontinuous lamellar composite containing a nondeforming reinforcing phase (rigid lamellar-reinforced composite). The factor of 10^9 for the case of a non-deforming reinforcing phase was arrived at by equating Eq. 1 to a corresponding expression for the creep strength of a uniaxially aligned discontinuous rigid lamellar-reinforced composite:

$$\sigma_c = \sigma_{mo} \left(\frac{\dot{\epsilon}}{\dot{\epsilon}_{mo}} \right)^{1/n} \left[\frac{\phi V_r}{2} \left(1 + \frac{t}{L} \right) \left(\frac{L}{t} \right)^{(n+1)/n} + (1 - V_r) \right] \quad (14)$$

where

$$\phi = \left(\frac{2}{3} \right)^{1/n} \left(\frac{n}{2n+1} \right) \left(\frac{V_r}{1 - V_r} \right)^{1/n}.$$

Thus, when the creep rate of the reinforcing phase is nine orders of magnitude less than the creep rate of the matrix phase, the composite strengths given by Eqs. 1 and 14

are equal. The derivation of Eq. 14 is based on a similar derivation by Kelly and Street [7] for the case of uniaxially aligned discontinuous rigid fiber-reinforced composites.

Fig. 2 depicts the effect of reinforcement creep properties (relative to the matrix creep properties) on the anisotropy of composite creep. The abscissa represents the ratio of matrix to reinforcing phase creep rates, $\dot{\epsilon}_{m0}/\dot{\epsilon}_{r0}$. As discussed previously, this ratio spans the range from 1 to 10^9 representing the transition from a homogeneous solid to a rigid lamellar-reinforced composite. The ordinate represents the ratio of the creep rates of composites possessing lamellae aligned perpendicular ($\psi = 90^\circ$) and parallel ($\psi = 0^\circ$) to an applied stress of 380 MPa, $\dot{\epsilon}_{33}(\psi = 90^\circ)/\dot{\epsilon}_{33}(\psi = 0^\circ)$. The constitutive relations for composites possessing lamellae aligned parallel and perpendicular to the applied stress are given by Eq. 1 and 4, respectively. In the present calculations, $\dot{\epsilon}_{33}(\psi = 90^\circ)$ and $\dot{\epsilon}_{33}(\psi = 0^\circ)$ represent the upper and lower bound creep rates of lamellar-reinforced composites [11].

Fig. 2 demonstrates that the effect of lamellae orientation on the creep rate of the TiAl/Ti₃Al lamellar composite dominates the error associated with the assumption of decoupled normal and shear stress and strain rate components for values of $\dot{\epsilon}_{m0}/\dot{\epsilon}_{r0}$ greater than 10^3 . For $\dot{\epsilon}_{m0}/\dot{\epsilon}_{r0} = 10^4$, the largest error in the predicted composite creep rate due to the assumptions of the model is less than 5% of the variation of composite creep rate due to lamellae orientation. For larger values of $\dot{\epsilon}_{m0}/\dot{\epsilon}_{r0}$, the variation of composite creep rate arising from assumptions in the model is only a fraction of a percent of the variation of composite creep rate due to lamellae orientation. Therefore, for values of $\dot{\epsilon}_{m0}/\dot{\epsilon}_{r0}$ larger than about 10^3 , the model developed in the present paper (Eq. 13) can be utilized to determine $\dot{\epsilon}_{33}(\psi)$ as a function of ψ .

For values of $\dot{\epsilon}_{m0}/\dot{\epsilon}_{r0} < 10^3$, there is less than an order of magnitude difference between $\dot{\epsilon}_{33}(\psi = 90^\circ)$ and $\dot{\epsilon}_{33}(\psi = 0^\circ)$, and the error associated with the assumption of decoupled normal and shear stress and strain rate components dominates the effect of lamellae orientation on the creep rate of the TiAl/Ti₃Al lamellar composite. However, due to the small difference between $\dot{\epsilon}_{33}(\psi = 90^\circ)$ and $\dot{\epsilon}_{33}(\psi = 0^\circ)$, $\dot{\epsilon}_{33}(\psi)$ as a function of ψ can be reasonably approximated as a linear function of the creep rates of the composite for ψ equal to 0° and 90° .

Fig. 3 shows the relative composite creep rate of the TiAl/Ti₃Al lamellar composite as a function of ψ for several values of $\dot{\epsilon}_{m0}/\dot{\epsilon}_{r0}$. For the curves representing

$\dot{\epsilon}_{m0}/\dot{\epsilon}_{r0} = 2$ and 10^3 , the relative composite creep rate as a function of ψ is modeled as a linear function of the creep rates of the lamellar composite for ψ equal to 0° and 90° , as discussed in the previous paragraph. The curve for $\dot{\epsilon}_{m0}/\dot{\epsilon}_{r0} = 2$ represents model predictions and the solid squares represent experimentally determined relative minimum creep rates as a function of lamellae orientation for the TiAl/Ti₃Al lamellar composite deformed in compression at an applied stress of 380 MPa [16].

Figs. 4 and 5 illustrate the effects of the microstructural parameters L/t and V_r on the relative creep rate of the composite. In Fig. 4 the smallest value of lamellar aspect ratio considered in the present calculation is 10. For aspect ratios smaller than this, the composite strength model developed in Eq. 1 is inaccurate because the contribution of direct load transfer to lamellae faces normal to the applied stress is neglected in the present model [7,11].

In Fig. 6, the ratio of the creep rate of a uniaxially aligned discontinuous lamellar-reinforced composite to the creep rate of a uniaxially aligned discontinuous fiber-reinforced composite is represented as a function of the ratio of $\dot{\epsilon}_{m0}/\dot{\epsilon}_{r0}$, for several values of reinforcing phase volume fraction. Recall that the ratio $\dot{\epsilon}_{m0}/\dot{\epsilon}_{r0}$ varies between 1 and 10^9 , representing the transition from a homogeneous solid to a rigid reinforcing phase. The constitutive equation for creep of uniaxially aligned discontinuous fiber-reinforced composites is presented in Ref [7], and the constitutive equation for creep of uniaxially aligned discontinuous lamellar-reinforced composites is given by Eq. 1. The same material parameters were used for both composite morphologies. The fiber length and diameter were taken to be equal to the lamellar length and thickness, respectively.

It is important to recognize that numerical results for different composite systems can differ significantly from the results for the TiAl/Ti₃Al lamellar composite as a consequence of the sensitivity of the constitutive equations to the material properties and geometrical characteristics of the matrix and reinforcing phases (i.e., n , η , $\dot{\epsilon}_{m0}$, $\dot{\epsilon}_{r0}$, σ_{m0} , σ_{r0} , t , L , w and V_r). However, the general trends reported in the present paper are characteristic of lamellar composites undergoing power-law creep deformation in the absence of interfacial sliding.

IV. Discussion

A. The effect of lamellae orientation on composite creep rate.

The good agreement between the experimental results (filled squares) and model predictions ($\dot{\epsilon}_{m0}/\dot{\epsilon}_{r0} = 2$) for the TiAl/Ti₃Al lamellar in-situ composite in Fig. 3 validates the linear relationship assumed between $\dot{\epsilon}_{33}(\psi)$ and ψ for small values of $\dot{\epsilon}_{m0}/\dot{\epsilon}_{r0}$. Therefore, for values of $\dot{\epsilon}_{m0}/\dot{\epsilon}_{r0} < 10^3$, the creep rate of a composite containing randomly aligned lamellar packets is computed as the arithmetic mean of lamellae aligned parallel and perpendicular to the applied stress [11]. Alternatively, for values of $\dot{\epsilon}_{m0}/\dot{\epsilon}_{r0} > 10^3$, integration of the curves in Fig. 3 yields the value of relative composite creep rate for a composite comprised of randomly aligned lamellar packets. The model predictions are equally valid for composites containing randomly aligned lamellar packets or randomly aligned lamellae.

The model results in Fig. 3 demonstrate that as the ratio of matrix to reinforcement creep rate, $\dot{\epsilon}_{m0}/\dot{\epsilon}_{r0}$, increases, the relative creep rate of composites possessing lamellae aligned nearly parallel to the applied stress ($\psi < 20^\circ$) decreases significantly, but the relative creep rate of composites with lamellae aligned nearly normal to the applied stress ($\psi > 80^\circ$) decreases only slightly. This result indicates that selection of a reinforcing phase based on its creep properties has a much smaller impact for composites undergoing isostress creep deformation ($\psi \approx 90^\circ$) than for composites undergoing isostrain creep deformation ($\psi \approx 0^\circ$). This result has similar implications for other composite morphologies where isostress loading predominates, i.e., particulate-reinforced composites and fiber-reinforced composite with fiber alignment perpendicular to the applied stress. The model developed in the present paper predicts that the isostress creep rate of a lamellar composite with nondeforming reinforcements is only a factor of 2 slower than the creep rate of the unreinforced matrix phase. This prediction is in agreement with experimental results determined by McLean [4] for a (Co,Cr)(Co,Cr)₇C₃ eutectic composite. The creep rate of the nondeforming fiber reinforced composite undergoing isostress deformation ($\psi \approx 90^\circ$) was only a factor of 4 slower than the creep rate of the unreinforced matrix phase.

B. Effect of reinforcing lamellar aspect ratio on composite creep.

In this section, the effect of the lamellar aspect ratio (L/t) will be evaluated for the case of lamellae aligned parallel to the applied stress. For lamellae aligned perpendicular to the applied stress the present model predicts that composite creep rate is independent of lamellar aspect ratio. This is only the case if the value of lamellar thickness remains large enough so that significant transverse stresses do not develop in the matrix and reinforcing phases. In real lamellar-reinforced composites possessing lamellae aligned perpendicular to the applied stress, there is likely to be a small dependence of composite creep rate on lamellar aspect ratio.

Two curves representing different ratios of matrix to reinforcement creep resistance, $\dot{\epsilon}_m/\dot{\epsilon}_r$, are plotted in Fig. 4. These curves demonstrate that as the ratio $\dot{\epsilon}_m/\dot{\epsilon}_r$ increases, the composite creep rate is more strongly affected by lamellar aspect ratio. In the case of a rigid lamellar composite (not shown in Fig. 4), increasing the lamellar aspect ratio from 30 to 100 decreases the composite creep rate by more than two orders of magnitude. The decrease in composite creep rate with increasing lamellar aspect ratio becomes insignificant for lamellar aspect ratios larger than 70. For small differences between matrix and reinforcement creep rates ($\dot{\epsilon}_m/\dot{\epsilon}_r < 10^2$), composite creep rate is essentially independent of lamella aspect ratio for $L/t > 10$.

The shape of the curves in Fig. 4 indicates the importance of achieving a nearly constant value of lamellar aspect ratio in lamellar composites where $\dot{\epsilon}_m/\dot{\epsilon}_r > 10^3$. If a composite possesses a wide range of lamellar aspect ratios, the overall composite creep rate can be approximated by summing the contributions of lamellae with distinct aspect ratios. Since the curve is concave upward, the sum of the individual contributions will always be greater than the composite creep rate for the mean value of aspect ratio. For example, consider the curve representing $\dot{\epsilon}_m/\dot{\epsilon}_r = 10^5$ in Fig. 4. If half the lamellae in the composite have an aspect ratio of 20 and the other half have an aspect ratio of 60, the mean lamellar aspect ratio is 40. Fig. 4 shows that the composite creep rate for a lamellar aspect ratio of 40 is $0.0019\dot{\epsilon}_m$, whereas, the average composite creep rate for lamellae possessing aspect ratios of 20 and 60 is approximately $0.5 \times (0.0041\dot{\epsilon}_m + 0.0015\dot{\epsilon}_m) = 0.0028\dot{\epsilon}_m$. The composite creep rate obtained using the mean lamellar aspect ratio underestimates the composite creep rate by a factor of 1.5 in this case. This underestimation can exceed a factor of 20 in the case of rigid lamellar composites.

The model results discussed in this section have two broad implications for materials with $\dot{\epsilon}_m/\dot{\epsilon}_r > 10^3$. First, predicting composite creep rate based on a mean value of lamellar aspect ratio can result in gross underestimation. Second, fracture of lamellae during composite fabrication and/or service can have a significant deleterious effect on composite creep resistance.

C. Effect of reinforcing lamella volume fraction on composite creep.

The influence of reinforcing phase volume fraction on the creep rate of composites containing lamellae aligned parallel ($\psi = 0^\circ$) and perpendicular ($\psi = 90^\circ$) to the applied stress for $\dot{\epsilon}_m/\dot{\epsilon}_r = 10^3$ is plotted in Fig. 5. As would be expected, increasing the volume fraction of the reinforcing phase decreases the composite creep rate. For other values of $\dot{\epsilon}_m/\dot{\epsilon}_r$, the composite creep rate as a function of volume fraction has the same form as the curves represented in Fig. 5, with the composite creep rate always varying between the creep rates of the matrix and reinforcing phases.

The positive second derivative of the curve for lamellae aligned parallel to the applied stress in Fig. 5 yields a noteworthy result. The composite creep rate increases as the inhomogeneity of the reinforcing phase distribution increases. Consider the curve representing $\dot{\epsilon}_m/\dot{\epsilon}_r = 10^3$ in Fig. 5 for two composite materials: one possessing an inhomogeneous distribution of reinforcing phase (i.e., half of the microstructure has a reinforcing phase volume fraction of 0.20 and the remainder of the microstructure has a reinforcing phase volume fraction of 0.60), and a second possessing a homogeneous distribution of reinforcing phase (with reinforcing phase volume fraction equal to 0.40). In both cases the mean reinforcing phase volume fraction is 0.40. However, consulting Fig. 5 demonstrates that the composite creep rate of the homogeneous composite material, $0.025\dot{\epsilon}_m$, is more than 2.5 times slower than the approximate creep rate of the inhomogeneous composite material, $0.5 \times (0.12\dot{\epsilon}_m + 0.0076\dot{\epsilon}_m) = 0.064\dot{\epsilon}_m$. This factor can exceed 30 in the case of rigid lamellar reinforced composites ($\dot{\epsilon}_m/\dot{\epsilon}_r = 10^9$). In the case of lamellae aligned perpendicular to the applied stress, Fig. 5 demonstrates that the homogeneity, or lack thereof, of the reinforcing phase distribution in the microstructure has no effect on composite creep rate. This result applies to isostress loading in general.

The previous example considered the effect of microstructural inhomogeneity on the relative composite creep rate at constant stress. Now consider the effect of microstructural inhomogeneity on the stress required to maintain a constant composite creep rate. For $\psi > 0^\circ$, an inhomogeneous reinforcing phase distribution requires a larger flow stress to attain a particular value of creep rate than a homogeneous reinforcing phase distribution with the same mean volume fraction. This result is in agreement with previous results presented by Bao et al. [8] for the case of rigid particles in a plastic matrix. In the case of lamellae aligned parallel to the applied stress ($\psi = 0^\circ$), the homogeneity of the reinforcing phase distribution in the microstructure has no effect on the stress required to attain a particular value of relative composite creep rate.

If design considerations require minimizing the relative composite creep rate for a specified stress, microstructural homogeneity can be used to minimize the creep rate for a prescribed reinforcing phase volume fraction in the case of lamellae aligned parallel to the applied stress, but has no effect in the case of lamellae aligned perpendicular to the applied stress. If, on the other hand, design considerations call for maximizing the flow stress required for a particular value of composite creep rate, then microstructural inhomogeneity can be used to maximize the flow stress for a prescribed reinforcing phase volume fraction in the case of lamellae aligned perpendicular to the applied stress, but has no effect in the case of lamellae aligned parallel to the applied stress.

D. Comparison between creep of aligned discontinuous lamellar and fiber reinforced composites.

Fig. 6 demonstrates that aligned discontinuous fiber-reinforced composites only become appreciably more creep resistant than aligned discontinuous lamellar-reinforced composites when $\dot{\epsilon}_{m0}/\dot{\epsilon}_{r0}$ exceeds about 10^5 . Additionally, as the reinforcing phase volume fraction increases, the ratio of lamellar-reinforced and fiber-reinforced composite creep rates noticeably decreases for large ratios of $\dot{\epsilon}_{m0}/\dot{\epsilon}_{r0}$. These results demonstrate that there is no significant improvement in creep resistance for aligned fiber-reinforced composites compared to aligned lamellar-reinforced composites, unless the reinforcing phase is essentially nondeforming in comparison with the matrix phase.

V. Conclusions

- (1) An analytical model has been developed to predict the creep rate of discontinuous lamellar-reinforced composites in which both phases plastically deform. The model incorporates effects associated with lamellar orientation relative to the uniaxial stress axis.
- (2) For modest to large differences between matrix and reinforcement creep rates, ($\dot{\epsilon}_{mo}/\dot{\epsilon}_{ro} > 10^3$), lamellar aspect ratio has a significant impact on composite creep rate.
- (3) For a prescribed reinforcing phase volume fraction, microstructural inhomogeneity can have a pronounced effect on composite creep properties. In the case of uniaxially aligned rigid lamellar-reinforced composites, an inhomogeneous distribution of reinforcing lamellae in the microstructure substantially increases the composite creep rate.
- (4) Model results demonstrate that there is no significant improvement in creep resistance for aligned fiber-reinforced composites compared to aligned lamellar-reinforced composites, unless the reinforcing phase is essentially nondeforming relative to the matrix phase.

Acknowledgments

This work was sponsored by AOFSR under contract number AOFSR-SR-90-0143; Capt. C. Ward was the contract monitor.

References

1. G. Bao, J.W. Hutchinson and R.M. McMeeking: *Acta Metall. et Mater.*, 1991, vol. 39, pp. 1871-82.
2. M. McLean, in *Proc. 5th Int. Conf. on Composite Materials*, W.C. Harrigan, J. Strife and A.K. Dhingra (eds.), TMS, Warrendale, PA, 1985, vol. 25, pp. 37-51.
3. H. Lilholt: *Materials Forum*, 1988, vol. 11, pp. 133-9.
4. D.E. Miles and M. McLean: *Metals Science*, 1977, vol. 11, pp. 563-70.
5. A.F. Johnson: *Mech. Phys. Solids*, 1977, vol. 25, pp. 117-26.
6. R.M. McMeeking: *Int. J. Solids Structures*, 1993, vol. 30, no. 13, pp. 1807-23.
7. A. Kelly and K.N. Street, *Proc. Roy. Soc. Lond.*, 1972, vol. 328A, pp. 283-93.
8. G. Bao, J.W. Hutchinson and R.M. McMeeking: *Mechanics of Materials*, 1991, vol. 12, pp. 85-94.
9. J.R. Brockenbrough, S. Suresh and H.A. Wienecke: *Acta Metall. et Mater.*, 1991, vol. 39, pp. 735-52.
10. R.M. McMeeking, in *Elevated Temperature Mechanical Behavior of Ceramic Matrix Composites*, S.V. Nair and K. Jakus (eds.), Butterworth-Heinemann, Stoneham, MA, 1992, in press.
11. M.F. Bartholomeusz and J.A. Wert, "Modeling Creep Deformation of a Two-Phase TiAl/Ti₃Al Alloy with a Lamellar Microstructure", submitted to *Metall. Trans. A*, 1994.
12. Y.W. Kim and D.M. Dimiduk: *JOM*, 1991, vol. 43, no. 8, pp. 40-7.
13. Y.W. Kim: *JOM*, 1989, vol. 41, pp. 24-30.
14. S. Mitao, S. Tsuyama and K. Minakawa: *Mater. Sci. Eng.*, 1991, vol. 143A, pp. 51-62.
15. M.F. Bartholomeusz, Q. Yang and J.A. Wert: *Scripta Metall. Mater.*, 1993, vol. 29, pp. 389-94.
16. M.F. Bartholomeusz and J.A. Wert, "Measurement of the Compressive Strain Rates of the Individual Phases within a Lamellar Microstructure", submitted to *Materials Characterization*, 1993.
17. H. Oikawa, in *High Temperature Aluminides & Intermetallics*, S.H. Wang, C.T. Liu, D.P. Pope, and J.O. Stiegler (eds.), TMS, Warrendale, PA, 1989, pp. 353-73.

Table I Material and geometric properties of the TiAl and Ti₃Al constituent phases modified to reflect the additional hardening they undergo within the microstructure of the two-phase TiAl/Ti₃Al lamellar in-situ composite [11,15,17].

TiAl (matrix phase)	Ti ₃ Al (reinforcement phase)
T = 1080 K	T = 1080 K
$\sigma_{m0} = 300 \text{ MPa}$	$\sigma_{r0} = 300 \text{ MPa}$
$\dot{\epsilon}_{m0} = 6.28 \times 10^{-7} \text{ /s}$	$\dot{\epsilon}_{r0} = 3.01 \times 10^{-7} \text{ /s}$
$n = 6.14$	$\eta = 5.82$
	$L = w = 70 \times 10^{-6} \text{ m}$
	$t = 1.8 \times 10^{-6} \text{ m}$
	$V_r = 0.36$

List of Figures

Figure 1. The uniaxial stress, σ , applied along the x_3 axis, is defined in the specimen coordinate system (x_1, x_2, x_3). The x_1', x_2', x_3' coordinate system is associated with the lamellae.

Figure 2. The effect of reinforcement creep properties (relative to the matrix creep properties), $\dot{\epsilon}_m/\dot{\epsilon}_r$, on the anisotropy of composite creep. The ratio $\dot{\epsilon}_m/\dot{\epsilon}_r$ varies from 1 to 10^9 representing the transition from a homogeneous solid to a rigid lamellar reinforced composite.

Figure 3. A series of curves for lamellar composites showing the relative composite creep rate as a function of ψ for several values of $\dot{\epsilon}_m/\dot{\epsilon}_r$. The curve for $\dot{\epsilon}_m/\dot{\epsilon}_r = 2$ represents model predictions and the solid squares represent experimentally determined relative minimum creep rates as a function of lamellae orientation for the TiAl/Ti₃Al lamellar composite deformed in compression at an applied stress of 380 MPa [16].

Figure 4. The effect of lamellar aspect ratio, L/t , on the relative creep rate of the composite for two values of $\dot{\epsilon}_m/\dot{\epsilon}_r$.

Figure 5. The effect of the reinforcing phase volume fraction, V_r , on the relative creep rate of the composite for isostrain ($\psi = 0^\circ$) and isostress ($\psi = 90^\circ$) loading conditions.

Figure 6. The ratio of the creep rate of a uniaxially aligned discontinuous *lamellar*-reinforced composite to the creep rate of a uniaxially aligned discontinuous *fiber*-reinforced composite is represented as a function of $\dot{\epsilon}_m/\dot{\epsilon}_r$, for several values of reinforcing phase volume fraction.

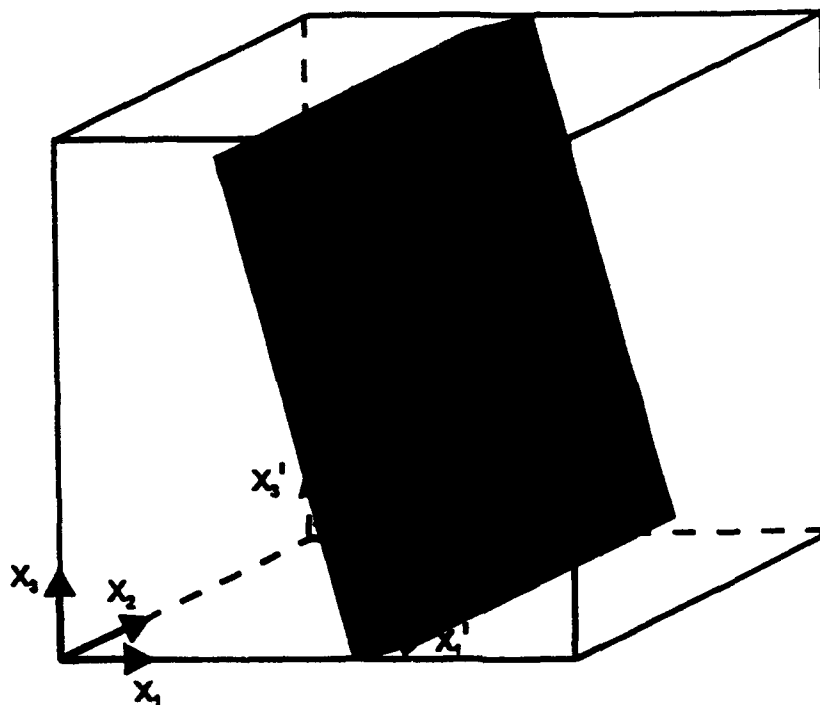


Figure 1. The uniaxial stress, σ , applied along the x_3 axis, is defined in the specimen coordinate system (x_1, x_2, x_3) . The x_1', x_2', x_3' coordinate system is associated with the lamellae.

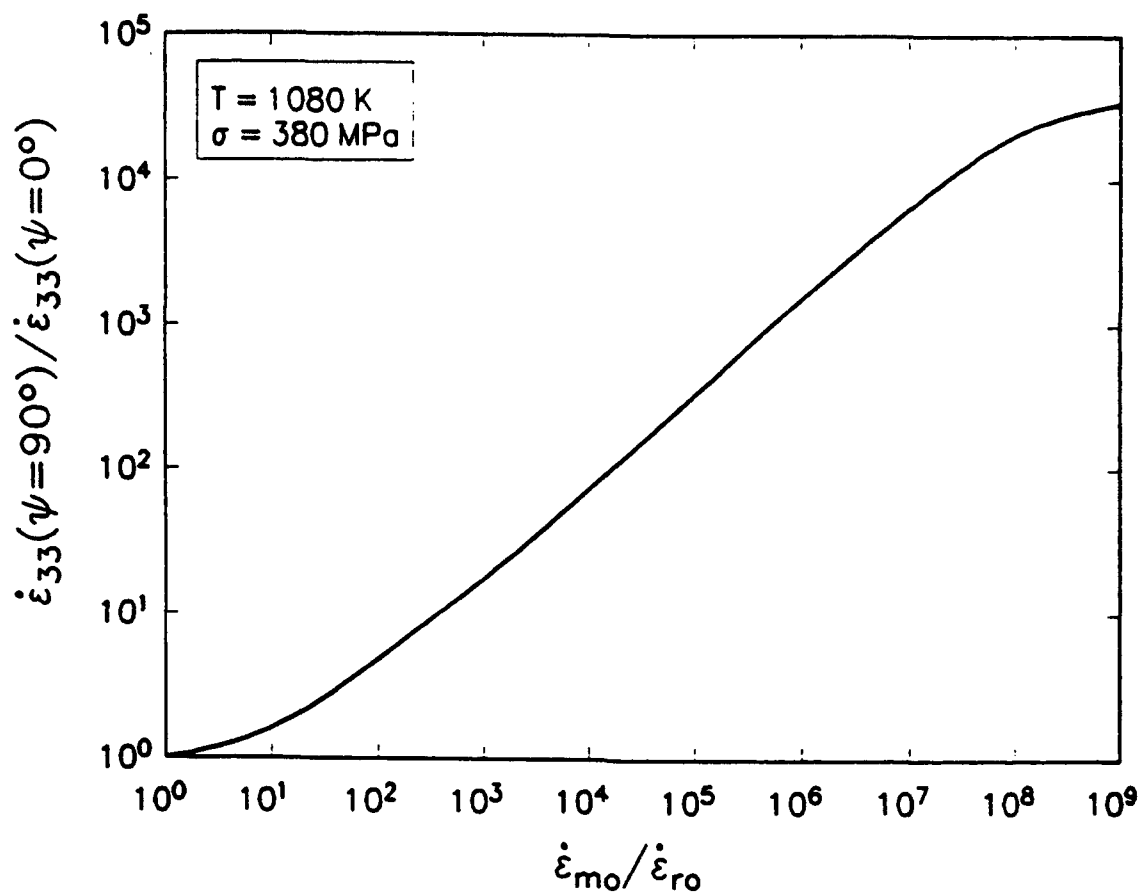


Figure 2. The effect of reinforcement creep properties (relative to the matrix creep properties), $\dot{\epsilon}_{mo}/\dot{\epsilon}_{ro}$, on the anisotropy of composite creep. The ratio $\dot{\epsilon}_{mo}/\dot{\epsilon}_{ro}$ varies from 1 to 10^9 representing the transition from a homogeneous solid to a rigid lamellar reinforced composite.

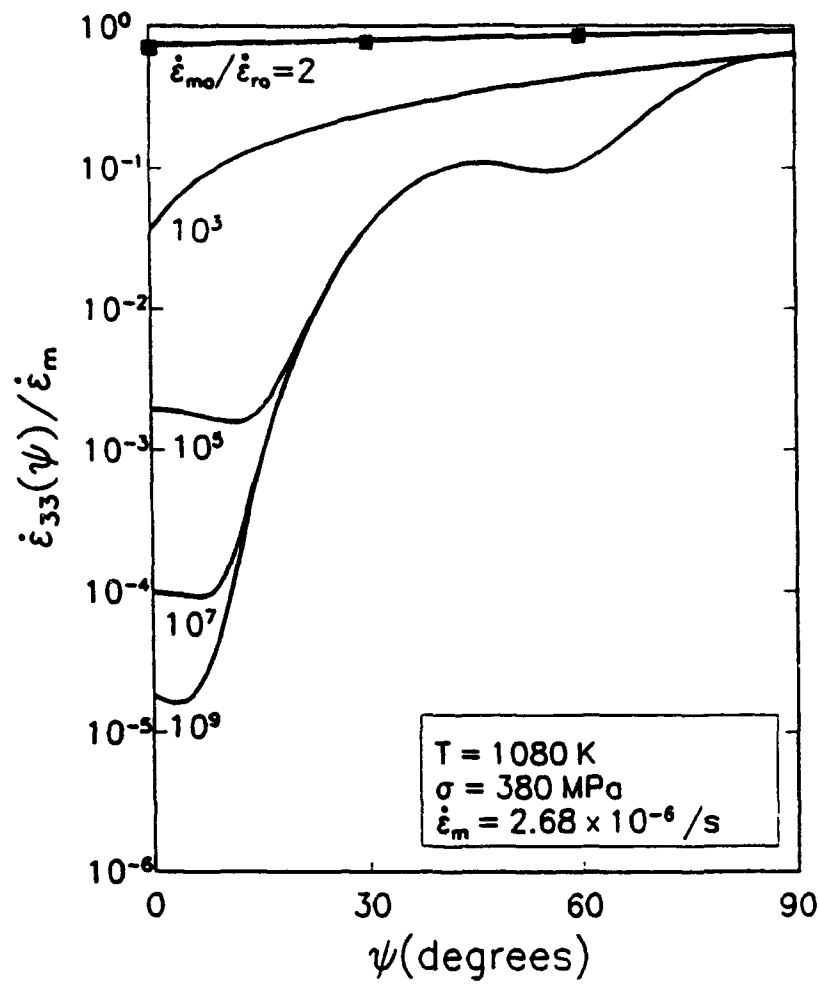


Figure 3. A series of curves for lamellar composites showing the relative composite creep rate as a function of ψ for several values of $\dot{\epsilon}_{m0}/\dot{\epsilon}_{r0}$. The curve for $\dot{\epsilon}_{m0}/\dot{\epsilon}_{r0} = 2$ represents model predictions and the solid squares represent experimentally determined relative minimum creep rates as a function of lamellae orientation for the TiAl/Ti₃Al lamellar composite deformed in compression at an applied stress of 380 MPa [16].

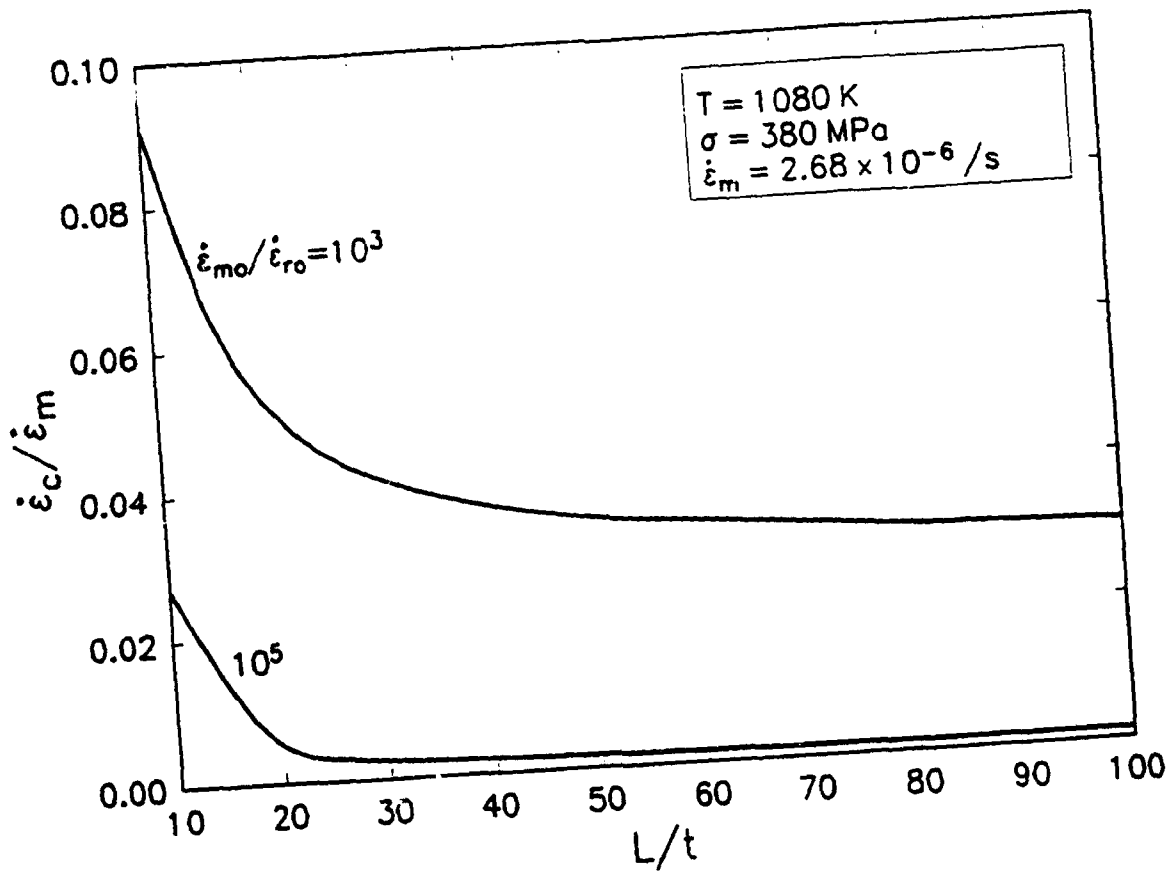


Figure 4. The effect of lamellar aspect ratio, L/t , on the relative creep rate of the composite for two values of $\dot{\epsilon}_{mo}/\dot{\epsilon}_{ro}$.

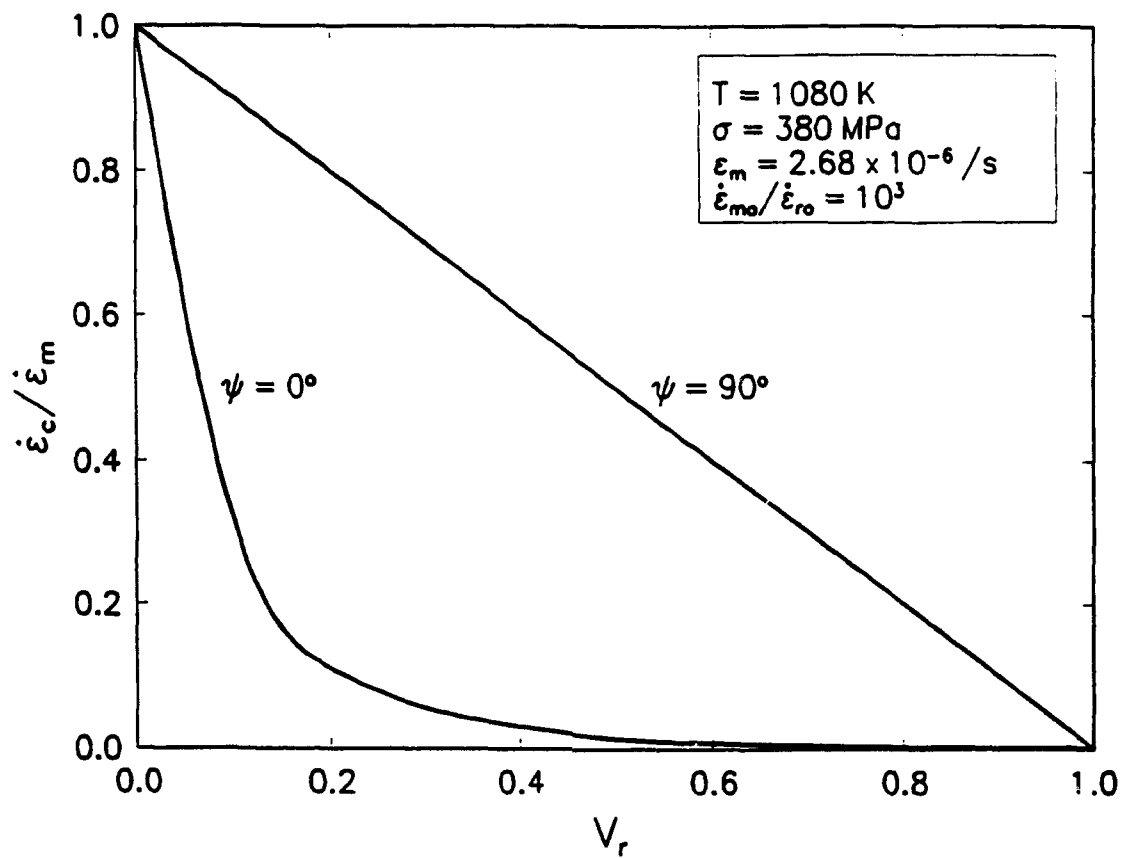


Figure 5. The effect of the reinforcing phase volume fraction, V_r , on the relative creep rate of the composite for isostrain ($\psi = 0^\circ$) and isostress ($\psi = 90^\circ$) loading conditions.

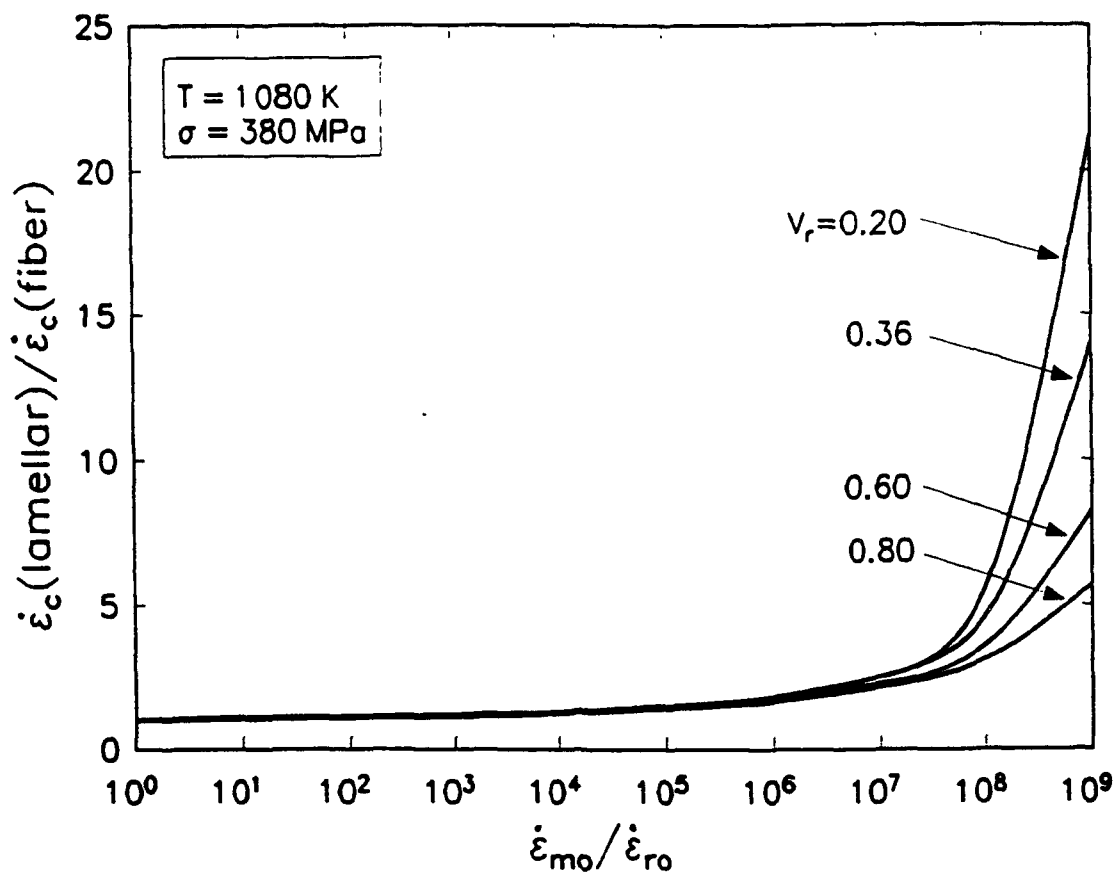


Figure 6. The ratio of the creep rate of a uniaxially aligned discontinuous *lamellar*-reinforced composite to the creep rate of a uniaxially aligned discontinuous *fiber*-reinforced composite is represented as a function of $\dot{\epsilon}_{m0}/\dot{\epsilon}_{r0}$, for several values of reinforcing phase volume fraction.

Chapter V

THE EFFECT OF THERMAL EXPOSURE ON MICROSTRUCTURAL STABILITY AND CREEP RESISTANCE OF A TWO-PHASE TiAl/Ti₃Al LAMELLAR ALLOY

I. Introduction

The low density and good oxidation resistance of TiAl and Ti₃Al ordered intermetallic alloys make them potential candidates for high temperature engineering applications [1,2]. Two-phase TiAl/Ti₃Al lamellar alloys possess a number of properties that distinguish them from the TiAl and Ti₃Al constituent single-phase alloys; namely, appreciably improved toughness, fatigue resistance and creep resistance [1-4]. Bartholomeusz and coworkers [5-7] demonstrated that the minimum creep rate of a two-phase TiAl/Ti₃Al lamellar alloy (referred to as *the lamellar alloy* in the present paper) is up to an order of magnitude lower than the creep rates of the constituent single-phase alloys. The lower creep rate of the lamellar alloy is attributed to the enhanced strain hardening of the constituent phases within the lamellar microstructure [6]. These results suggest that one approach to development of titanium aluminides as high-temperature engineering materials involves synthesis of multiphase alloys with specific phase morphologies. One of the challenges involved in developing alloys possessing multiphase microstructures for use at elevated temperatures is understanding and preventing degradation resulting from thermally induced coarsening of the microstructure.

Thermal exposure of the two-phase TiAl/Ti₃Al lamellar alloy investigated in the present study results in microstructural evolution. The lamellar microstructure undergoes capillarity driven coarsening, and ultimately transforms into a coarse, globular microstructure. The driving force for coarsening is the reduction of surface energy attained by eliminating microstructural features with small principal radii of curvature [8]. An ideal lamellar microstructure comprised of lamellae possessing flat faces is intrinsically stable; the principle radii of the flat faces are infinite and therefore no driving force exists for coarsening [8]. However, the presence of lamellae terminations (plate edges) possessing small radii of curvature, and the presence of internal boundaries, ensure microstructural coarsening of real lamellar alloys annealed at elevated temperatures. A survey of the literature yields numerous proposed coarsening mechanisms in lamellar alloys [9-16].

The objective of the present paper is to identify the mechanisms governing the microstructural evolution of a two-phase TiAl/Ti₃Al lamellar alloy subject to thermal exposure. Additionally, the effect of thermally induced microstructural evolution on the creep properties of the lamellar alloy are experimentally evaluated and modeled.

II. Experimental Procedure

Fig. 1a is a scanning electron micrograph of the two-phase TiAl/Ti₃Al lamellar alloy (44 mol.% Al) prior to thermal exposure. The microstructure is composed of lamellar packets of various orientations. Each lamellar packet consists of alternating TiAl and Ti₃Al lamellae. The darker phase (in the SEM micrographs) is the TiAl phase, which constitutes 64 vol.% of the lamellar microstructure. The average linear intercept packet diameter is 70 μm and the true thickness of the TiAl lamellae is 3.3 μm [5]. The lamellar alloy investigated in the present study possesses a type II microstructure [1]. The type II lamellar microstructure is formed via the reaction $\alpha(\text{Ti}) \Rightarrow \alpha_2(\text{Ti}_3\text{Al}) \Rightarrow \alpha_2(\text{Ti}_3\text{Al}) + \gamma(\text{TiAl})$ when the high temperature α -titanium phase is cooled. Details concerning processing of the two-phase TiAl/Ti₃Al lamellar alloy used in this study have been previously reported [5].

Specimens of the lamellar alloy were encapsulated in evacuated quartz tubes and annealed for various lengths of time between 100 and 4000 h at 1273 and 1323 K. Metallographic evaluation of the specimens was conducted using the back scattered electron imaging mode in the scanning electron microscope. The interfacial surface area-to-volume ratio (S_v) of the lamellar specimens annealed at different times and temperatures was determined using a Saltykov analysis for lamellar microstructures [17]. Following metallographic evaluation, the lamellar specimens annealed at 1323 K were compression creep tested at 1080 K under an applied true stress of 450 MPa. The stress and temperature values used in the creep tests are in the range associated with power-law creep of the lamellar alloy.

III. Microstructural Coarsening of the Two-Phase TiAl/Ti₃Al Lamellar Alloy

A. Results of Coarsening Experiments

Fig. 2 summarizes the results of the S_v measurements obtained from the specimens annealed at 1273 and 1323 K. S_v of the lamellar alloy decreases with

increasing annealing time, and the rate of change of S_v increases with increasing annealing temperature. Both of these results are consistent with the classical description of coarsening as a diffusion accommodated process occurring to lower the overall surface free energy of the system [18]. Fig. 1b - 1e depict the microstructural evolution of the lamellar alloy annealed at 1323 K for 166, 667, 1960 and 2710 h, respectively. Coarsening results in transformation of the initial lamellar microstructure into a coarse, globular microstructure. Both the TiAl phase (dark phase) and Ti_3Al phase (light phase) appear to be coarsening.

B. Summary of Coarsening Mechanisms

A comprehensive investigation by Courtney and coworkers [9,10] addresses three coarsening processes associated with the intrinsic shape instability of lamellae subject to thermal exposure: cylinderization, edge spheroidization and plate separation. During cylinderization of lamellae, capillarity drives mass transfer from the lamellar edges to their broad faces. If volume diffusion dominates mass transfer, the cylinders further coarsen by two-dimensional Ostwald ripening [19], in which large cylinders grow at the expense of smaller ones. If interfacial diffusion dominates mass transfer, each cylinder subject to a Rayleigh instability of sufficient wavelength along its length will decompose into a row of spheres [16,20]. Coarsening by cylinderization is favored for lamellae with small width-to-thickness aspect ratios. Edge spheroidization is an alternate manifestation of the cylinderization process. For lamellae possessing larger width-to-thickness aspect ratios, mass transfer is localized at lamellar edges, resulting in the evolution of lamellae possessing *pseudo-cylindrical* edges. Under the influence of a Rayleigh instability, the pseudo-cylindrical edges of lamellae separate into rows of spheres. This process continues until the width of the remaining lamellae is small enough for complete cylinderization to occur. The presence of internal boundaries in lamellae can also result in coarsening. The radius of curvature associated with interfacial tension equilibrium at the internal boundary/interphase interface junction promotes intraplate mass transfer from the boundary regions to the flat faces of the lamellae, resulting in boundary recession followed by plate separation. This process is referred to as plate splitting, and the separated plates coarsen further by cylinderization and spheroidization. Plate splitting generally occurs in lamellae possessing internal boundaries of high energy.

Lamellar terminations not only occur at the boundaries of lamellar colonies, but are also found within colonies as schematically depicted in Fig. 3a. A lamellar termination serves as a source of matter for the broad faces of the terminated lamella as well as the broad faces of adjacent lamellae [13]. Fig. 3 demonstrates how capillarity driven mass transfer results in the recession of lamellar terminations and a corresponding thickening of adjacent lamellae. The net rate of mass transport is calculated to be significantly larger for termination migration coarsening than for edge spheroidization [8]. Therefore, in alloys possessing internal lamellae terminations, termination migration is predicted to supplant edge spheroidization as the coarsening mechanism for lamellae possessing large aspect ratios.

The final coarsening process to be considered in the present paper is discontinuous coarsening [15]. Discontinuous coarsening occurs by grain boundary migration in which the moving grain boundary leaves behind a lamellar microstructure that is significantly coarser than the microstructure ahead of the grain boundary. Discontinuous coarsening is predicted to become relatively more important than termination migration coarsening at lower temperatures and finer lamellar spacings [15].

C. Discussion of the Mechanisms Responsible for Coarsening in the Lamellar Alloy

Fig. 4 is a coarsening diagram for volume diffusion control of the coarsening process for the lamellar alloy used in the present study constructed using equations A1.a - A1.d in reference [8]. The interphase interfacial energy and internal boundary energy are denoted by γ_s and γ_B , and the parameter w/t represents the coarsening plate width-to-thickness aspect ratio. The dominant coarsening mechanism for a selected combination of plate aspect ratio and internal boundary energy is defined as the mechanism yielding the greatest rate of mass transport. The diagram was constructed for coarsening phase volume fractions of 0.36 and 0.64 to obtain coarsening mechanism predictions for both the Ti_3Al and $TiAl$ constituent phases. The presence of numerous internal twin boundaries has been reported in the $TiAl$ phase of two-phase $TiAl/Ti_3Al$ lamellar alloys [21,22]. Typically, coherent twin boundary energies are lower than interfacial energies associated with semicoherent interphase interfaces [23-25]; therefore, the ratio γ_B/γ_s is expected to be smaller than 1 for the lamellar alloy evaluated in the present study. Considering the values of $TiAl$ and Ti_3Al plate aspect

ratio (21 and 39) and $\gamma_B/\gamma_S (\leq 1)$, termination migration is predicted to be the dominant coarsening mechanism for both phases in the lamellar alloy, assuming that coarsening is volume diffusion controlled [8].

Microstructural evaluation indicates that the dominant mechanism controlling coarsening of the lamellar microstructure changes with annealing time. Prior to annealing, the lamellar microstructure possesses a significant density of lamellar terminations, as seen in Fig. 1a. Lamellar terminations occur within lamellar packets (intrapacket) and at the lamellar packet boundaries (interpacket). For relatively short annealing times (i.e., 166 and 667 h at 1323 K) the general appearance of the lamellar microstructure is preserved, although an overall thickening of the lamellae can be detected. Careful examination of these specimens revealed no microstructural evidence of cylinderization, edge spheroidization or plate splitting. The thickening, or coarsening, of the lamellae coupled with the presence of numerous lamellar terminations indicates that the dominant coarsening mechanism for short annealing times is termination migration, consistent with the prediction of the coarsening diagram [8]. The microstructural evolution of lamellae depicted in Fig. 1a - 1c is very similar to the description of termination migration coarsening represented schematically in Fig. 3. The general features associated with intrapacket termination migration coarsening can be more clearly observed in Fig. 5a, a higher magnification SEM micrograph of the specimen annealed at 1323 K for 667 h. The localized thickening of lamellae adjacent to lamellar terminations is apparent. The thickening of the lamellae associated with termination migration coarsening results in an overall decrease in the average plate aspect ratio [13].

At relatively longer annealing times, 1960 and 2710 h at 1323 K, the microstructure of the lamellar alloy becomes predominantly globular. It is believed that when the aspect ratio of lamellae falls below some small critical value, as a result of termination migration coarsening, continued coarsening of the microstructure is controlled by cylinderization and conventional Ostwald ripening processes [8]. This proposition is supported by the general predictions of the coarsening diagram represented in Fig. 4: as the plate aspect ratio decreases below about 3, the overall rate of mass transfer by cylinderization approaches, and finally surpasses, that by termination migration. The change in microstructure from lamellar to globular is not a homogeneous process, as demonstrated in Fig. 1d and 1e. Some lamellar packets

persist after annealing treatments that transform most regions of the microstructure from the initial lamellar morphology into a completely globular morphology.

Examination of the micrographs in Fig. 1 reveals a second origin of termination migration coarsening: interpacket termination migration. During interpacket termination migration, mass transfer occurs from lamellar terminations at the boundaries of lamellar packets to the broad faces of lamellae in adjacent packets, as schematically depicted in Fig. 6. The arrows in Figs. 1b and 1d indicate regions in which coarsening by interpacket termination migration may have occurred. Figs. 3 and 6 demonstrate that during coarsening, the diffusion distance associated with interpacket termination migration coarsening increases more rapidly than the diffusion distance associated with intrapacket termination migration coarsening. This geometrical effect limits the contribution of interpacket termination migration coarsening to the overall termination migration coarsening rate. This conclusion is consistent with metallographic observations of annealed specimens which suggest that interpacket termination migration coarsening is restricted to a small fraction of the microstructure.

A small amount of discontinuous coarsening was also observed in the lamellar microstructure. The general features associated with discontinuous coarsening can be seen in Fig. 5b, a high magnification SEM micrograph of the lamellar specimen annealed at 1323 K for 1960 h. As noted in section IIIB, Livingston and Cahn [15] predict that discontinuous coarsening becomes relatively more important than termination migration coarsening for finer interlamellar spacings. Several investigators have evaluated the elevated temperature coarsening of two-phase TiAl/Ti₃Al lamellar alloys possessing an interlamellar spacing significantly smaller than the lamellar alloy in the present investigation [26,27]. They report that discontinuous coarsening is the dominant mechanism of microstructural evolution of the fine lamellar microstructures, consistent with the predictions of Livingston and Cahn [15].

The experimental observations described in the previous paragraphs reveal that several mechanisms contribute to coarsening of the lamellar microstructure during elevated temperature thermal exposure. For short annealing times, theoretical predictions and metallographic evaluations indicate that intrapacket termination migration is the dominant coarsening mechanism during annealing of the lamellar alloy at temperatures between 1273 and 1323 K. In section IIID, this mechanism is used as the basis for an activation energy analysis.

D. Discussion of the Activation Energy for Termination Migration Coarsening

The curvature at a TiAl lamellar termination is associated with an increased solubility of Al atoms and a decreased solubility of Ti atoms in the Ti_3Al phase adjacent to the TiAl termination [14]. The resulting concentration gradients drive interdiffusion between TiAl lamellar terminations and the broad faces of adjacent TiAl lamellae, causing recession of the termination and thickening of the adjacent lamellae. Similarly, increased solubility of Ti atoms and decreased solubility of Al atoms adjacent to a Ti_3Al lamellar termination drives Ti_3Al termination recession and thickening of the adjacent Ti_3Al lamellae. Using considerations of matter conservation, Courtney et al. [13] developed an equation relating S_v to coarsening time for lamellar composites that experience small changes in S_v :

$$S_v/S_{v0} = 1 - N\lambda Vt \quad (1)$$

where S_{v0} is the interfacial surface area-to-volume ratio at $t=0$, N is the original number of TiAl and Ti_3Al terminations per unit area (termination density), λ is the true center-to-center spacing of TiAl lamellae (which is equal to the true center-to-center spacing of Ti_3Al lamellae), and V is the velocity of termination recession.

In Fig. 2, the coarsening rate is related to the rate of change of S_v/S_{v0} with time, which decreases with increasing annealing times. For short annealing times where intrapacket termination migration is the dominant coarsening mechanism, the coarsening rate reflects the velocity of receding lamellae terminations [13,14]. Later in the coarsening process the coarsening rate decreases, probably as a result of the larger diffusion distance and/or different diffusion path associated with coarsening of the globular microstructure.

The solid lines in Fig. 2 are characteristic of the lamellar termination migration velocity for short annealing times at the two annealing temperatures. The slopes of the lines should be given by $N\lambda V$, as deduced from Eq. 1. The values of N and λ were metallographically determined for the lamellar alloy on the basis of measurements taken in over sixty individual lamellar packets. Two values of N were determined: one including only intrapacket terminations ($2.4 \times 10^6 /m^2$) and one including both intrapacket and interpacket terminations ($4.3 \times 10^6 /m^2$). The mean value of

λ (5.1×10^{-6} m) was the same in both cases. Combining the values of N and λ with S_v/S_{v0} from Fig. 2 allows the termination recession velocity to be determined.

The termination recession velocity, V , is directly related to the diffusivity by [14]:

$$V = \frac{CD}{T} \quad (2)$$

where D is the diffusivity, T is the temperature and C is a parameter that depends on several thermodynamic and microstructural factors. The thermodynamic factors include interphase interfacial energy and the partial molar volumes and equilibrium concentrations of the different atomic species in the two phases. The microstructural factors include lamellar thickness and initial center-to-center lamellar spacing. Theoretical expressions for C have been developed by several investigators for the case of eutectic lamellar composites [12,14,16]. Application of the theoretical expressions has yielded very good agreement with experimentally measured values of termination recession velocity [14].

To determine Q , the activation energy for the rate-controlling diffusion process governing termination migration coarsening, C is assumed to be temperature independent. This is a reasonable assumption since over the temperature range 1273 to 1323 K the compositions of the phases predicted by the phase diagram do not change appreciably [28]. If C is temperature independent, Q can be determined from the values of V at the two annealing temperatures. The resulting activation energy for the rate-controlling diffusion process governing termination migration coarsening is 215 kJ/mol.

The activation energy for power-law creep of the lamellar alloy has been reported as 407 kJ/mol [5], about double that determined for coarsening of the lamellar microstructure. The following paragraphs present two views of these observations.

- i) At temperatures greater than about $0.6T_m$, the activation energy for creep is found to equal the activation energy for volume diffusion for a large number of materials [29,30-33]. It is also well established that the activation energy for boundary diffusion accommodated processes is approximately half that of

volume diffusion accommodated processes [34,35]. These results suggest that the rate controlling process during termination migration coarsening of the lamellar alloy could be an interface boundary diffusion accommodated process, possibly associated with reorganization of the semicoherent interphase interfaces during termination recession, rather than the volume diffusion of atoms between receding lamellar terminations and adjacent broad faces. In support of this proposition, calculations by Cline [16] demonstrate that retention of semicoherent interfaces can retard termination recession during termination migration coarsening.

- ii) Alternatively, in many alloy systems (monolithic and composite) the activation energy for creep has been reported to be up to 2.5 times larger than the activation energy for volume diffusion [32,33,36-39]. Therefore, it is possible that the activation energy reported for creep is significantly larger than the activation energy for volume diffusion in the lamellar alloy. Furthermore, the observation of conventional Ostwald ripening processes at long annealing times is indicative of coarsening controlled by volume diffusion. This result suggests that at temperatures between 1273 and 1323 K either volume diffusion controls coarsening for all annealing times, or volume diffusion becomes the rate controlling process at later annealing times when the total interfacial boundary area has significantly decreased.

The uncertainty of interpretation of the activation energy for creep in the lamellar alloy and the lack of appropriate diffusion data hinder identification of the rate controlling process governing termination migration coarsening. Recently, Kroll and coworkers [40] have reported that the activation energy for Ti diffusion in a single-phase TiAl alloy (54 mol.% Al) is 291 kJ/mol. Furthermore, diffusion couple experiments indicate that the activation energy for diffusion of Al in TiAl is higher than the activation energy for diffusion of Ti in TiAl [41]. These results support the proposition that boundary diffusion processes control the initial coarsening of the lamellar alloy.

Fig. 1a and Fig. 1b demonstrate that annealing at 1323 K for 166 h results in little change in the appearance of the lamellar microstructure. The good elevated temperature microstructural stability of the lamellar alloy is predominantly due to the low density of intrapacket terminations, approximately three orders of magnitude lower than the density of terminations observed in a eutectic alloy [13]. Titanium aluminides

are being developed for service temperatures of about 1100 K. Using the value of activation energy for termination migration coarsening determined in the present study, the relative microstructural stability of the lamellar alloy at 1100 K can be predicted. Annealing at 1323 K for 166 h results in coarsening such that $S_v/S_{v0} = 0.935$. A corresponding change in S_v/S_{v0} for the lamellar alloy annealed at 1100 K is predicted to take approximately 10^4 h. These results indicate that the thermal stability of the lamellar microstructure in its proposed service temperature range is excellent.

IV. Effect of Microstructural Evolution on the Creep Properties of the Two-Phase TiAl/Ti₃Al Lamellar Alloy

A. Results of Creep Tests

Fig. 7 represents the results of compression creep tests carried out at 1080 K under an applied true stress of 450 MPa for an unannealed specimen of the lamellar alloy, and for specimens of the lamellar alloy annealed at 1323 K for 166, 667, 1960 and 2710 h prior to creep testing. Fig. 7 demonstrates three important effects of coarsening on the creep properties of the lamellar alloy. First, the minimum creep rate of the lamellar alloy in the secondary creep regime increases with increasing prior annealing time. Second, the primary creep strain of the lamellar alloy also increases with increasing prior annealing time. Third, the increase in secondary creep rate with strain for an individual specimen decreases with increasing prior annealing time. For the specimens annealed for 1960 and 2710 h, the secondary creep rate appears to be independent of strain. In the following sections, these observations will be reconciled with a phenomenological model for creep of the lamellar alloy.

B. Discussion of the Effect of Coarsening on the Minimum Creep Rate

The TiAl/Ti₃Al lamellar alloy discussed in the present paper exhibits a minimum creep rate more than an order of magnitude lower than the minimum creep rates of single-phase TiAl and Ti₃Al alloys, at the same stress and temperature [5]. This result has been shown to arise from the difference in creep properties of the TiAl and Ti₃Al phases within the lamellar microstructure, compared to the creep properties of the single-phase alloys. Rao and Tangri [42] reported that the work hardening rate of the lamellar alloy is about an order of magnitude higher than the work hardening rate of the single-phase alloys in the temperature range where creep testing has been performed.

Since power-law creep can be regarded as a competition between recovery and work hardening [43,44], an increase in the work hardening rate promotes a lower minimum creep rate.

Although the cause of the high work hardening rate of the lamellar alloy relative to its constituent phases has not been conclusively established, the high density of interphase interfaces in the lamellar alloy may be a contributing factor. A previous experimental study revealed TiAl/Ti₃Al interfaces to be rich sources of dislocations during deformation [45]. Modeling by Van Der Merwe, Shiflet and Stoop [46] demonstrates that stresses generated at structural ledges on semicoherent interfaces can be large enough to emit mobile dislocations into the adjacent phases. The conjecture that the high density of interphase interfaces provides a high density of dislocation sources in the lamellar alloy is also consistent with predictions of Weertman's model [47] for power-law creep. In this model, the steady-state creep rate is inversely proportional to the density of dislocation sources, M :

$$\dot{\epsilon}_{ss} \propto \frac{1}{\sqrt{M}}. \quad (3)$$

The model therefore predicts that coarsening of the lamellar microstructure should increase the steady-state creep rate. In the present analysis, the minimum creep rate in the secondary creep regime is considered equivalent to the steady-state creep rate. Fig. 7 shows that coarsening results in an increase in the minimum creep rate, consistent with the model predictions.

The previous discussion shows that numerous experimental observations and modeling results are consistent with the hypothesis that the interphase interfaces in the lamellar alloy act as dislocation sources during deformation, and that these interfaces therefore contribute to the high work hardening rate and the low minimum creep rate of the lamellar alloy. Assuming this hypothesis to be correct, the effect of coarsening of the lamellar microstructure on the minimum creep rate can be modeled. To formulate such a model it is convenient to relate the density of dislocation sources to S_v , a readily measurable parameter. If the density of dislocation sources per unit interphase interface area is assumed to be relatively insensitive to the changing microstructural morphology during coarsening, the minimum creep rate of the lamellar alloy can be

expressed as:

$$\dot{\epsilon}(S_v) = \dot{\epsilon}(S_{v0}) \sqrt{\frac{S_{v0}}{S_v}} \quad (4)$$

where $\dot{\epsilon}(S_{v0})$ is the minimum creep rate of the unannealed lamellar alloy possessing an interfacial area-to-volume ratio of S_{v0} , and $\dot{\epsilon}(S_v)$ is the minimum creep rate of a coarsened lamellar specimen possessing an interfacial area-to-volume ratio of S_v .

In Fig. 8, the experimentally determined minimum creep rates of the lamellar specimens annealed at 1323 K are plotted as a function of S_v/S_{v0} (filled squares). The results of the dislocation source density model represented by Eq. 4 are also represented in Fig. 8 by the solid curve. For short annealing times ($S_v/S_{v0} > 0.7$), agreement between the model predictions and experimental results is good. At longer annealing times ($S_v/S_{v0} < 0.7$), the experimentally determined minimum creep rates are higher than those predicted by the model. In the remainder of Section IVB, the difference between the experimental and predicted creep rates after long annealing times is explained in terms of the different *composite strengthening conditions* that prevail for lamellar and globular microstructures.

Bartholomeusz and Wert [6] have formulated a composite strength model to predict the creep rate of composites reinforced by aligned discontinuous lamellae. Lamellae orientation with respect to the uniaxial stress axis was found to affect the creep resistance of lamellar alloys. Lamellae oriented parallel and perpendicular to the uniaxial stress represent the upper and lower bound creep strength conditions. The difference between the upper and lower bound creep strengths of a lamellar alloy is a strong function of the difference in creep strengths of the individual constituent phases [48]. The difference in creep strengths of the constituent phases for the TiAl/Ti₃Al lamellar alloy used in the present investigation is relatively small, resulting in a modest difference between the upper and lower bound creep strengths of the lamellar alloy. Bartholomeusz and Wert [6] reported that the arithmetic mean of the upper and lower bound creep strengths was a good approximation of the creep strength of the lamellar alloy possessing randomly oriented lamellar packets.

Mechanically, the globular microstructure is approximately equivalent to the case of lamellae aligned perpendicular to the applied stress, the morphology representing the lower bound creep strength of the lamellar alloy. Therefore, microstructural evolution during coarsening should degrade the creep resistance of the lamellar alloy toward the lower bound creep strength prediction. The lower bound creep strength differs from the arithmetic mean of the upper and lower bound creep strengths for the lamellar alloy by approximately a factor of 1.2 [6]. This factor represents the increase in minimum creep rate of the lamellar alloy when the microstructure transforms from randomly oriented lamellar packets to predominantly globular. The microstructures of the lamellar alloys annealed for the two longest times ($S_v/S_{v0} < 0.7$) are predominantly globular in appearance. If the minimum creep rates of the specimens with predominantly globular microstructures are multiplied by the factor 1.2 that reflects the decrease in creep resistance associated with the morphology change, the dotted curve in Fig. 8 is obtained. The excellent agreement between the predicted and experimentally measured minimum creep rates of the lamellar alloy at the two longest annealing times shows that the creep results can be adequately accounted for by considering changes in microstructural morphology.

The concepts used to derive Eq. 4 assume that the dependence of work hardening rate on S_v , and the change in composite strengthening during coarsening are the primary factors contributing to the increase in minimum creep rate during coarsening. The good agreement shown in Fig. 8 between the predicted and experimentally determined values of minimum creep rate supports the contention that the interphase interfaces strongly contribute to work hardening of the lamellar alloy. It is notable that microstructural evolution during coarsening has only a modest effect on the minimum creep rate of the lamellar alloy.

C. Discussion of the Effect of Coarsening on Primary Creep Strain

From the creep curves depicted in Fig. 7, the primary creep strain for the unannealed and annealed lamellar specimens can be determined by extrapolating the portion of the creep curve representing the minimum creep rate to the total strain axis. The measured values of primary creep strain, represented as filled squares in Fig. 9, demonstrate that coarsening degrades the primary creep resistance of the lamellar alloy. The parameter ϵ_p/ϵ_{p0} represents the primary creep strain of the lamellar alloy after coarsening to a particular value of S_v , normalized by the primary creep strain of

the lamellar alloy prior to annealing. The very small primary creep strain of the unannealed lamellar alloy has been attributed to the enhanced work hardening rate of the constituent phases within the lamellar microstructure [5,43].

McLean [43] has developed an expression relating the primary creep strain to the work hardening rate:

$$\epsilon_p = \frac{kT}{\Delta A b h} \ln \left(\frac{\dot{\epsilon}_0}{\dot{\epsilon}_{ss}} \right) \quad (5)$$

where ϵ_p is the primary creep strain, $\dot{\epsilon}_0$ is the strain rate at time = 0, $\dot{\epsilon}_{ss}$ is the steady-state creep rate, h is the work hardening rate, b is the Burger's vector, T is temperature, k is Boltzmann's constant and ΔA is the activation area. In Section IVB it was proposed that, as S_v decreases during coarsening, the density of dislocation sources associated with the interphase interfaces decreases and results in a reduction of the work hardening rate of the lamellar alloy. Examination of Eq. 5 reveals that a decrease in the work hardening rate results in an increase in the primary creep strain, consistent with the experimental results (filled squares) represented in Fig. 9.

The values of the parameters in Eq. 5 have been estimated to allow quantitative comparison with the experimental results represented in Fig. 9. The creep test temperature was 1080K. The work hardening rate (h) at 1080 K for two-phase TiAl/Ti₃Al lamellar alloys has been previously reported to be approximately 3000 MPa [42]. The steady-state creep rate, $\dot{\epsilon}_{ss}$, increases with increasing annealing time from 3.2×10^{-6} /s for the unannealed specimen to 5.3×10^{-6} /s for the specimen annealed at 1323 K for 2710 h. The magnitude of the Burgers vectors of TiAl and Ti₃Al falls within the range 0.3 nm to 0.6 nm [45,49,50]. The values of $\dot{\epsilon}_0$ were measured and found to increase with increasing annealing time from 4.7×10^{-6} /s for the unannealed specimen to 1.6×10^{-5} /s for the specimen annealed at 1323 K for 2710 h. Finally, ΔA is proportional to the stress exponent for power law creep, n , and the inverse of the applied true stress, σ [44]:

$$\Delta A = \frac{kTn}{b\sigma} \quad (6)$$

The value of stress exponent for the lamellar alloy has been reported to be 5.4 [5]. Since the creep tests in the present study were carried out for an applied true compressive stress of 450 MPa, the appropriate value of ΔA is $3.6 \times 10^{-19} \text{ m}^2$.

Inserting the values discussed in the previous paragraph into Eq. 5 yields the solid lines depicted in Fig. 9, where the normalized primary creep strain is plotted as a function of the normalized work hardening rate, h/h_0 . A decrease in the work hardening rate from h_0 to h is reflected by an increase in the primary creep strain from ϵ_{p0} to ϵ_p . In the case of the lamellar alloy, h_0 and ϵ_{p0} represent the work hardening rate and primary creep strain of the unannealed specimen. Two solid curves are depicted in Fig. 9 to represent the range of values associated with the individual parameters (i.e., b , $\dot{\epsilon}_{ss}$ and $\dot{\epsilon}_0$) used in Eq. 5. Aside from the range of values for the individual parameters, no adjustable parameters are involved in the prediction of ϵ_p/ϵ_{p0} shown in Fig. 9.

The experimentally determined values of primary creep strain and the predictions of Eq. 5 represented in Fig. 9 can be directly compared using the assumption that the work hardening rate of the lamellar alloy varies linearly with the interphase interface area per unit volume, S_v . The excellent agreement between the experimental data and the theoretically predicted range in Fig. 9 demonstrates that the reduction in work hardening rate with S_v during coarsening can account for the observed increase in primary creep strain. This result provides further evidence for the important effect of interphase interfaces on the creep resistance of the lamellar alloy. In contrast to the case of the minimum creep rate, the primary creep strain of the lamellar alloy increases quite significantly as a result of microstructural coarsening.

D. Discussion of the Effect of Coarsening on Secondary Creep Rate Evolution with Strain

The secondary creep rate for the unannealed lamellar alloy increases with increasing strain, as shown in Fig. 7. Since the creep tests were conducted in compression at a constant true stress, this is not a tertiary creep phenomenon. During creep, the lamellar microstructure undergoes deformation-induced spheroidization and transforms into a fine equiaxed duplex microstructure. It is important to differentiate between deformation-induced spheroidization and thermally-induced spheroidization. Thermally-induced spheroidization is a coarsening process, whereas deformation-induced spheroidization is a strain-driven process in which the total interphase

interfacial area per unit volume increases [5,51]. Fig. 10a is a SEM micrograph of an unannealed lamellar specimen tested at 1080 K to a true strain of 0.46. The individual lamellar plates are seen to have undergone substantial shearing and bending, and spheroidization is prevalent in the interpacket regions. The increase in secondary creep rate with deformation-induced spheroidization is a result of acceleration of creep processes in the spheroidized regions of the microstructure. Therefore, as the volume fraction of the spheroidized lamellar microstructure increases with strain, the secondary creep rate of the lamellar alloy increases. The effect of deformation-induced spheroidization on the creep properties of the lamellar alloy will be the topic of a subsequent paper.

Fig. 7 demonstrates that the increase in secondary creep rate with strain for specimens of the lamellar alloy decreases with increasing prior annealing time. For the specimens annealed for 1960 and 2710 h at 1323 K, the secondary creep rate is essentially independent of the total strain. Fig. 10b is a SEM micrograph of the specimen annealed at 1323 K for 2710 h, then crept at 1080 K to a true strain of 0.43. Comparing Figs. 1e and 10b demonstrates that the appearance of the globular microstructure does not change appreciably during creep deformation, in contrast to the substantial changes observed in the lamellar microstructure as a consequence of creep. Therefore, during annealing, as the microstructure of the lamellar alloy transforms to a globular microstructure, the amount of spheroidization occurring during subsequent creep decreases, and the secondary creep rate of the alloy becomes increasingly strain independent.

V. Conclusions

(1) During annealing of the two-phase TiAl/Ti₃Al lamellar alloy at 1273 and 1323 K, the lamellar microstructure evolves into a coarse, globular microstructure. For short annealing times (less than about 1000 h at these temperatures) microstructural evolution occurs predominantly by intrapacket termination migration coarsening. For longer annealing times, cylinderization and conventional Ostwald ripening coarsening mechanisms are observed. Limited interpacket termination migration and discontinuous coarsening were also observed.

(2) The activation energy for intrapacket termination migration coarsening of the lamellar microstructure was determined to be 215 kJ/mol.

(3) The minimum creep rate of the lamellar alloy increases with increasing prior annealing time. Modeling demonstrates that the increase in the minimum creep rate of the lamellar alloy during annealing can be accounted for by consideration of two factors: the decrease in the work hardening rate of the lamellar alloy in response to the overall decrease in interphase interfacial area, and the decreased mechanical strengthening effect associated with transformation from a lamellar to a globular microstructure.

(4) The primary creep strain of the lamellar alloy increases with increasing annealing time. Modeling demonstrates that the increase in primary creep strain of the lamellar alloy as a result of coarsening can be accounted for by the decrease in the work hardening rate of the lamellar alloy resulting from the overall decrease in interphase interfacial area during coarsening.

(5) Deformation-induced spheroidization results in an increase of the secondary creep rate of the unannealed lamellar alloy with creep strain. Specimens of the lamellar alloy annealed for long times (in excess of 1000 h at temperatures near 1300 K) possess a predominantly globular microstructure. The globular microstructure is not susceptible to deformation-induced spheroidization, and creep tests of specimens with globular microstructures reveal that the secondary creep rate is essentially independent of strain.

VI. Acknowledgments

We would like to express our appreciation to several of our colleagues who have made valuable contributions to various aspects of this work: Professors T.H. Courtney, J.M. Howe, F.W. Wawner, R.A. Johnson and D.P. Pope. We would also like to acknowledge Prof. K.R. Lawless and Mr. H. Koenigsmann for their assistance on the SEM. This work was sponsored by AOFSR under contract number AOFSR-90-0143; Capt. C. Ward and Dr. A. Rosenstein were the contract monitors.

VII. References

1. Y.W. Kim and D.M. Dimiduk: *JOM*, 1991, vol. 43, no. 8, pp. 40-7.
2. H.A. Lipsitt, D. Shechtman and R.E. Schafrik: *Metall. Trans. A*, 1980, vol. 11A, pp. 1369-75.
3. S. Mitao, S. Tsuyama and K. Minakawa: *Mater. Sci. Eng.*, 1991, vol. 143A, pp. 51-62.
4. S. Reuss and H. Vehoff: *Scripta Metall. Mater.*, 1990, vol. 24, pp. 1021-26.
5. M.F. Bartholomeusz, Q. Yang and J.A. Wert: *Scripta Metall. Mater.*, 1993, vol. 29, pp. 389-94.
6. M.F. Bartholomeusz and J.A. Wert, "Modeling Creep Deformation of a Two-Phase TiAl/Ti₃Al Alloy with a Lamellar Microstructure", submitted to *Metall. Trans. A*, 1994.
7. M.F. Bartholomeusz and J.A. Wert, "Measurement of the Compressive Creep Strain Rates of the Individual Phases within a Lamellar Microstructure", submitted to *Materials Characterization*, 1994.
8. T.H. Courtney, in *Metal Matrix Composites-Processing, Microstructure and Properties*, N. Hansen, D.J. Jensen, T. Leffers, H. Liholt, T. Lorentzen, A.S. Pederson, O.B. Pederson and B. Ralph (eds.), Riso National Laboratory, Roskilde, Denmark, 1991, pp. 17-29.
9. J.C. Malzahn Kampe, T.H. Courtney and Y. Leng: *Acta Metall. Mater.*, 1989, vol. 37, pp. 1735-45.
10. T.H. Courtney and J.C. Malzahn Kampe: *Acta Metall. Mater.*, 1989, vol. 7, pp. 1747-58.
11. Y.G. Nakagawa and G.C. Weatherly: *Metall. Trans. A*, 1972, vol. 3A, pp. 3223-9.
12. L.D. Graham and R.W. Kraft: *Trans. TMS-AIME*, 1966, vol. 19, pp. 94-101.
13. L.Y. Lin, T.H. Courtney and K.M. Ralls: *Acta Metall. Mater.*, 1977, vol. 25, pp. 99-106.
14. L.Y. Lin and T.H. Courtney: *Metall. Trans. A*, 1974, vol. 5A, pp. 513-4.
15. J.D. Livingston and J.W. Cahn: *Acta Metall. Mater.*, 1974, vol. 22, pp. 495-503.
16. H.E. Cline: *Acta Metall. Mater.*, 1971, vol. 19, pp. 481-90.
17. W. Ostwald: *Z. phys. Chem.*, 1900, vol. 34, pp. 495-512.
18. J.W. Martin and R.D. Doherty: *Stability of Microstructure in Metallic Systems*, Cambridge University Press, Cambridge, 1976, pp. 154-244.
19. E. Underwood, in *Metals Handbook*, vol. 8, ASM, Metals Park, Ohio, 1973, pp. 37-47.
20. Lord Rayleigh: *Lond. Math Soc. Proc.*, 1879, vol. 10, pp. 4-13.
21. S.R. Singh and J.M. Howe: *Philos. Mag. Lett.*, 1992, vol. 65, pp. 233-241.
22. C.R. Feng, D.J. Michel and C.R. Crowe: *Mater. Sci. Eng.*, 1991, vol. 145A, pp. 257-64.
23. L.E. Murr: *Interfacial Phenomena in Metals and Alloys*, Addison-Wesley Publishing Co., London, 1975, pp. 130-57.

24. N. Prabhu and J.M. Howe: *Acta Metall. Mater.*, 1990, vol. 38, pp. 889-96.
25. D.A. Porter and K.E. Easterling: *Phase Transformations in Metals and Alloys*, Chapman and Hall, London, 1990, pp. 142-72.
26. D.S. Shong and Y.W. Kim: *Scripta Metall. Mater.*, 1989, vol. 23, pp. 257-61.
27. Y. Zheng, L. Zhao and K. Tangri: *Scripta Metall. Mater.*, 1992, vol. 26, pp. 219-24.
28. J.L. Murray: *Metall. Trans. A*, 1988, vol. 19A, pp. 243-7.
29. O.D. Sherby, R.H. Klundt and A.K. Miller: *Metall. Trans. A*, 1977, vol. 8A, pp. 843-50.
30. R.S. Polvani, W.S. Tzeng and P.R. Strutt: *Metall. Trans. A*, 1976, vol. 7A, pp. 33-40.
31. K.J. Hemker and W.D. Nix: *Metall. Trans. A*, 1993, vol. 24A, pp. 335-41.
32. G.F. Hancock and B.R. McDonnell: *physica status solidi*, 1971, vol. 4, pp. 143-50.
33. M. Rudy and G. Sauthoff, in *High temperature Ordered Intermetallic Alloys*, C.C. Koch, C.T. Liu and N.S. Stoloff (eds.), MRS, Pittsburgh, PA, 1985, pp. 327-33.
34. H.B. Aaron and H.I. Aaronson: *Acta Metall. Mater.*, 1968, vol. 16, pp. 789-98.
35. H.J. Frost and M.F. Ashby: *Deformation-Mechanism Maps*, Pergamon Press Ltd, Oxford, 1982, pp. 7-16.
36. H. Oikawa, in *High Temperature Aluminides & Intermetallics*, S.H. Wang, C.T. Liu, D.P. Pope and J.O. Stiegler (eds.), TMS, Warrendale, PA, 1989, pp. 353-73.
37. K.T. Park, E.J. Lavernia and F.A. Mohamed: *Acta Metall. mater.*, vol. 38, pp. 2149-21.
38. G. Gonzalez-Doncel and O.D. Sherby: *Acta Metall. Mater.*, 1993, vol. 41, pp. 2797-805.
39. S. Kroll, H. Mehrer, N. Stolwijk, C. Herzig, R. Rosenkranz and G. Frommeyer: *Z. Metallkunde*, 1992, vol. 83, pp. 591-5.
40. S. Kroll, H. Mehrer, N. Stolwijk, C. Herzig, R. Rosenkranz and G. Frommeyer: *Z. Metallkd.*, 1992, vol. 8, pp. 591-595.
41. H. Mehrer, W. Sprengel and M. Denkingen in *Diffusion in Ordered Alloys*, B. Fultz, R.W. Cahn and D. Gupta (eds.), TMS, Warrendale, PA, 1993, pp. 51-67.
42. P.P. Rao and K. Tangri: *Mater. Sci. Eng.*, 1991, vol. 132A, pp. 49-59.
43. D. McLean: *Progress in Physics*, 1966, vol. 29, pp. 1-33.
44. J.P. Poirier: *Creep of Crystals*, Cambridge University Press, Cambridge, 1985, pp. 76-144.
45. F. Appel, P.A. Beaven and R. Wagner: *Acta Metall. Mater.*, 1993, vol. 41, pp. 1721-1732.
46. J.H. Van Der Merwe G.J. Shiflet and P.M. Stoop: *Metall Trans. A*, 1991, vol. 22A, pp. 1165-75.
47. J. Weertman: *Trans. A.S.M.*, 1968, vol. 61, pp. 681-94.

48. M.F. Bartholomeusz and J.A. Wert, "Modeling the Minimum Creep Rate of an In-Situ TiAl/Ti₃Al Lamellar Composite", manuscript in preparation for submission to 1994 TMS Annual Meeting.
49. G.J. Mahon and J.M. Howe: *Metall. Trans. A*, 1990, vol. 21A, pp. 1655-62.
50. S.A. Court, J.P.A. Lofvander, M.H. Loretto and H.L. Fraser: *Philos. Mag.*, 1990, vol. 61, pp. 109-39.
51. J.A. Wert: *JOM*, 1982, vol. 34, no. 9, pp. 35-41.

List of Figures

Figure 1. SEM micrographs of specimens of the lamellar alloy: (a) Unannealed. (b) Annealed at 1323 K for 166 h. (c) Annealed at 1323 K for 667 h. (d) Annealed at 1323 K for 1960 h. (e) Annealed at 1323 K for 2710 h. The darker phase is the TiAl phase and the lighter phase is the Ti_3Al phase.

Figure 2. Variation of interfacial surface area-to-volume ratio (S_v) with time for specimens of the lamellar alloy annealed at 1273 and 1323 K.

Figure 3. Schematic of intrapacket termination migration coarsening during elevated temperature annealing of a lamellar microstructure: (a) Unannealed microstructure, (b)-(c) Microstructure at successively longer annealing times.

Figure 4. Coarsening diagram for volume diffusion controlled coarsening of lamellar microstructures [8].

Figure 5. (a) SEM micrograph of the lamellar specimen annealed at 1323 K for 667 h depicting microstructural characteristics associated with termination migration coarsening. (b) SEM micrograph of the lamellar specimen annealed at 1323 K for 1960 h depicting microstructural characteristics associated with discontinuous coarsening. The dark phase is the TiAl Phase.

Figure 6. Schematic of interpacket termination migration coarsening during elevated temperature annealing of lamellar microstructure.

Figure 7. Compression creep curves at 1080 K and 450 MPa for unannealed and previously annealed (1323 K) specimens of the lamellar alloy.

Figure 8. The effect of the change in interfacial surface area-to-volume ratio (S_v) during coarsening on the minimum creep rate of the lamellar alloy. The filled squares represent experimental results. The solid line represents model results that account for the change of hardening rate. The dashed line represents model results that account for both the change of hardening rate and the effect of morphology on composite strengthening.

Figure 9. The filled squares represent the experimentally measured dependence of primary creep strain on the change in interfacial surface area-to-volume ratio (S_v/S_{v0}) during coarsening of the lamellar microstructure. The continuous curves represent model predictions of the dependence of primary creep strain on the change in work hardening rate (h/h_0) during coarsening of the lamellar microstructure.

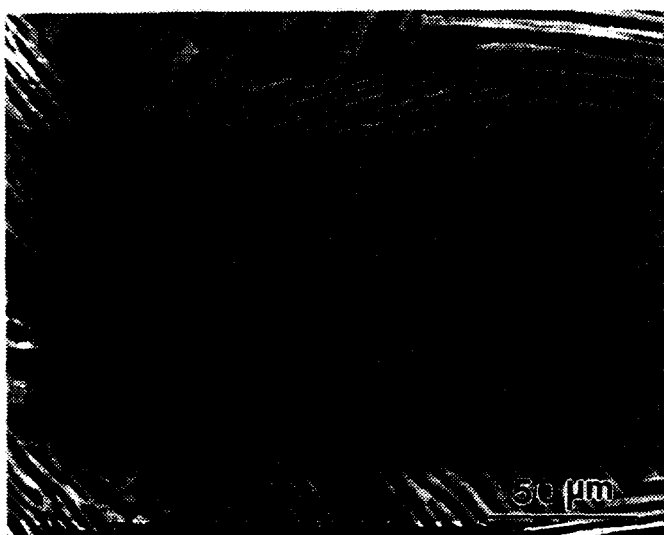
Figure 10. SEM micrographs of specimens of the lamellar alloy: (a) Unannealed and crept in compression at 1080 K and 450 MPa to a true strain of 0.46. (b) Annealed at 1323 K for 2710 h and crept in compression at 1080 K and 450 MPa to a true strain of 0.43. The dark phase is the TiAl Phase.



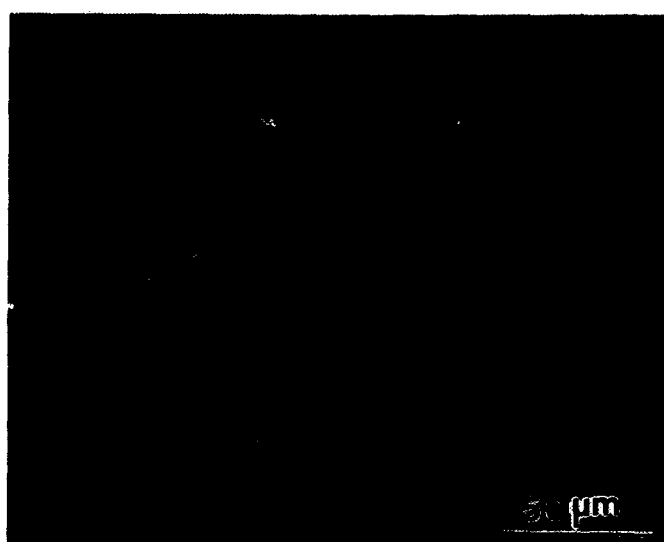
(a)



(b)



(c)



(d)



(e)

Figure 1. SEM micrographs of specimens of the lamellar alloy: (a) Unannealed. (b) Annealed at 1323 K for 166 h. (c) Annealed at 1323 K for 667 h. (d) Annealed at 1323 K for 1960 h. (e) Annealed at 1323 K for 2710 h. The darker phase is the TiAl phase and the lighter phase is the Ti₃Al phase.

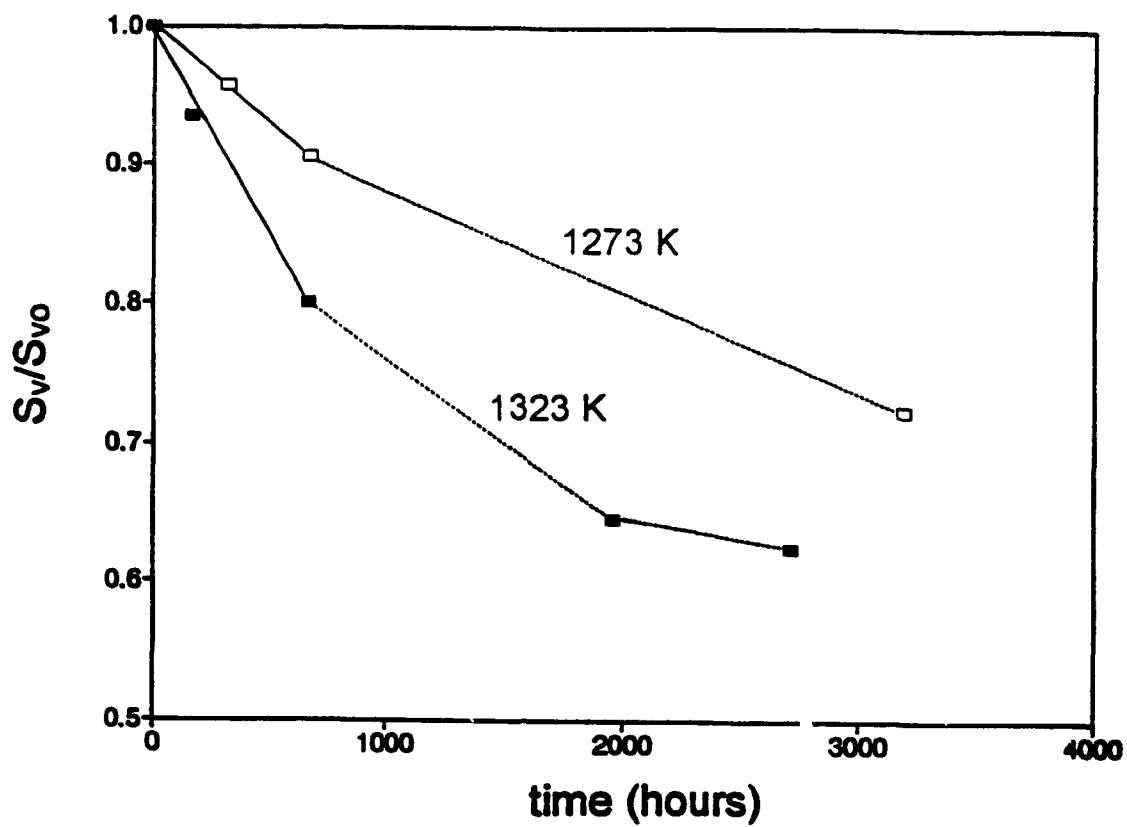
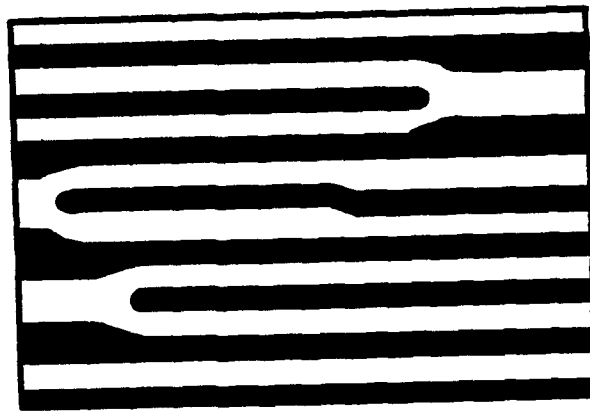
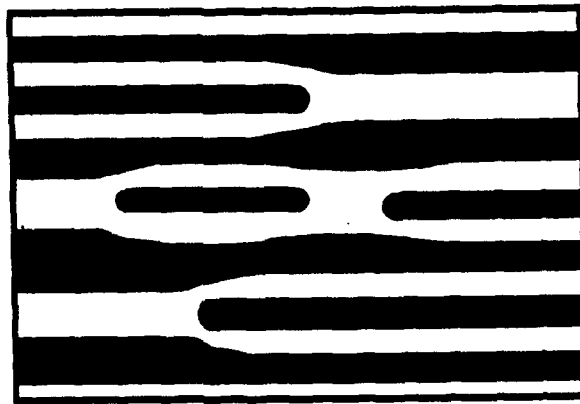


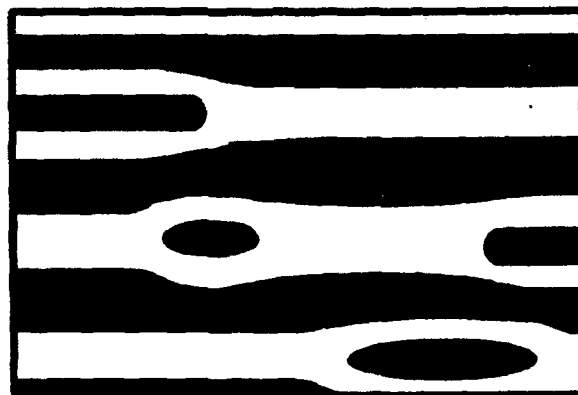
Figure 2. Variation of interfacial surface area-to-volume ratio (S_v) with time for specimens of the lamellar alloy annealed at 1273 and 1323 K.



(a)



(b)



(c)

Figure 3. Schematic of intrapacket termination migration coarsening during elevated temperature annealing of a lamellar microstructure: (a) Unannealed microstructure, (b)- (c) Microstructure at successively longer annealing times.

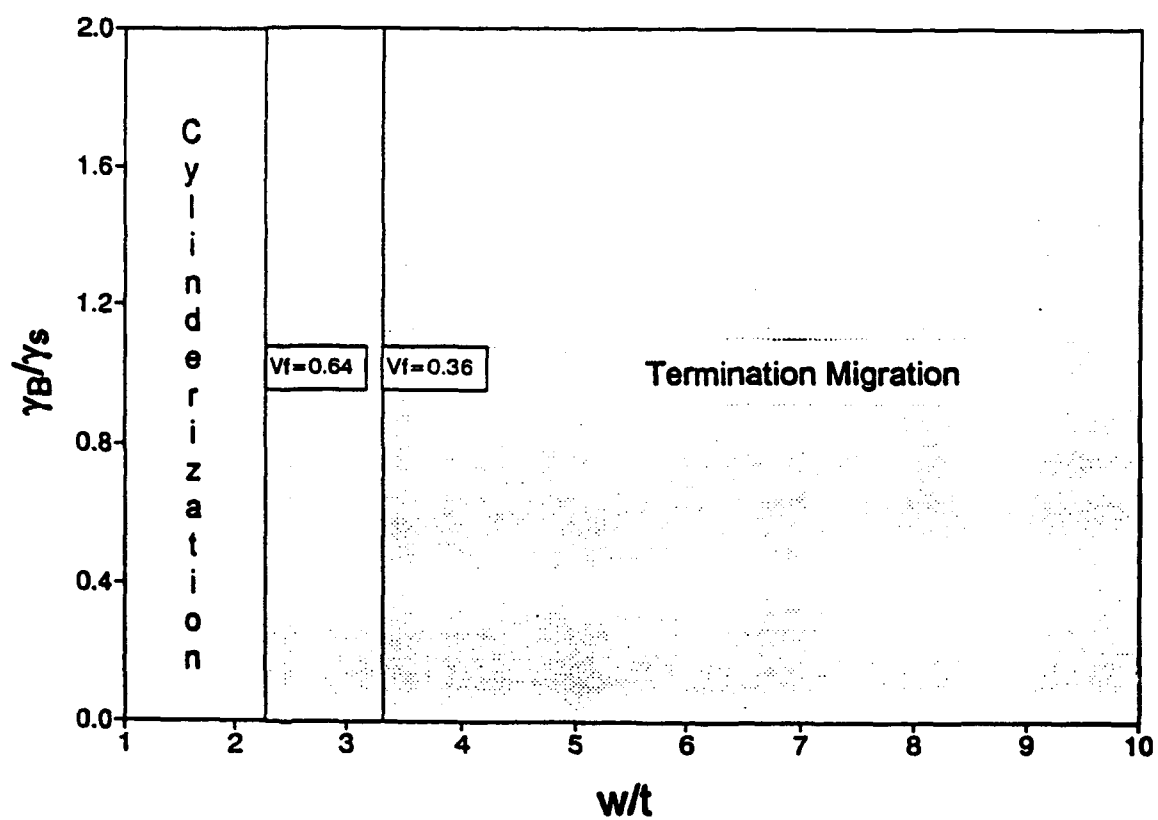
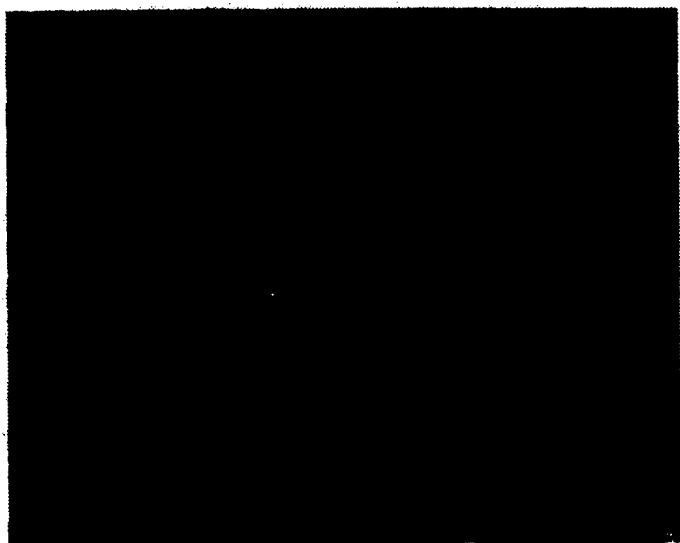


Figure 4. Coarsening diagram for volume diffusion controlled coarsening of lamellar microstructures [8].



(a)



(b)

Figure 5. (a) SEM micrograph of the lamellar specimen annealed at 1323 K for 667 h depicting microstructural characteristics associated with termination migration coarsening. (b) SEM micrograph of the lamellar specimen annealed at 1323 K for 1960 h depicting microstructural characteristics associated with discontinuous coarsening. The dark phase is the TiAl Phase.

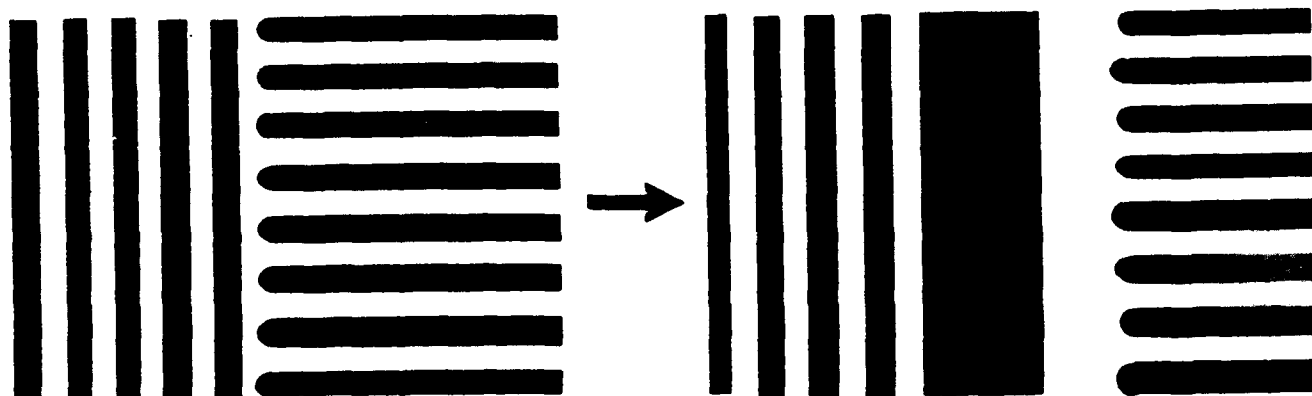


Figure 6. Schematic of interpacket termination migration coarsening during elevated temperature annealing of lamellar microstructure.

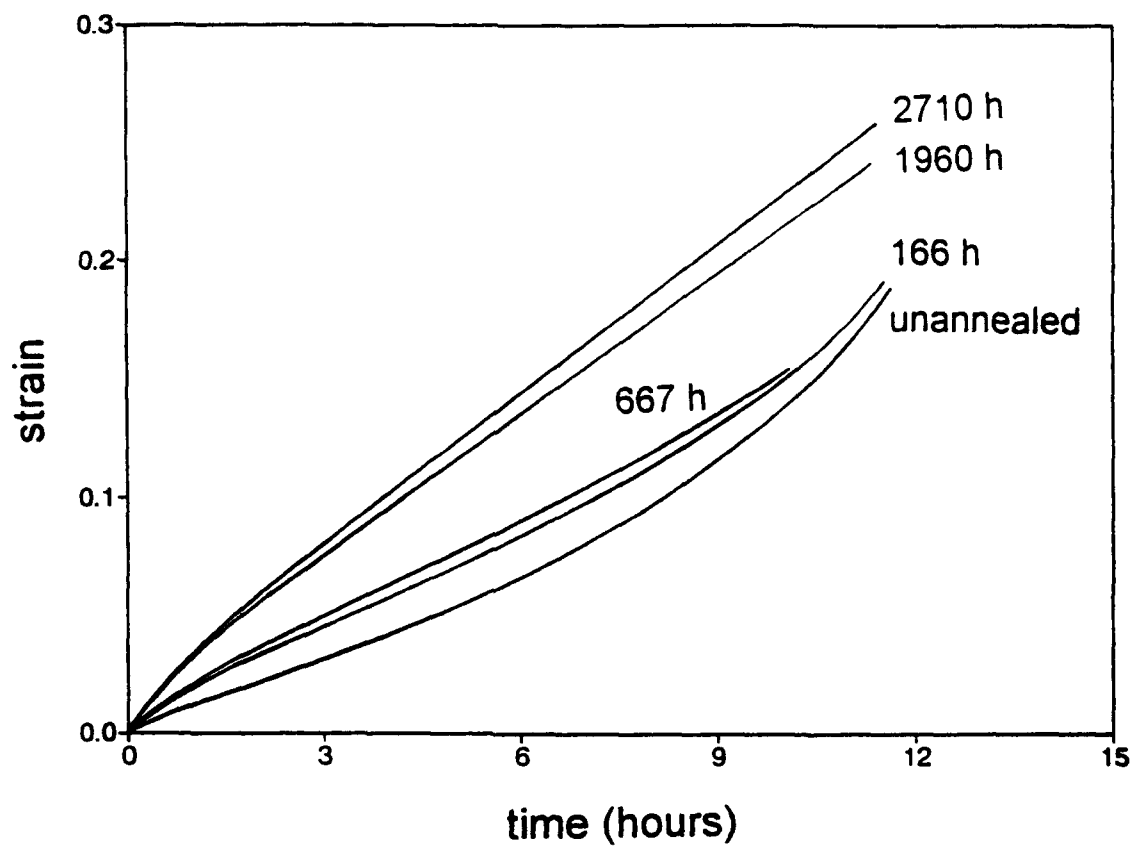


Figure 7. Compression creep curves at 1080 K and 450 MPa for unannealed and previously annealed (1323 K) specimens of the lamellar alloy.

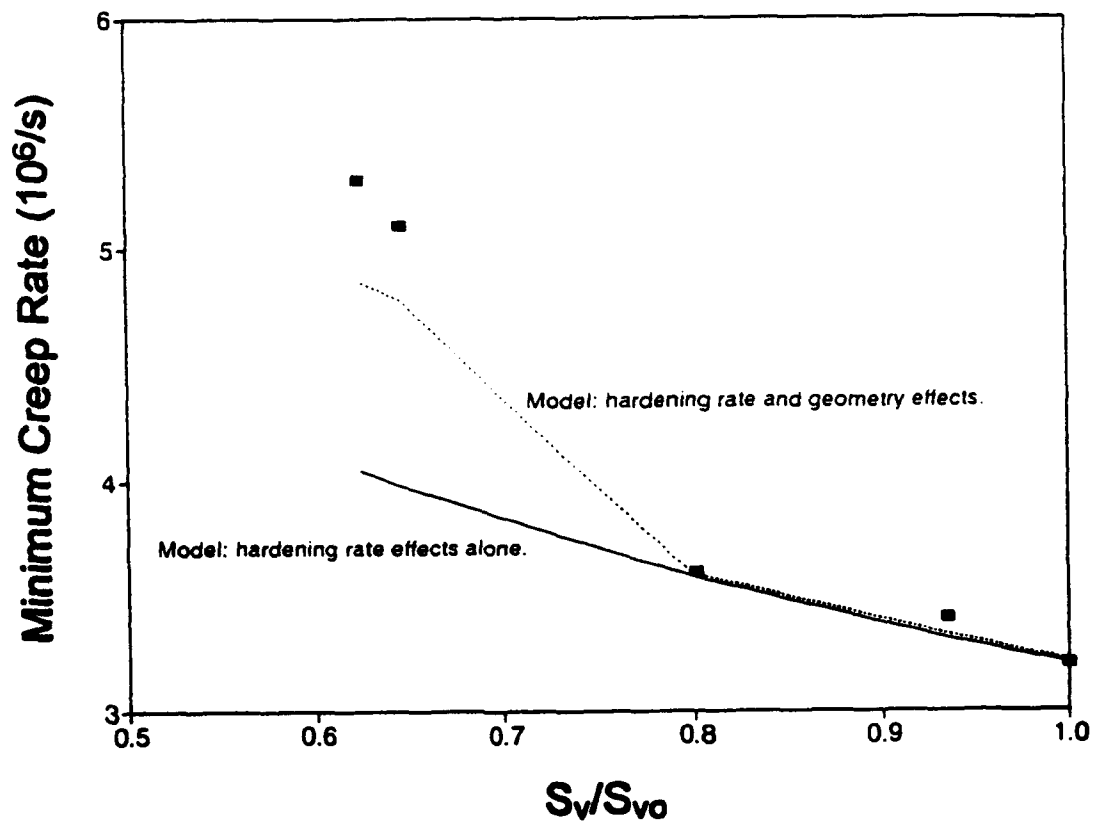


Figure 8. The effect of the change in interfacial surface area-to-volume ratio (S_v) during coarsening on the minimum creep rate of the lamellar alloy. The filled squares represent experimental results. The solid line represents model results that account for the change of hardening rate. The dashed line represents model results that account for both the change of hardening rate and the effect of morphology on composite strengthening.

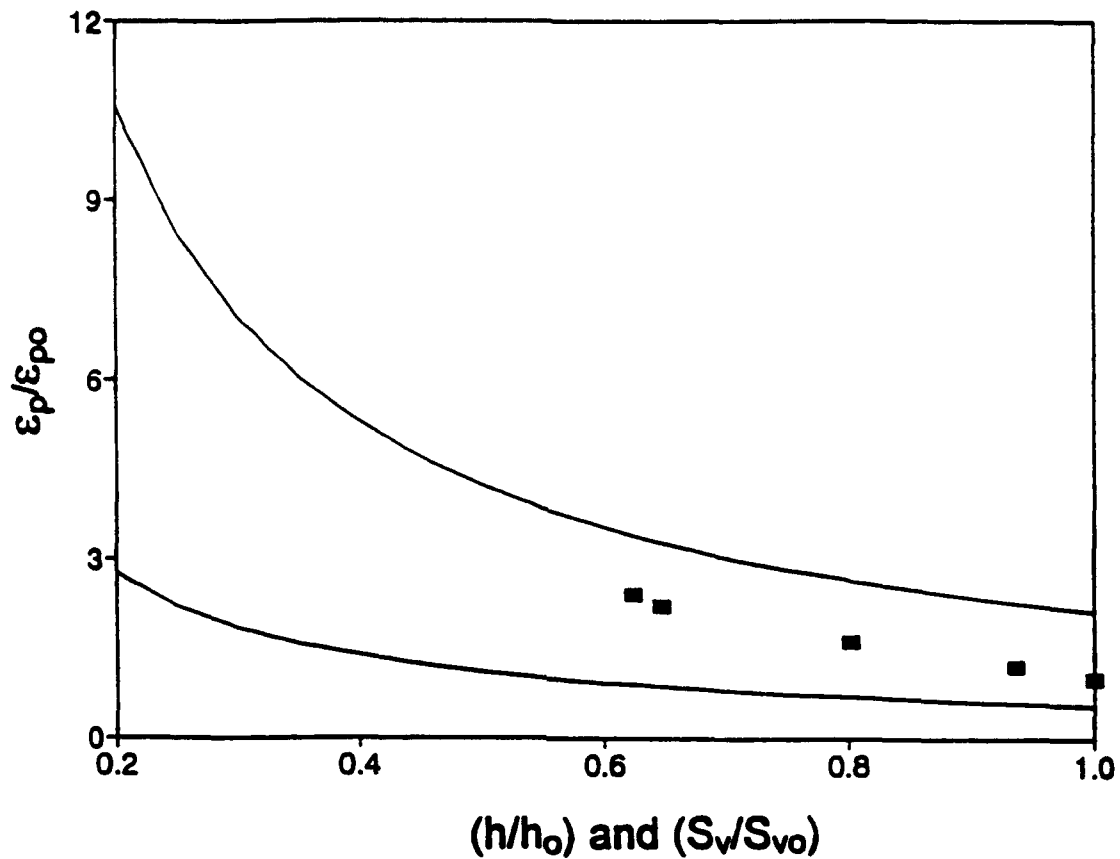


Figure 9. The filled squares represent the experimentally measured dependence of primary creep strain on the change in interfacial surface area-to-volume ratio (S_v/S_{vo}) during coarsening of the lamellar microstructure. The continuous curves represent model predictions of the dependence of primary creep strain on the change in work hardening rate (h/h_o) during coarsening of the lamellar microstructure.



(a)



(b)

Figure 10. SEM micrographs of specimens of the lamellar alloy: (a) Unannealed and crept in compression at 1080 K and 450 MPa to a true strain of 0.46. (b) Annealed at 1323 K for 2710 h and crept in compression at 1080 K and 450 MPa to a true strain of 0.43. The dark phase is the TiAl Phase.

Chapter VI

PUBLICATIONS AND PRESENTATIONS

Publications

1. M.F. Bartholomeusz and J.A. Wert, "Modeling Creep Deformation of a Two-Phase TiAl/Ti₃Al Alloy with a Lamellar Microstructure", *Metallurgical Transactions A*, in press.
2. M.F. Bartholomeusz and J.A. Wert, "The Effect of Thermal Exposure on Microstructural Stability and Creep Resistance of a Two-Phase TiAl/Ti₃Al Lamellar Alloy", *Metallurgical and Materials Transactions A*, in press.
3. M.F. Bartholomeusz and J.A. Wert, "Measurement of the Compressive Creep Strain Rates of the Individual Phases Within a Lamellar Microstructure", submitted to *Materials Characterization*, 1993.
4. M.F. Bartholomeusz and J.A. Wert, "Modeling the Minimum Creep Rate of Discontinuous Lamellar-Reinforced Composites", submitted to *Metallurgical Transactions A*, 1994.
5. M.F. Bartholomeusz, M.A. Cantrell, and J.A. Wert, "The Enhanced Work Hardening Rates of the TiAl and Ti₃Al Phases in Lamellar Microstructure", in preparation.

Presentations

1. M.F. Bartholomeusz and J.A. Wert, "Modeling the Minimum Creep Rate of an In-Situ TiAl/Ti₃Al Composite", TMS Annual Meeting, San Francisco, February 28 - March 3, 1994.

DISTRIBUTION LIST

1 - 10 Air Force Office of Scientific Research
 110 Duncan Avenue, Suite B115
 Bolling Air Force Base
 Washington, DC 20332-0001

 Attention: Dr. Charles Ward, NC
 Directorate of Chemistry and Materials Science

11 - 12 J. A. Wert

13 W. A. Jesser

14 - 15 H. Earnhardt, Clark Hall

* SEAS Postaward Administration

16 SEAS Preaward Administration Files

*Cover letter

JO#5751:ph

**END
FILMED**

DATE: 9-94

DTIC